



### 저작자표시-비영리-변경금지 2.0 대한민국

이용자는 아래의 조건을 따르는 경우에 한하여 자유롭게

- 이 저작물을 복제, 배포, 전송, 전시, 공연 및 방송할 수 있습니다.

다음과 같은 조건을 따라야 합니다:



저작자표시. 귀하는 원 저작자를 표시하여야 합니다.



비영리. 귀하는 이 저작물을 영리 목적으로 이용할 수 없습니다.



변경금지. 귀하는 이 저작물을 개작, 변형 또는 가공할 수 없습니다.

- 귀하는, 이 저작물의 재이용이나 배포의 경우, 이 저작물에 적용된 이용허락조건을 명확하게 나타내어야 합니다.
- 저작권자로부터 별도의 허가를 받으면 이러한 조건들은 적용되지 않습니다.

저작권법에 따른 이용자의 권리와 책임은 위의 내용에 의하여 영향을 받지 않습니다.

이것은 [이용허락규약\(Legal Code\)](#)을 이해하기 쉽게 요약한 것입니다.

[Disclaimer](#)



공학박사 학위논문

**Evaluation of Deformation & Fracture Properties  
of Metallic Materials  
Using Instrumented Flat Punch Indentation**

플랫펀치 압입시험을 이용한  
금속소재의 변형 및 파괴특성 평가

2016년 2월

서울대학교 대학원

재료공학부

김 준 영

**Evaluation of Deformation & Fracture Properties  
of Metallic Materials  
Using Instrumented Flat Punch Indentation**

플랫펀치 압입시험을 이용한  
금속소재의 변형 및 파괴특성 평가

지도교수 권동일

이 논문을 공학박사 학위논문으로 제출함  
2015년 12월

서울대학교 대학원  
재료공학부  
김준영

김준영의 박사학위논문을 인준함  
2015년 12월

위 원장

호수화



부위원장

권동일



위원

박은수



위원

장재일



위원

이봉상



## **ABSTRACT**

Kim, Junyeong

Dept. Materials Science and Engineering

The Graduate School

Seoul National University

Structural integrity is the ability of a structure or a component to withstand a designed service load, resisting structural failure due to fracture, deformation, or fatigue. To construct an item with structural integrity, an engineer must first consider the mechanical properties of a material, such as strength, hardness, or fracture toughness. In many cases, structural failures arise from a change in mechanical properties of the material due to degradation or embrittlement. In such cases, structural integrity assessment requires measurement of in-situ mechanical properties of in-service structural components.

Fracture toughness, defined as the resistance to crack propagation, is one of the most important mechanical properties in fracture mechanical analysis of structural integrity. But standard fracture toughness testing is, like conventional mechanical testing, destructive and requires many specimens with specified geometry, so that measuring in-situ fracture toughness on in-

service structural components is almost impossible. For this reason, nondestructive ways to measure in-situ mechanical properties as well as fracture toughness are highly desirable in order to improve the reliability of structural integrity assessment.

Instrumented indentation testing, developed for nondestructive testing of in-field structures can be considered a solution to this problem. Many researchers have worked to estimate fracture toughness of metallic materials using instrumented indentation testing, trying to develop theoretical or experimental models. But these studies have some drawbacks arising from the many assumptions and empirical correlations made as an inevitable consequence of extrapolating from non-cracking to cracking resistance, that is, fracture toughness.

In this study, new fracture toughness models are developed by theoretical and practical approaches based on fracture mechanics and contact mechanics to estimate the fracture toughness of metallic materials. First, in order to match the stress state beneath an indenter with that ahead of a crack tip, a flat punch indenter is selected instead of the spherical indenter generally used in indentation techniques. Using the flat punch indenter lets us derive a crack-like stress concentration at the edge of the indenter tip. Second, from this, the modeling is conceived as deriving virtual fracture toughness from flat punch indentation, not as in conventional methods correlating indentation

deformation energy with fracture energy. Finally, the specimen size requirement in the fracture toughness testing standard, which has not been considered in previous indentation fracture toughness models but is very important for the validity of fracture toughness value, is made to correspond with the indenter size adjustment in indentation testing.

Two distinct indentation fracture toughness models, a ductile fracture model and a brittle fracture model, have been established. In the ductile fracture model, the crack initiation point is determined by limit load and the indenter size is adjusted to a geometrical relationship between the acceptable crack extension and corresponding indentation depth. In the brittle fracture model, the crack initiation point is determined by the onset of nonlinear behavior in the indentation curve and the indenter size is adjusted to the standard thickness of a fracture toughness specimen.

To verify these models, experimental results are compared with standard J test results and the results are considered to match well if they are within 20% error range. In addition to fracture toughness, tensile properties are also evaluated using flat punch indentation, and the yield strength and strain-hardening exponent can be evaluated by a simpler approach than the strength algorithm for spherical indentation. Further studies are recommended for improvement of indentation fracture toughness models and application to evaluation of the ductile-brittle transition temperature and in-field testing.

**Keywords:** Instrumented Indentation Testing, Fracture Toughness, Flat Punch, Tensile Properties, Ductile Fracture, Brittle Fracture, Structural Integrity

**Student Number:** 2008-20634

# TABLE OF CONTENTS

<b>Abstract</b> .....	i
<b>Table of Contents</b> .....	v
<b>List of Tables</b> .....	vii
<b>List of Figures</b> .....	viii
<b>Chapter 1. Introduction</b> .....	1
1.1. Objective and Scope of the Thesis .....	2
1.2. Outline of the Thesis .....	6
<b>Chapter 2. Research Background</b> .....	7
2.1. Fracture Mechanics .....	8
2.1.1. Overview .....	9
2.1.2. Stress analysis of cracks .....	13
2.1.3. Fracture toughness parameters .....	22
2.1.4. Measurement of fracture toughness .....	32
2.2. Instrumented Indentation Technique .....	43
2.2.1. Introduction .....	43
2.2.2. Applications .....	46
2.2.3. Indentation fracture toughness .....	62
2.3. Flat Punch Indentation .....	74
2.3.1. Contact mechanics .....	74
2.3.2. Equivalence with fracture mechanics .....	83

<b>Chapter 3. Theoretical Modeling</b>	99
3.1. Introduction	100
3.1.1. Origin of modeling	100
3.1.2. Key issues	107
3.2. Ductile Fracture Model	113
3.2.1. Crack initiation determination	113
3.2.2. Indenter size adjustment	117
3.3. Brittle Fracture Model	122
3.3.1. Crack initiation determination	122
3.3.2. Indenter size adjustment	125
<b>Chapter 4. Experimental Verification</b>	128
4.1. Materials and Methods	129
4.2. Results and Discussion	143
4.2.1. Tensile properties	143
4.2.2. Fracture toughness	149
<b>Chapter 5. Conclusions</b>	153
<b>References</b>	156
<b>Abstract in Korean (초록)</b>	165
<b>List of Publications</b>	169
<b>Acknowledgments (감사의 글)</b>	173

## **LIST OF TABLES**

**Table 2.1**

Stress fields ahead of crack tip for Mode

**Table 2.2**

Fracture toughness-Charpy energy correlations

**Table 4.1**

Mechanical properties of tested materials

## LIST OF FIGURES

### **Figure 2.1**

Type of structural failure [33]

### **Figure 2.2**

The three modes of loading that can be applied to a crack

### **Figure 2.3**

Coordinate system and stress components ahead of crack tip

### **Figure 2.4**

Effect of thickness on  $K_C$  behavior [40]

### **Figure 2.5**

Constraint to plastic flow caused by notched geometries [40]

### **Figure 2.6**

Crack tip opening displacement (CTOD). An initially sharp crack blunts with plastic deformation, resulting in a finite displacement,  $\delta$ , at the crack tip

### **Figure 2.7**

Alternative definitions of CTOD: (a) displacement at the original crack tip and (b) displacement at the intersection of a 90° vertex with the crack flanks

### **Figure 2.8**

The hinge model for estimating CTOD from three-point bend specimens

### **Figure 2.9**

Arbitrary contour around the tip of a crack

### **Figure 2.10**

Schematic of typical stress-stain curves: (a) brittle material and (b) ductile material

**Figure 2.11**

Non-adhesive Hertzian contacts: when a sphere is pressed against an elastic material, the contact area increases

**Figure 2.12**

The stress distribution along z-axis under the contact surface

**Figure 2.13**

Expanding cavity model schematic

**Figure 2.14**

Schematic diagram of typical load-depth curve obtained during instrumented indentations: (a) sharp indentation and (b) spherical indentation

**Figure 2.15**

Cross section of contact morphology in the loaded state and residual indent after unloading by a sharp indenter

**Figure 2.16**

Variation of indentation loading curves with changes in the stress state

**Figure 2.17**

Theoretical surface morphologies around the contact for (a) stress-free, (b) tensile stress, and (c) compressive stress states

**Figure 2.18**

Crack system for Vickers indenter: (a) radial cracks, (b) lateral cracks, (c) median cracks, and (d) half-penny cracks

**Figure 2.19**

Schematic of radial cracking by Vickers indentation

**Figure 2.20**

Decreasing elastic modulus with indentation depth (API steels)

**Figure 2.21**

Schematic of flat punch indentation

**Figure 2.22**

Typical flat punch indentation curve

**Figure 2.23**

A schematic representation of the contact between a two-dimensional rectangular punch and a substrate

**Figure 2.24**

Crack analogue of Figure 2.23 showing the double-edge cracked plate specimen which is subjected to mode I and mode II stress intensity factors,  $K_I$  and  $K_{II}$ .

**Figure 2.25**

A schematic representation of the contact between the end of a right-circular cylindrical punch and a substrate

**Figure 2.26**

Crack analogue of Figure 2.25 showing the circumferentially cracked cylindrical rod specimen, and the associated nomenclature

**Figure 3.1**

Similar stress state ahead of a crack tip and beneath an indenter

**Figure 3.2**

Dissimilar symmetry of stress state ahead of a crack tip and beneath an indenter

**Figure 3.3**

Elastic stress field ahead of a crack tip

**Figure 3.4**

Elastic stress fields beneath spherical indenter and flat punch indenter

**Figure 3.5**

Indentation load-depth curves using flat punch indenters of various indenter radii

**Figure 3.6**

Normalization of indentation load-depth curves using flat punch indenters of various indenter radii

**Figure 3.7**

Indentation load-depth curves converted from normalized curve

**Figure 3.8**

Load displacement curves of circumferentially cracked round bar specimen with ductile fracture [129]

**Figure 3.9**

Schematic description of limit load concept

**Figure 3.10**

General  $J_{IC}$  determination method in J-R curve [131]

**Figure 3.11**

$J_{0.2}$  determination method in J-R curve [131]

**Figure 3.12**

Geometrical similarity between flat punch indenter and circumferentially cracked round bar specimen

**Figure 3.13**

Load displacement curves of circumferentially cracked round bar specimen with brittle fracture [129]

**Figure 3.14**

95% secant line method for  $K_{IC}$  determination [46]

**Figure 3.15**

Typical  $K_{JC}$  data adjusted to 1T (inch) thickness with temperature

**Figure 3.16**

Geometrical relationship between crack front length and specimen geometry

**Figure 4.1**

Tensile specimen configuration according to specification ASTM E8:09

**Figure 4.2**

AIS 2100 system for indentation

**Figure 4.3**

Load and displacement curve measured from the basic method

**Figure 4.4**

An example of the unloading compliance method

**Figure 4.5**

Geometry of the SENB specimen used in fracture test according to specification ASTM E1820:09

**Figure 4.6**

ASTM notation for fracture specimens from (a) rolled plate and forgings and (b) disk and hollow cylinders

**Figure 4.7**

Equipment (Instron 8502 in KOGAS) and specimen for  $J$ -integral tests

**Figure 4.8**

Optical crack size measurement for SCM 21 and API X100: (a) original crack length and (b) final physical crack length

**Figure 4.9**

J-R curve results

**Figure 4.10**

Examples of data analysis for evaluating tensile properties using flat punch indentation

**Figure 4.11**

Comparison between indentation tensile properties results and uniaxial tensile test results: (a) yield strength (b) strain-hardening exponent

**Figure 4.12**

Comparison of yield strength between flat punch indentation results and spherical indentation results

**Figure 4.13**

Comparison of strain hardening exponent between flat punch indentation results and spherical indentation results

**Figure 4.14**

Comparison of fracture toughness results between flat punch indentation tests and J tests: (a) ductile fracture model (b) brittle fracture model

**Figure 4.15**

Comparison between normalized flat punch indentation curve and stress strain curve from uniaxial tensile test of SS400

# **Chapter 1**

---

---

## **INTRODUCTION**

### **Contents**

1.1. Objective and Scope of the Thesis .....	2
1.2. Outline of the Thesis .....	6

## **1.1. Objective and Scope of the Thesis**

Structural integrity is the ability of a structure or component to withstand a designed service load, resisting structural failure due to fracture, deformation, or fatigue. It is a concept often used in engineering to produce items that will function adequately for their designed purposes and for a desired service life. To construct an item with structural integrity, an engineer must first consider the mechanical properties of a material, such as strength, hardness, or fracture toughness, and then determine a suitable size, thickness, or shape that will withstand the desired load for a long life. In many cases, structural failures arise from the change in mechanical properties of the material due to degradation or embrittlement. In such cases, structural integrity assessment requires measurement of in-situ mechanical properties of in-service structural components.

Fracture toughness, which is defined as the resistance to crack propagation, is one of the most important mechanical properties for fracture mechanical analysis of structural integrity. Several fracture toughness parameters are used in the given mechanical situations or testing methods, including the critical stress intensity factor,  $K_{IC}$ , the critical value of the J-integral,  $J_{IC}$ , and the critical crack-tip opening displacement, CTOD or  $\delta_{IC}$  [52]. But these fracture toughness parameters are largely influenced by testing

variables such as specimen geometry, crack length, constraints, temperature, and strain rate, so that testing and determining fracture toughness parameters are complex and difficult. Moreover, since standard fracture toughness testing is destructive and requires many specimens of specified geometries, measuring in-situ fracture toughness in in-service structural components is almost impossible. For this reason, a nondestructive way to measure in-situ mechanical properties as well as fracture toughness is necessary to improve the reliability of structural integrity assessment.

Instrumented indentation testing (IIT), which has been developed for nondestructive testing of in-field structures, can be considered a solution to this problem. This technique can be used to measure various mechanical properties such as hardness, elastic modulus [1-3], tensile properties [4-17], residual stress [18-22], and fracture toughness [23-32] by analyzing the indentation load-depth curve. Since IIT makes just a small indent on the surface of the material, it can be applied in in-situ and in-field measurement as a nondestructive mechanical test and for mechanical mapping by local area testing on a multi-scale level.

A well-known technique to evaluate fracture toughness using instrumented indentation testing is the so-called ‘indentation cracking method’, which uses the relationship among an indentation-induced crack length, an indentation load and indentation parameters [23-27]. This method can be applied to very

brittle materials like ceramics that crack during indentation. However, in ductile materials like structural metals, cracking does not occur during indentation, so that the indentation cracking method is not appropriate for nondestructive structural integrity assessment. Consequently, many researchers have tried to develop theoretical or experimental models to estimate the fracture toughness of metallic materials using instrumented indentation testing [28-32]. But these studies have some drawbacks arising from the many assumptions and empirical correlations necessary to move from non-cracking to cracking resistance, that is, fracture toughness.

In this study, new fracture toughness models are developed by more theoretical and practical approaches based on fracture mechanics and contact mechanics to estimate the fracture toughness of metallic materials. First, in order to match the stress state beneath an indenter with that ahead of a crack tip, a flat punch indenter is selected, instead of the spherical indenter generally used in indentation techniques. Using the flat punch indenter, makes it possible to derive a crack-like stress concentration at the edge of the indenter tip. Second, from this, the model is designed as deriving virtual fracture toughness from a flat punch indentation, unlike the conventional methods of correlating indentation deformation energy with fracture energy. Finally, the specimen size requirement in the fracture toughness testing standard, which is not considered in previous indentation fracture toughness

models but is very important for the validity of fracture toughness value, is made to correspond with the indenter size adjustment in indentation testing.

## **1.2 Outline of the Thesis**

The thesis has five chapters. After a brief introduction in Chapter 1, Chapter 2 gives a historical overview of fracture mechanics, stress analysis of cracks, fracture toughness parameters, and methods to measure fracture toughness. Theories of and methods for the instrumented indentation technique (IIT), a nondestructive technique to evaluate mechanical properties such as hardness, elastic modulus, tensile properties, residual stress, and fracture toughness, are discussed in detail, in particular previous work on fracture toughness. Chapter 2 also gives a detailed description of indentation stress fields for a cylindrical flat punch indenter and equivalence with fracture mechanics, from which is derived the basic principle of the new indentation fracture toughness models presented here. The theoretical grounding of new models to estimate fracture toughness is presented in Chapter 3. In Chapter 4, experimental work to verify the new models is described and the results are discussed. Finally, conclusions and recommendations for further study are given in Chapter 5.

# **Chapter 2**

---

---

## **RESEARCH BACKGROUND**

### **Contents**

2.1. Fracture Mechanics .....	8
2.1.1. Overview	
2.1.2. Stress analysis of cracks	
2.1.3. Fracture toughness parameters	
2.1.4. Measurement of fracture toughness	
2.2. Instrumented Indentation Technique .....	43
2.2.1. Introduction	
2.2.2. Applications	
2.2.3. Indentation fracture toughness	
2.3. Flat Punch Indentation .....	74
2.3.1. Contact mechanics	
2.3.2. Equivalence with fracture mechanics	

## 2.1. Fracture Mechanics

Failures of strength in load-bearing structures can be either yielding-dominant failures or fracture-dominant failures. Defects are important in both failure types, but those of primary importance to fracture differ considerably from those influencing yielding and the resistance to plastic flow. These differences are illustrated schematically in Figure 2.1 [33].

For yielding-dominant failures, the significant defects are those that tend to warp and interrupt the crystal lattice planes, thus interfering with dislocation glide and providing a resistance to plastic deformation that is essential to the strength of high-strength metals. Examples of such defects are interstitial and out-of-size substitutional atoms, grain boundaries, coherent precipitates and dislocation networks. Larger defects like inclusions, porosity, surface scratches and small cracks may influence the effective net section bearing the load, but otherwise have little effect on resistance to yielding.

For fracture-dominant failures, the size scale of the defects of major significance is essentially macroscopic, since general plasticity is not involved but only the local stress-strain fields associated with the defects. The minute lattice-related defects that control resistance to plastic flow are not of direct concern. They are important insofar as the resistance to plastic flow is related to the material's susceptibility to fracture.

### 2.1.1. Overview

The commonly accepted first successful analysis of a fracture-dominant problem was that of Griffith in 1920 [34], who considered the propagation of brittle cracks in glass. Griffith formulated the well-known concept that an existing crack will propagate if the total energy of the system is lowered thereby, and he assumed a simple energy balance involving a decrease in elastic strain energy within the stressed body as the crack extends, counteracted by the energy needed to create the new crack surface. From Griffith theory [34], fracture stress is obtained as in Eq. (2-1),

$$\sigma = \left( \frac{2E\gamma_s}{\pi a} \right)^{\frac{1}{2}} \quad (2-1)$$

where  $a$  is crack length and  $2\gamma_s$  is surface energy. Eq. (2-1) indicates that crack extension in ideally brittle materials is governed by the product of the remotely applied stress and the square root of the crack length and by material properties. Because  $E$  and  $\gamma_s$  are material properties, the right-hand side of Eq. (2-1), except for the crack length  $a$ , is equal to a constant value characteristic of a given ideally brittle material. Consequently, Eq. (2-1) indicates that crack extension occurs when the product  $\sigma\sqrt{a}$  attains a certain

critical value. The Griffith concept has the limitation that it applies only to elastic, brittle materials, in which no plastic deformation took place.

Irwin [35] modified the Griffith expression to take ductile material into account. Irwin indicated that the Griffith energy balance must be between the stored strain energy and the surface energy plus the work done in plastic deformation. He recognized that for relatively ductile materials the energy required to form new crack surfaces is generally insignificant compared to the work done in plastic deformation. The revised expression is given by

$$\sigma_f = \left( \frac{2E(\gamma_s + \gamma_p)}{\pi a} \right)^{\frac{1}{2}} \quad (2-2)$$

where  $\gamma_p$  is the plastic work per unit area of surface created, and is typically much larger than  $\gamma_s$ . He also defined a quantity called *energy release rate* or *crack driving force*,  $G$ , as the total energy that is released during cracking per unit increase in crack size. Moreover, Irwin contributed another major advance by showing that the energy approach ( $G$ ) is equivalent to a stress intensity approach ( $K$ ), according to which fracture occurs when a critical stress distribution ahead of the crack tip is reached, when a critical strain energy release rate ( $G_c$ ) or critical stress intensity ( $K_c$ ) is accomplished.

In the 1960s, fracture mechanics theories were developed to handle various

type of nonlinear material behavior, i.e. plasticity, notably Wells and Post's [36] work on crack tip displacement (CTD). In 1968, Rice and Rosengren [37] introduced an elastic-plastic fracture parameter with a more theoretical basis: the J integral, which expresses the energy release rate can be expressed as a path-independent line integral. Although both CTD and J are now well established concepts, elastic-plastic fracture mechanics (EPFM) is still very much an evolving discipline because of the complexity of elastic-plastic analysis.

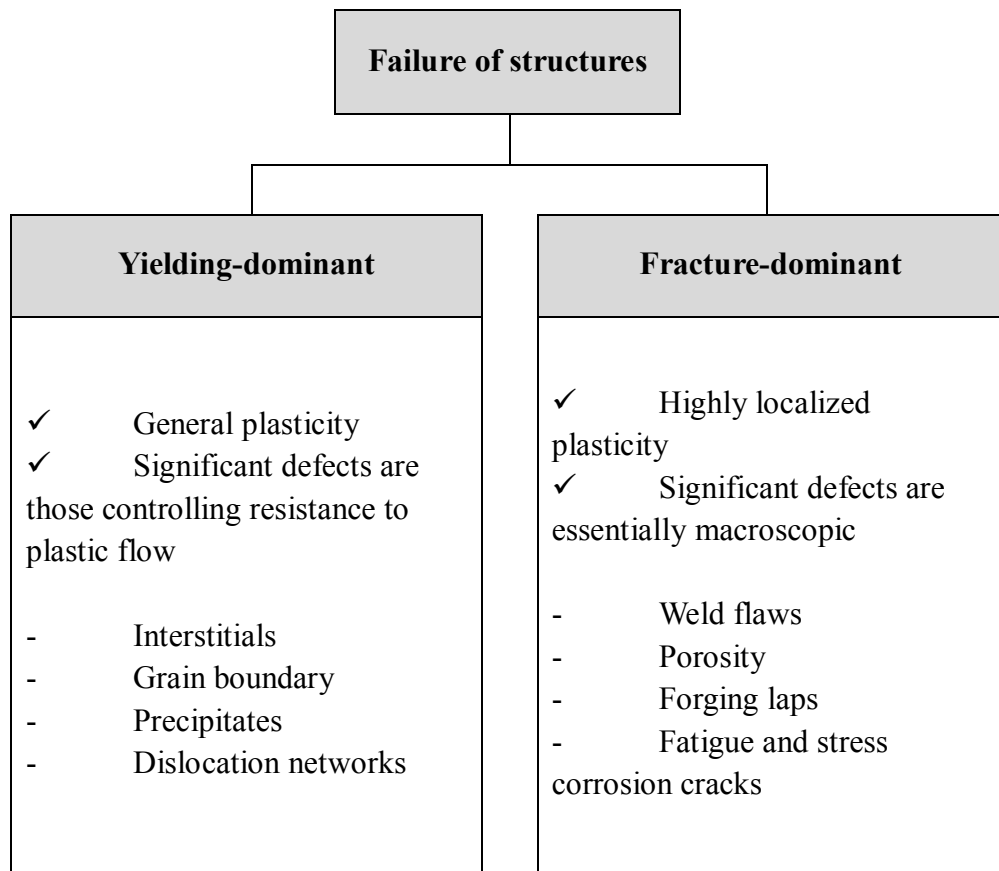


**Figure 2.1** Type of structural failure [33]

## 2.1.2. Stress analysis of cracks

### 2.1.2.1. Crack tip stress analysis

There are three types of loading that a crack can experience, as Figure 2.2 illustrates. Mode I loading, in which the principal load is applied normal to the crack plane, tends to open the crack. The two fracture surfaces are displaced perpendicular to each other in opposite directions. Mode II corresponds to in-plane shear loading and tends to slide one crack face with respect to the other. Mode III involves out-of-plane shear. A cracked body can be loaded in any one of these modes or in a combination of two or three modes.

Westergaad [38] and Irwin [39] developed analytically the crack tip stress field for a linear elastic isotropic material subjected to the three modes of deformation, as listed in Table 2.1. The stress components and the coordinates  $r$  and  $\theta$  are shown in Figure 2.3;  $u_x$ ,  $u_y$ , and  $u_z$  are the displacements in the  $x$ ,  $y$ , and  $z$  directions, respectively;  $v$  is Poisson's ratio, and  $G$  is the shear modulus of elasticity.

### 2.1.2.2. Effect of constraint on fracture toughness

Of the three primary factors that affect the fracture toughness of a given material — temperature, loading rate, and constraint — the effect of constraint is the most difficult to establish quantitatively. The primary definition of constraint deals with the plane-strain-to-plane-stress transition as defined by specimen thickness. Plane strain is the maximum constraint and occurs in very thick test specimens having deep cracks. In contrast, plane stress refers to minimum constraint and occurs in thin test specimens.

Ahead of a sharp crack, the lateral constraint, which increases with increasing specimen thickness, is such that through-thickness stresses are present. Because these through-thickness stresses must be zero at each surface of a specimen, they are less for thin specimens than thick ones. For very thick specimens, the through-thickness stresses at the centerline are large and a triaxial tensile state of stress occurs ahead of the crack. This triaxial state of stress reduces the apparent ductility of the material by decreasing the shear stresses. Because yielding is restricted, the constraint ahead of the crack is increased and thus the fracture toughness is reduced. This decrease in fracture toughness is controlled by the thickness of the specimen, even though the inherent metallurgical properties of the material may be unchanged. Thus, the fracture toughness is smaller for thick specimens than for thinner specimens of the same material. This behavior is shown schematically in Figure 2.4 [40], which indicates that the minimum

fracture toughness of a particular material,  $K_{IC}$ , is reached when the thickness of the specimen is large enough so that the state of stress is plane strain.

To demonstrate the significant constraint effect on the fracture behavior of a given material, consider a point on the crack plane just ahead of the crack tip. According to Table 2.1, the stresses in the x and y direction at a point on the crack plane ( $\theta = 0$ ) for Mode I are equal:

$$\sigma_x = \sigma_y = \frac{K_I}{\sqrt{2\pi r}} \quad (2-3)$$

When  $\theta = 0$  under linear elastic conditions, the shear stress is zero, which means that the crack plane is a principal plane for pure Mode I loading. If the stress state is the plane stress,  $\sigma_z = 0$  by definition. Under plane strain conditions,  $\sigma_z = 2\nu\sigma_y$ . Substituting these stresses into the von Mises yield criterion leads to the following:

$$\sigma_y = \sigma_{ys} \text{ (plane stress)} \quad (2-4a)$$

$$\sigma_y = 2.5\sigma_{ys} \text{ (plane strain)} \quad (2-4b)$$

assuming  $\nu = 0.3$ . Therefore, the triaxial stress state associated with plane strain leads to higher stresses in the plastic zone. For fracture mechanisms

that are governed by normal stress, such as cleavage in metals, the material will behave in a more brittle fashion when subjected to a triaxial stress state. Triaxial stresses also assist ductile fracture processes such as microvoid coalescence.

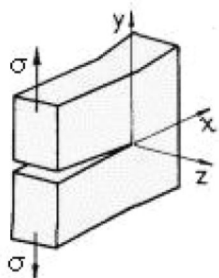
Pellini [41] described the physical significance of constraint and plate thickness on fracture toughness in terms of plastic flow, as shown in Figure 2.5. This figure shows that the introduction of a circular notch in a bar loaded in tension elevates the stress-strain curve. The plastic flow of the smooth tensile bar, which is usually used to develop conventional stress-strain curves, is free flow because lateral contraction is not constrained during initial loading. In the notched bar, however, the reduced section deforms inelastically while the ends of the specimen are still loaded elastically. Since the amount of elastic contraction is small compared to the inelastic contraction of the reduced section, a restriction to plastic flow is developed. This restriction is in the nature of a reaction-stress system such that the  $\sigma_x$  and  $\sigma_y$  stresses restrict or constrain the flow in the  $\sigma_y$  direction. Thus, the uniaxial stress state of the smooth bar is changed to a triaxial tensile stress system in the notched bar compared with the unnotched bar. As the notch becomes far sharper, the severity of the stress state increases.

**Table 2.1** Stress and displacement fields ahead of crack tip for each mode

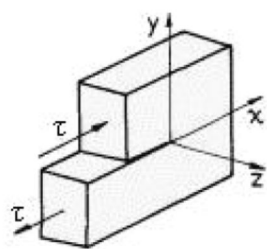
	<b>Mode I</b>	<b>Mode II</b>	<b>Mode III</b>
$\sigma_{xx}$	$\frac{K_I}{\sqrt{2\pi r}} \cos\left(\frac{\theta}{2}\right) \left[ 1 - \sin\left(\frac{\theta}{2}\right) \sin\left(\frac{3\theta}{2}\right) \right]$	$\frac{K_{II}}{\sqrt{2\pi r}} \sin\left(\frac{\theta}{2}\right) \left[ 2 + \cos\left(\frac{\theta}{2}\right) \cos\left(\frac{3\theta}{2}\right) \right]$	-
$\sigma_{yy}$	$\frac{K_I}{\sqrt{2\pi r}} \cos\left(\frac{\theta}{2}\right) \left[ 1 + \sin\left(\frac{\theta}{2}\right) \sin\left(\frac{3\theta}{2}\right) \right]$	$\frac{K_{II}}{\sqrt{2\pi r}} \sin\left(\frac{\theta}{2}\right) \cos\left(\frac{\theta}{2}\right) \cos\left(\frac{3\theta}{2}\right)$	-
$\sigma_{zz}$	$0$ (plane stress) $v(\sigma_{xx} + \sigma_{yy})$ (plane strain)	$0$ (plane stress) $v(\sigma_{xx} + \sigma_{yy})$ (plane strain)	-
$\tau_{xy}$	$\frac{K_I}{\sqrt{2\pi r}} \cos\left(\frac{\theta}{2}\right) \sin\left(\frac{\theta}{2}\right) \cos\left(\frac{3\theta}{2}\right)$	$\frac{K_{II}}{\sqrt{2\pi r}} \cos\left(\frac{\theta}{2}\right) \left[ 1 - \sin\left(\frac{\theta}{2}\right) \sin\left(\frac{3\theta}{2}\right) \right]$	-
$\tau_{yz}$	0	0	$\frac{K_{III}}{\sqrt{2\pi r}} \cos\left(\frac{\theta}{2}\right)$
$\tau_{xz}$	0	0	$-\frac{K_{III}}{\sqrt{2\pi r}} \sin\left(\frac{\theta}{2}\right)$
$u_x$	$\frac{K_I}{2\mu} \sqrt{\frac{r}{2\pi}} \cos\left(\frac{\theta}{2}\right) \left[ \kappa - 1 + 2 \sin^2\left(\frac{\theta}{2}\right) \right]$	$\frac{K_{II}}{2\mu} \sqrt{\frac{r}{2\pi}} \sin\left(\frac{\theta}{2}\right) \left[ \kappa + 1 + 2 \cos^2\left(\frac{\theta}{2}\right) \right]$	-
$u_y$	$\frac{K_I}{2\mu} \sqrt{\frac{r}{2\pi}} \sin\left(\frac{\theta}{2}\right) \left[ \kappa + 1 - 2 \cos^2\left(\frac{\theta}{2}\right) \right]$	$-\frac{K_{II}}{2\mu} \sqrt{\frac{r}{2\pi}} \cos\left(\frac{\theta}{2}\right) \left[ \kappa - 1 - 2 \sin^2\left(\frac{\theta}{2}\right) \right]$	-
$u_z$	-	-	$\frac{2K_{III}}{\mu} \sqrt{\frac{r}{2\pi}} \sin\left(\frac{\theta}{2}\right)$

Note:  $v$  is Poisson's ratio and  $\mu$  is the shear modulus.  $\kappa = 3 - 4v$  (plane strain) and  $\kappa = (3 - v)/(1 + v)$  (plane stress).

**Mode I**



**Mode II**



**Mode III**

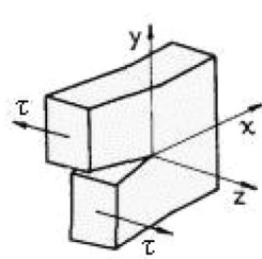


**Figure 2.2** The three modes of loading that can be applied to a crack

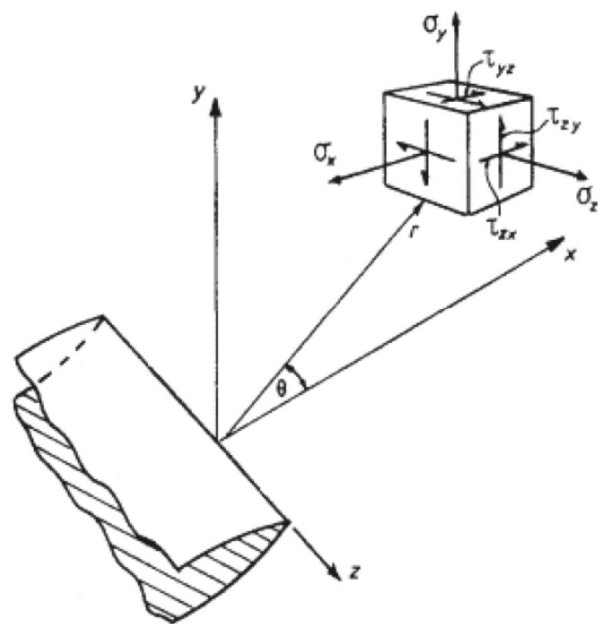


**Figure 2.3** Coordinate system and stress components ahead of crack tip

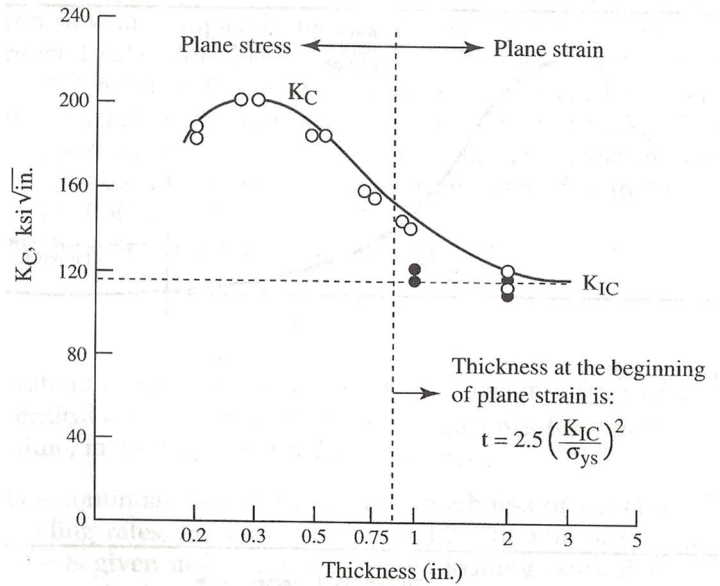


**Figure 2.4** Effect of thickness on  $K_{IC}$  behavior [40]

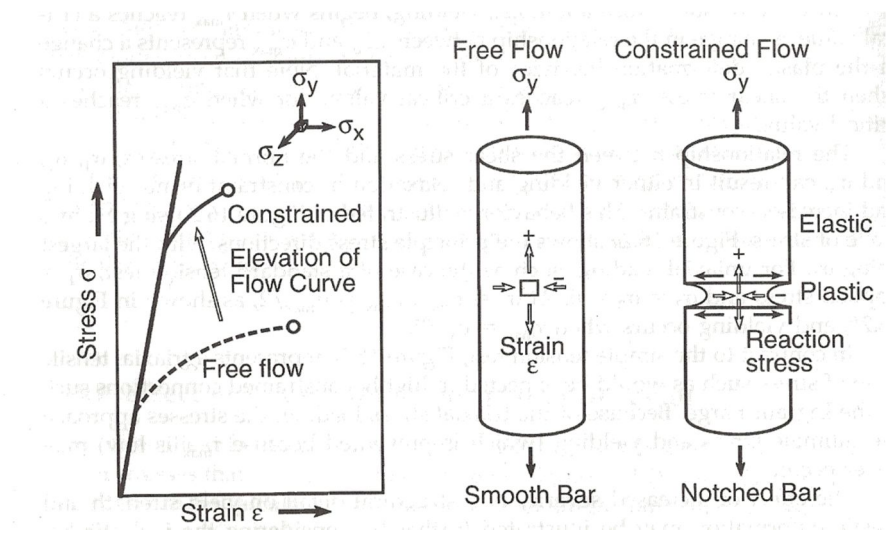


**Figure 2.5** Constraint to plastic flow caused by notched geometries [40]

### **2.1.3. Fracture toughness parameters**

The fracture toughness of a material measures its ability to resist crack initiation and propagation. Several fracture toughness parameters are available, including the critical stress intensity factor, the critical value of the J integral, and the critical crack tip opening displacement.

#### **2.1.3.1. Stress intensity factor**

Irwin [39] showed that the stresses in the vicinity of a crack tip have the form

$$\sigma_{ij} = \frac{K}{\sqrt{2\pi r}} f_{ij}(\theta) + \dots \quad (2-5)$$

where  $r, \theta$  are the cylindrical polar coordinates of a point with respect to the crack tip. K, the stress intensity factor, is a quantity that gives the magnitude of the elastic stress field. Dimensional analysis shows that K must be linearly related to stress and directly related to the square root of a characteristic length. Eq. (2-1) from Griffith's analysis indicates that this characteristic length is the crack length, and it turns out that the general form

of the stress intensity factor is given by:

$$K = \sigma\sqrt{\pi a} \cdot f(a/W) \quad (2-6)$$

where  $f(a/W)$  is a dimensionless parameter that depends on the geometries of the specimen and crack and  $\sigma$  is the applied stress.

It is customary to write the limiting value of  $K$  for maximum constraint, i.e. plane strain, in Mode I fracture as  $K_{IC}$ .  $K_{IC}$  can be considered a material property characterizing the crack resistance, and is therefore called the plane strain fracture toughness. Thus the same value of  $K_{IC}$  should be found by testing specimens of the same material with different geometries and with different critical combinations of crack size and shape and fracture stress.

### 2.1.3.2. Crack tip opening displacement

Wells [42] focuses on the strains in the crack tip region instead of the stresses, unlike the stress intensity approach. He noticed that the crack faces had moved apart prior to fracture; the presence of the plasticity, i.e. plastic deformation, had blunted an initially sharp crack. The degree of crack blunting increased in proportion to the toughness of the material, as illustrated in Figure 2.6. Eventually, Wells proposed using the crack flank

displacement at the tip of a blunting crack, the well-known the crack tip opening displacement (CTOD), as a fracture toughness parameter.

There are a number of alternative definitions of CTOD. The two most common ones, shown in Figure 2.7, are the displacement at the original crack tip and the 90° intercept. These two definitions are equivalent if the crack blunts in a semicircle.

CTOD can be considered a strain-based estimate of fracture toughness. However, it can be separated into elastic and plastic components, as in Eq. (2-7):

$$\delta = \delta_{el} + \delta_p. \quad (2-7)$$

Here the subscripts *el* and *p* denote elastic and plastic components, respectively.

The elastic part of CTOD is derived from the stress intensity factor computed from the load and specimen dimensions, K. In some standards, the plastic component of CTOD is obtained by assuming that the specimen rotates about a plastic hinge, as in Figure 2.8 [43]. The plastic component is derived from the crack mouth opening displacement which measured using a clip gauge. The position of the plastic hinge is given in test standards for each specimen type.

### 2.1.3.3. J-Integral

The fracture parameter J-integral proposed by Rice and Rosengren [37] is a contour integral that can be evaluated along any arbitrary path enclosing the crack tip, as illustrated in Figure 2.9. They considered the potential energy changes involved in crack growth in a nonlinear elastic material. Such nonlinear elastic behavior is a realistic approximation for plastic behavior provided no unloading occurs in any part of the material. From these concepts, the authors derived the J-integral as in Eq. (2-8):

$$J = \int_{\Gamma} \left( w dy - T_i \frac{\partial u_i}{\partial x} ds \right) \quad (2-8)$$

where  $w$  is the strain energy density and  $s$  is distance along an arbitrary path,  $\Gamma$ , around the crack tip.  $T_i$  and  $u_i$  are the component of the traction vector and the displacement vector, respectively.

It is also shown in [37] that  $J$  is equal to the energy release rate for a crack in an elastic-plastic material, analogous to  $G$  for linear elastic material.  $J$  is thus a more general version of the energy release rate and for the special case of a linear elastic material only,  $J$  is identical to  $G$ . The energy release rate is generally defined as the potential energy that is released from a structure

when the crack grows in an elastic material. However, much of the strain energy absorbed by an elastic-plastic material is not recovered when the crack grows or the specimen is unloaded; a growing crack in an elastic-plastic material leaves a plastic wake. Thus the energy release rate concept has a somewhat different interpretation for elastic-plastic materials. Consequently, the energy release rate of  $J$  is useful for elastic-plastic materials when applied in an appropriate manner.

#### **2.1.3.4. Relationship among fracture parameters**

As mentioned above, for linear elastic conditions, the  $J$ -integral is identical to  $G$ , the energy release rate per unit crack extension. Therefore it is possible to infer “equivalent”  $K_{IC}$  values from  $J$  and CTOD by exploiting the relationships among three fracture toughness parameters for the linear elastic case.

Under plane strain linear elastic conditions,

$$J_{IC} = G_{IC} = \frac{(1 - v^2)K^2_{IC}}{E} \quad (2-9)$$

The CTOD parameter,  $\delta$ , is also related to  $J$  as follows:

$$\delta = \frac{G}{m\sigma_{ys}} = \frac{K^2_{IC}}{m\sigma_{ys}E} \quad (2-10)$$

where  $m$  is a dimensionless constant that depends on the stress state and material properties,  $1 \leq m \leq 2$ . By Eqs. (2-9) and (2-10), the fracture mechanics analysis can be expressed in terms of any one of the three parameters based on the relationships below:

- a) For small-scale yielding, an equivalent  $K_{IC}$ , denoted  $K_{JC}$ , can be computed as follows:

$$K_{JC} = \sqrt{\frac{J_{IC} \cdot E}{1 - \nu^2}} \quad (2-11)$$

- b) An approximate relationship between the J-integral and CTOD is given by Eq. (2-12).

$$J_{IC} = m \cdot \sigma_{ys} \cdot \delta_{IC} \quad (2-12)$$

- c) By combining the above equations, the equivalent value computed from CTOD data is given by Eq. (2-13):

$$K_{JC} = \sqrt{\frac{m \cdot \sigma_{ys} \cdot \delta_{IC} \cdot E}{1 - \nu^2}} \quad (2-13)$$

Some studies [44-45] indicate that flow strength,  $\sigma_{flow}$ , should be used in place of yield strength in Eqs. (2-12) and (2-13).

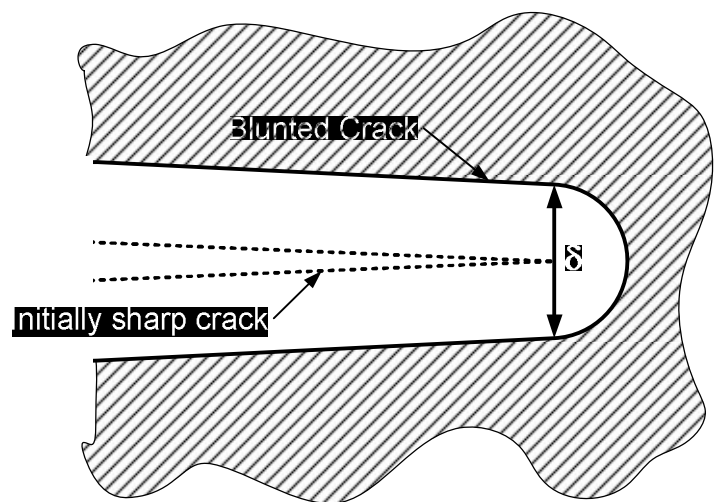


**Figure 2.6** Crack tip opening displacement (CTOD). An initially sharp crack blunts with plastic deformation, resulting in a finite displacement,  $\delta$ , at the crack tip.

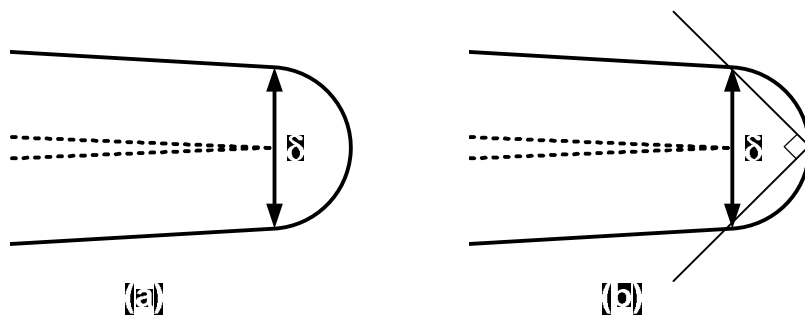


**Figure 2.7** Alternative definitions of CTOD: (a) displacement at the original crack tip and (b) displacement at the intersection of a  $90^\circ$  vertex with the crack flanks.

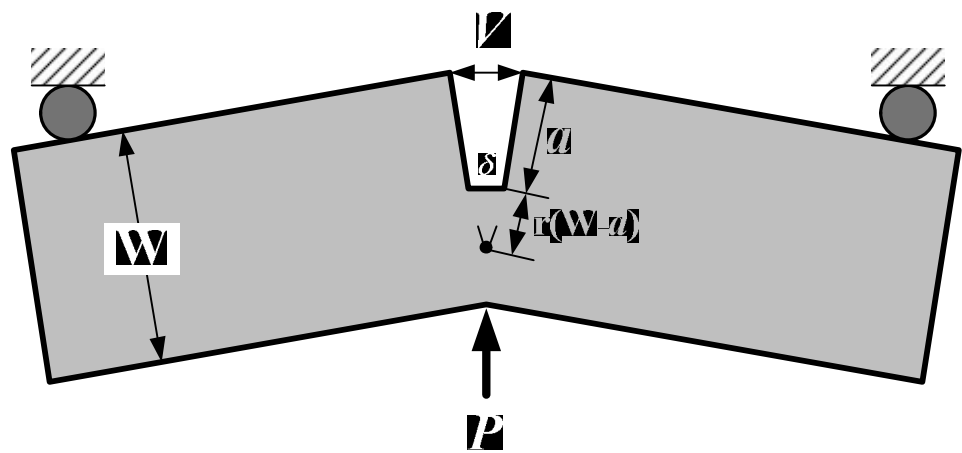


**Figure 2.8** The hinge model for estimating CTOD from three-point bend specimens

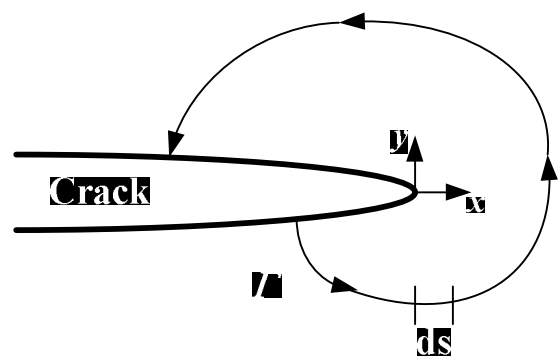


**Figure 2.9** Arbitrary contour around the tip of a crack

## **2.1.4. Measurement of fracture toughness**

### **2.1.4.1. ASTM standard fracture toughness tests**

Several ASTM testing methods have been developed to measure the various critical stress intensity factors for materials that exhibit different types of fracture behavior and the corresponding service conditions.

- 1)  $K_{IC}$  [46]

Plane strain fracture toughness values obtained at slow loading rates. Plane strain refers to conditions of maximum constraint, e.g., generally thick plates and deep cracks. Fracture is sudden, resulting in unstable brittle fracture with little or no deformation.

- 2)  $\delta_c$  [47-49],  $J_c$  [50]

Elastic-plastic plane stress behavior during slow loading accompanied by plastic zone development, but not stable crack growth. Failure is by rapid unstable brittle fracture.

3)  $J_{IC}$  [51]

Critical value of the J-integral that describes the stress-strain field ahead of a crack is a measure of the fracture toughness at the onset of slow stable crack extension. Behavior is nonlinear elastic plastic.

4)  $\delta_u$  [47-49],  $J_u$  [50]

Elastic-plastic behavior during slow loading accompanied by slow stable ductile crack growth. This stable crack growth is either followed by brittle fracture or continued stable ductile crack growth until separation of the test specimen.

5)  $J_C$ ,  $J_{IC}$ ,  $J-R$  [51]

A new test method has been developed to cover all J-integral test results in one standard. Behavior is elastic-plastic with or without stable crack extension.

6)  $K$ ,  $J$ , CTOD ( $\delta$ ) [52]

This standard effectively replaces all previous test methods. A new common fracture test method, the Standard Test Method [51], has been developed for materials when the type of behavior and thus the type of test needed is not known before testing. A bend or compact specimen is tested and the  $P$ - $\delta_{CMOD}$  and  $P$ - $\delta_{LLD}$  records, where CMOD is the crack mouth opening displacement and LLD is the load line displacement, are analyzed as either of three fracture toughness values, depending on the test records.

#### 7) $K_{JC}$ [53]

This test method covers the determination of a reference temperature,  $T_o$ , that characterizes the fracture toughness of ferritic steels that experience onset of cleavage cracking at elastic or elastic-plastic  $K_{IC}$  instabilities or both [53]. This method treats the statistical effects of specimen size on  $K_{JC}$  in the transition range using the weakest-link theory applied to a three-parameter Weibull distribution of fracture values [54]. Accordingly, it has advantages in dealing with the variability of test results.

#### **2.1.4.2. Limitations and alternative approach**

This section gives a brief review of the estimation of fracture toughness

( $K_{IC}$ ) by methods other than the standard fracture toughness tests. The standard tests have significant limitations: 1) complex test procedures, 2) strict requirements for validating  $K_{IC}$ , primarily because of thickness effects, and 3) the effects of pre-existing defects. Consequently,  $K_{IC}$  values obtained in different works show large variations, and many researchers have tried to find alternative approaches that are easier and more convenient.

One such approach is to calculate the area under the stress-strain curve from a tension test [55], a value is simply known as *material toughness*. In general, fracture toughness can be defined as the strain energy absorbed by a material prior to fracture. The area under the stress-strain curve is a measure of fracture toughness in terms of the strain energy density, which is not a common variable in structural engineering analysis but may be used as a controlling parameter in classifying structural materials. Figure 2.10 shows typical stress-strain curves characterizing the behavior of an initially crack-free material. A material of high strain-energy density usually has greater fracture toughness than a material of low strain-energy density. However, when a notched tensile specimen of a ductile material is loaded in tension, the plastic flow is shifted upwards because a triaxial stress state is developed at the root of the notch. This means that a strain-energy density derived from the tensile curve is significantly affected by the presence of a notch in the specimen, and that the fracture toughness in terms of strain-energy density of

crack-free materials does not apply to the fracture behavior of materials with cracks.

Nevertheless, attempts to estimate fracture toughness from tensile properties continue to evolve due to the simplicity and cost-effectiveness of the tension test. Many attempts have been made to estimate the plane-strain fracture toughness  $K_{IC}$  of ductile materials from other properties. Such modeling encounters several problems [33]:

- 1) Stress-strain distributions in the plastic zone ahead of the crack must be known or assumed. In this respect strain hardening is very important.
- 2) The proper fracture criterion must be chosen. Ductile rupture is strain controlled, i.e. the local strain must exceed a critical value. This is sometimes considered the fracture strain at the crack tip.
- 3) The critical strain must be reached or exceeded over a certain distance or volume. A reasonable assumption is that this distance is equal to the particle spacing. However, there is a complication: the critical strain depends strongly on the stress state, which varies significantly near the crack tip.
- 4) Calculation of  $K_{IC}$  is based on the assumption that unstable fracture occurs when the fracture criterion is satisfied. But the actual

determination of  $K_{IC}$  involves 2% crack extension which, if stable, can cause a significant increase in stress intensity.

In view of these problems, it is clear that the evaluation of fracture toughness is often very inaccurate. Even so, Hahn and Rosenfield [29] proposed a semi-empirical model using the relation between fracture toughness and tensile properties. They characterized the shear strain at the crack tip by a characteristic length  $l^*$ , the width of the plastic zone close to the crack tip under plane strain, which depends on the strain-hardening exponent. Also, they argued that the crack-tip fracture strain  $\varepsilon_f^*$  can be related to the true strain  $\varepsilon_f$  in a tensile test. In this way, the plane-strain fracture toughness  $K_{IC}$  is formulated in terms of tensile properties by combining the various descriptions and correlating the result with existing measurements:

$$K_{IC} = \text{const.} \sqrt{E \cdot \sigma_{ys} \cdot n^2 \cdot \varepsilon_f^*} \quad (2-14)$$

where  $E$  is Young's modulus,  $n$  is the strain-hardening exponent, and  $\varepsilon_f$  is the true strain at fracture of a smooth tensile specimen. This expression is accurate to within about 30% for eleven different aluminum, titanium, and steel alloys.

The model of Hahn and Rosenfield contains only macroscopic parameters.

The influence of microstructure on fracture toughness is therefore only implicit, i.e. by its effect on these parameters. An obvious extension of the model is to incorporate the observed behavior of microvoid nucleation and coalescence. This can be done by specifying that the average strain over the distance  $d$  between particles must equal  $\varepsilon_f^*$  for fracture to occur. Several relationships among fracture toughness, particle spacing, and other material properties have been derived [28,56-58] that incorporate the influence of microstructure in different ways: as microvoid diameter [56], dispersoid spacing [57], grain size [28], area fraction of coarse voids [58], and the like.

Barsom [59] suggested determining fracture toughness by the mechanical properties near the crack tip. He assumed that the fracture strain near the tip of a crack is the same as in a plane-strain tension specimen. Using the relation between the crack-tip strain and the crack-tip opening displacement, the plane-strain fracture toughness is approximated by:

$$K_{IC} = A \sqrt{\sigma_{ys}} \varepsilon_f^2 \quad (2-15)$$

where  $A$  is a material constant and  $\varepsilon_f$  is the plane-strain tensile ductility.

In addition, Teleshov et al. [60] and Oleinik et al. [61] proposed an empirical relation between the fracture toughness  $K_{IC}$  and mechanical

properties such as tensile strength and percent elongation. From a hypothesis relating the fracture toughness and the thermo-activation energy of plastic deformation at the crack tip for BCC metals and alloys, Said and Tasgetiren [62] expressed the fracture toughness as a function of some mechanical properties and microstructure. Their model has the advantage of covering both quasi-static and dynamic loading. Baron [63] described the empirical relation among crack resistance, Brinell hardness, and yield strength of steels at various temperatures and deformation rates.

However, most alternative approaches to characterizing the fracture behavior have not been generally accepted because the value of fracture toughness is intended to provide a conservative assessment, particularly with regard to fitness for service. Thus, although most codes and specifications were developed using principles of fracture mechanics, the specific fracture-toughness tests specified for material purchase or quality control are given in terms of auxiliary test specimens, such as the CVN (Charpy V-Notch) impact test specimen. Many correlations have been developed using a wide variety of test specimens. However, because the CVN test specimen has been the most widely used quality-control and specification specimen, correlations have been proposed primarily to relate the CVN test to  $K_{IC}$  results. Such correlations are summarized in Table 2-2 [64].

Hardness or instrumented indentation testing is commonly used to measure

the mechanical performance of materials. In the 1950s, Palmquist [23] recognized that the indentation-induced cracking observed on cermets was related to fracture toughness and developed a procedure to predict fracture toughness. Predicted values of fracture toughness for many brittle materials using empirical formulations from indentation theory can be found in the literature [65-69]; details are given in Section 2.2.3.

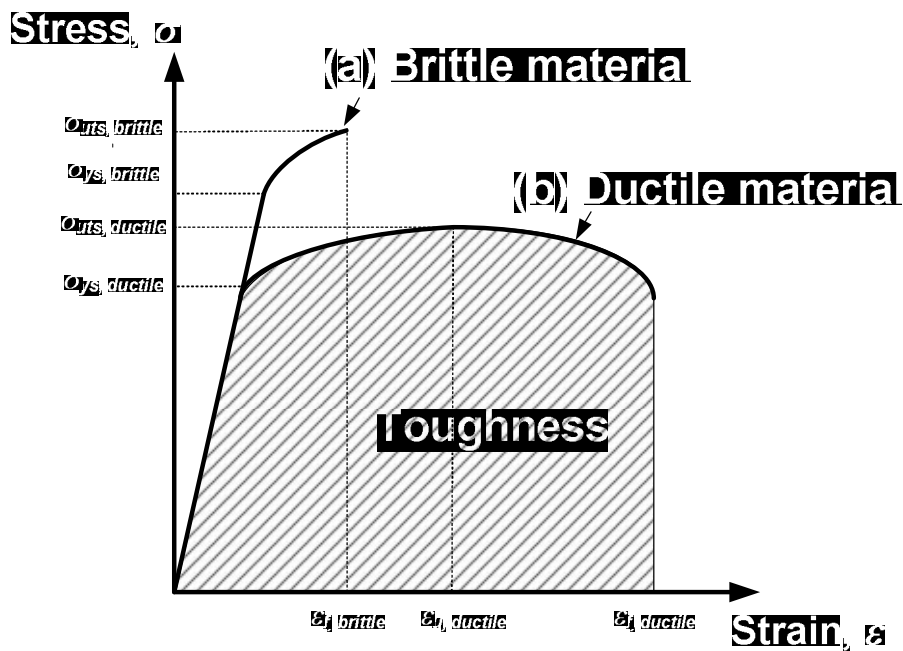


**Figure 2.10** Schematic of typical stress-stain curves

**Table 2.2 Fracture Toughness-Charpy energy correlations [64]**

Material	Notch	Test	Temperature Range	Range of Charpy Results	Yield Strength Range (MPa)	Correlation
A517D 4147 HY 130 4130 12 Ni-5Cr-3Mo 18 Ni-8Co-3Mo	V-Notch	Impact	Upper Shelf	31-121	760-1700	$\frac{K_{lc}^2}{\sigma_{ys}} = 0.64 \left( \frac{CVN}{\sigma_{ys}} - 0.01 \right)$
High-Strength Steels	V-Notch	Impact	Upper Shelf	15-28.6	1610-1980	$\frac{K_{lc}^2}{\sigma_{ys}} = 0.18 \frac{CVN}{\sigma_{ys}} - 0.0011$
A517F A3202B ABS-C HY-130 18 Ni (250) Ni-Cr-Mo-V Cr-Mo-V Ni-Mo-V	V-Notch	Impact	Transition	4-82	270-1700	$\frac{K_{lc}^2}{E} = 0.22(CVN)^{1.5}$
A533B A517F A542	V-Notch	Impact	Transition	7-68	410-480	$K_{Ic} = 14.6(CVN)^{0.5}$
En25 3% Ni-Cr-Mo-V	V-Notch	Impact	Transition	6-55	820-1420	$K_{lc} = 18.2 \frac{CVN^{0.5}}{A}$
HY60 Ti 3 Ti 6	V-Notch	Impact	Transition & Upper Shelf	5-125	400-560	$K_c = 15 \frac{CVN^{0.543}}{A}$
ABS-C A305-B A517-F	V-Notch	Impact Slow Bend	Transition	2.7-61	250-345	$\frac{K_{ld}^2}{E} = 0.64CVN$ $\frac{K_{lc}^2}{E} = 0.64CSB$
ABS-C A305-B A517-F A533-B	V-Notch	Impact	Transition	3-95	270-815	$K_{ld} = 15.5(CVN)^{0.375}$
A533-73 2.25% Cr-1Mo C-Mn-Nb-V 12MDV C4-03M	V-Notch	Impact	Transition	5-50	303-820	$K_{ld} = 19(CVN)^{0.5}$
ABS-C A302-B A517F	Precracked	Impact Slow Bend	Transition	2.7-61	250-345	$\frac{K_{ld}^2}{E} = 0.52PCI$ $\frac{K_{lc}^2}{E} = 0.52PSB$
HY60	Precracked	Impact	Transition	16-40	400	$K_c = 25 \frac{PCI^{0.5}}{A}$

## **2.2. Instrumented Indentation Technique**

### **2.2.1. Introduction**

The instrumented indentation technique started from the conventional hardness tests such as Vickers and Brinell hardness testing, etc. Conventional hardness testing measures hardness only from the residual imprint size, and thus shows the resistance of the material to penetration. In instrumented indentation testing, however, the applied load and the depth of penetration of an indenter into the specimen are recorded simultaneously and used to indirectly determine the area of contact from the indentation load-depth curve and hence the hardness of the test material [1-4]. The contact equations also allow determination of the specimen elastic modulus [1-4]. Other properties such as the yield strength, tensile strength, strain-hardening exponent [16, 17], fracture toughness [28,30-32], and residual stress [18-22] can also be obtained in some circumstances.

The merits of instrumented indentation technique are 1) its simplicity, 2) its applicability to microstructural constituents using micro or nanoindentation, 3) its cost-effectiveness since only small specimens are needed, and 4) its nondestructiveness on a macroscale, which makes on-site testing possible. Although it is difficult to make comparisons with the conventional

mechanical test, specimen preparation is somewhat time-consuming since a polished surface is required so that uniform indentations are made on a reflective flat plane, which is necessary in order to obtain consistent and reproducible results.

Depending on the applied load range, instrumented indentation testing is classified into three categories: macro, micro, and nano. Macroindentation is used mainly in the safety assessment of in-service components due to its nondestructiveness. Micro or nanoindentation is now one of the most powerful tools for evaluating material properties and deformation behavior at small scales, such as thin films, MEMS, and bio-tissues.

Over the past decade, standardizations for instrumented indentation have been actively discussed worldwide. ISO 14577-1 [83], the most fundamental standard, specifies not only the method of instrumented indentation testing for hardness and material parameter, but also methods for verification and calibration of the testing machine. Section ISO 14577-4 [84], which describes a method for testing coatings that is particularly suitable for testing in the micro/nano range applicable to thin coatings, is also under discussion. In addition, a new ISO technical report, TR 29381:2008 [85], describes three methods by which instrumented indentation tests can determine the tensile properties of metallic materials. Of three methods, the representative stress and strain method has been being developed in our laboratory since 2003,

including a procedure given in an appendix for evaluating residual stress using instrumented indentation tests.

## 2.2.2. Applications

### 2.2.2.1. Hardness and elastic modulus

A schematic representation of a typical data set obtained with a sharp indenter such as Vickers and Berkovich indenter appears in Figure 2.14(a), where the parameter  $P$  designates the load and  $h$  the displacement relative to the initial undeformed surface. For modeling purposes, deformation during loading is assumed to be both elastic and plastic in nature as the permanent hardness impression forms. During unloading, it is assumed that only the elastic displacements are recovered; it is the elastic nature of the unloading curve that facilitates the analysis. For this reason, the method does not apply to materials in which plasticity reverses during unloading. However, finite element simulations have shown that reverse plastic deformation is usually negligible [86]. There are three important quantities that must be measured from the  $P$ - $h$  curves: the maximum load,  $P_{\max}$ , the maximum displacement,  $h_{\max}$ , and the elastic unloading stiffness,  $S=dP/dh$ , defined as the slope of the upper portion of the unloading curve during the initial stages of unloading (also called the contact stiffness). The accuracy of hardness and modulus measurement depends inherently on how well these parameters can be measured experimentally. Another important quantity is the final depth,  $h_f$ ,

the permanent depth of penetration after the indenter is fully unloaded.

The analysis used to determine the hardness,  $H$ , and elastic modulus,  $E$ , is essentially an extension of the method proposed by Doerner and Nix [1] that takes into account the fact that unloading curves are distinctly curved in a manner that cannot be explained by the flat-punch approximation. In the flat-punch approximation used by Doerner and Nix, the contact area remains constant as the indenter is withdrawn, and the resulting unloading curve is linear. In contrast, experiments have shown that unloading curves are distinctly curved and usually well approximated by the power law relation

$$P = \alpha (h - h_f)^m \quad (2-16)$$

where  $\alpha$  and  $m$  are power-law-fitting constants [2].

The exact procedure used to measure  $H$  and  $E$  is based on the unloading processes shown schematically in Figure 2.15, in which it is assumed that the behavior of the Berkovich indenter can be modeled by a conical indenter with a half-included angle,  $\theta$ , that gives the same depth-to-area relationship,  $\theta = 70.3^\circ$ . The basic assumption is that the contact periphery sinks in in a manner that can be described by models for indentation of a flat elastic half-space by rigid punches of simple geometry [87-91]. This assumption limits the applicability of the method since it does not take into account the pile-up

of material at the contact periphery that occurs in some elastic-plastic materials. Assuming, however, that pile-up is negligible, the elastic models show that the amount of sink-in,  $h_d$ , is given by

$$h_d = \omega \frac{P_{max}}{S} \quad (2-17)$$

where  $\omega$  is a constant that depends on the geometry of the indenter; important values are:  $\omega = 0.72$  for a conical punch,  $\omega = 0.75$  for a parabola of revolution (which approximates to a sphere at small depths), and  $\omega = 1.00$  for a flat punch [87].

Using Eq. (2-17) to approximate the vertical displacement of the contact periphery, it follows from the geometry of Figure 2.15 that the depth along which contact is made between the indenter and the specimen,  $h_c = h_{max} - h_d$ , is

$$h_c = h_{max} - \varepsilon \frac{P_{max}}{S} \quad (2-18)$$

Letting  $F(d)$  be an area function that describes the projected (or cross-sectional) area of the indenter at a distance  $d$  back from its tip, the contact area  $A$  is then

$$A = F(h_c) \quad (2-19)$$

The area function, also sometimes called the indenter shape function, must be carefully calibrated by independent measurements so that deviations from non-ideal indenter geometry are taken into account. These deviations can be quite severe near the tip of the Berkovich indenter, where some rounding inevitably occurs during the grinding process.

Once the contact area is determined, the hardness is estimated from

$$H = \frac{P_{max}}{A} \quad (2-20)$$

Note that because this definition of hardness is based on the contact area under load, it may deviate from the traditional hardness measured from the area of the residual hardness impression if there is significant elastic recovery during unloading. However, this is generally important only in materials with extremely small values of  $E/H$  [20].

Measurement of the elastic modulus follows from its relationship to contact area and the measured unloading stiffness through the relation

$$S = \beta \frac{2}{\sqrt{\pi}} E_r \sqrt{A} \quad (2-21)$$

where  $E_r$  is the reduced modulus. The effective elastic modulus takes into account the fact that elastic displacements occur in both the specimen, with Young's modulus  $E$  and Poisson's ratio  $\nu$ , and the indenter, with elastic constants  $E_i$  and  $\nu_i$ . Note that Eq. (2-21) is a very general relation that applies to any axisymmetric indenter [92, 93]. It is not limited to a specific sample geometry, even though it is often associated with flat punch indentation. Although originally derived for elastic contact only [94], it has subsequently been shown to apply equally well to elastic-plastic contact [95], and that small perturbations from pure axisymmetry geometry do not affect it [96]. It is also unaffected by pile-up and sink-in.

### 2.2.2.2. Indentation tensile properties

The algorithm for evaluating tensile properties has four steps: step 0 — determine real contact area; step 1 — define representative stress and strain; step 2 — fit to constitutive equation; and step 3 — evaluate tensile properties. Details are as follows.

Figure 2.14(b) shows a typical indentation load-depth curve obtained during

instrumented spherical indentations on steel. Unlike curves from sharp indentation using a pyramidal indenter, such loading curves are quite linear due to the counterbalance of spherical geometry and work-hardening in tested steel. Several depths are defined from this curve. The maximum indentation depth  $h_{max}$  is the total displacement of the material and the indenter at maximum load  $L_{max}$ , including elastic and plastic deformation. In unloading, elastic deformation is the indentation stiffness of the specimen and the indenter S. Thus, the final depth  $h_f$  is the plastic deformation of the material.

A contact depth  $h_c^*$  at maximum indentation load can be evaluated by analyzing the unloading curve using the concepts of indenter geometry and elastic deflection [2]:

$$h_c^* = h_{max} - \omega (h_{max} - h_i) \quad (2-22)$$

where  $h_i$  is the intercept indentation depth and the indenter shape parameter is 0.75 for a spherical indenter. The material pile-up around the indentation enlarges the contact radius (from the analysis of elastic deflection) by an extent that is determined by the work-hardening exponent  $n$  and the ratio of the maximum indentation depth and indenter radius  $h_{max}/R$  [4]:

$$h_{pile}^* = h_c^* \cdot f(n, h_{max}/R) \quad (2-23)$$

where  $h_{pile}^*$  is the plastic pile-up depth.

The mean pressure  $p_m$  obtained by dividing the maximum load  $L_{max}$  by the contact area  $\pi a_c^2$  is well known to be about three times the representative stress  $\sigma_R$  for fully plastic deformation of steels [4]. In other words, the representative stress can be expressed as:

$$\sigma_R = \left(\frac{1}{\psi}\right) P_m = \left(\frac{1}{\psi}\right) \left(\frac{L_{max}}{\pi a_c^2}\right) \quad (2-24)$$

where  $\psi$  is a plastic constraint factor, here taken as 3, and  $a_c$  is the contact area. On the basis of the deformation shape and strain distribution under a spherical indenter, Ahn and Kwon [16] proposed a new definition using the tangent function and a strain-proportional constant,  $\alpha$ :

$$\varepsilon_R = \left(\frac{\alpha}{\sqrt{1 - (a_c/R)^2}}\right) \left(\frac{a_c}{R}\right) = \alpha \tan \gamma \quad (2-25)$$

where  $\alpha$  was determined as 0.14 by finite element analysis for various materials [97],  $R$  is the indenter radius and  $\gamma$  is the half-angle between the

indenter and the material. The true stress and strain points obtained from the indentation test are then fitted to a constitutive equation by a simple power-law-type Hollomon equation:

$$\sigma = K \cdot \varepsilon^n \quad (2-26)$$

where  $n$  is the work-hardening exponent and the gradient of the curve,  $K$  is the strength coefficient, and  $\sigma$  and  $\varepsilon$  are respectively the representative stress and strain values. This approach assumes that the flow curve of many metals in the uniform plastic deformation region can be expressed by Eq. (2-26). With most materials there is a gradual transition from elastic to plastic behavior, and the point at which plastic deformation begins is hard to define with precision. Although there are various criteria for the initiation of yielding, a yield strength obtained by an offset method is commonly used for design and specification purposes because it avoids the practical difficulties of measuring the elastic limit or proportional limit [98]. Thus, the yield strain can be determined as the intersection point of an elastic line whose slope is the elastic modulus 0.2% offset from the origin and a plastic curve of the constitutive equation. The uniform tensile strain should be same as the work-hardening exponent, by the theory of instability in tension [98], and from this the indentation tensile strength can be determined. The indentation yield

strengths and the indentation tensile strengths lie within 10% and 5% errors of those from uniaxial tensile tests, respectively [17, 99].

### 2.2.2.3. Residual Stress

Indentation hardness as analyzed from the indentation  $P$ - $h$  curve changes with the material residual stress: indentation  $P$ - $h$  curves are shifted in the direction and with the magnitude of the residual stress within the tested material. However, the variations in apparent indentation hardness with changes in residual stress have been identified as an artifact of erroneous optical measurements of the indentation imprint [18, 19]: in a study of the influence of in-plane stress on indentation plasticity that investigated both the shape of the indentation curve and the contact impressions, the contact hardness was found to be invariant regardless of the elastically applied stress (residual stress) [18, 19]. The FEA results showed the important role of sink-in or pile-up deformations around the contact in the stressed state in producing the stress-insensitive contact hardness [20]. Therefore, the change in contact morphologies with residual stress was modeled for constant maximum indentation depth assuming the independence of intrinsic hardness and residual stress [21].

The change in indentation deformation caused by the residual stress was

identified in the indentation loading curve in Figure 2.16. The applied load in the tensile-stressed state is lower than that in the stress-free state for the same maximum indentation depth [18, 19, 21]. In other words, the maximum indentation depth desired is reached at a smaller indentation load in a tensile-stressed state because a residual-stress-induced normal load acts as an additive load to the applied load. Therefore, the residual stress can be evaluated by analyzing the residual-stress-induced normal load.

The detailed changes in contact morphology can be seen in the schematic diagram in Figure 2.17. The residual stress is relaxed from a tensile-stressed state to a stress-free state while maintaining the constant maximum depth,  $h_{max}$ , as the stress relaxation pushes the indenter out from the surface. The pushing force appears as an increase in the applied load ( $L_T \rightarrow L_0$ ) and the contact depth ( $h_c^T \rightarrow h_c$ ), because the maximum depth is held constant. The indentation load and maximum depth for the tensile-stressed state ( $L_T, h_{max}$ ) are equivalent to those in the relaxed state ( $L_0, h_{max}$ ). Thus, the relationship between the two states can be expressed as

$$L_0 = L_T + L_{res} \quad (2-27)$$

In the compressive stress state, the applied load and contact depth decrease by stress relaxation under the maximum-depth-controlled path. Furthermore,

this decreasing portion of the applied load was the residual-stress-induced normal load,  $L_{\text{res}}$ . Therefore, the residual stress in a welded joint can be evaluated by dividing  $L_{\text{res}}$  by the contact area,  $A_C$ , regardless of the stress state [22]:

$$\sigma_{\text{res}} = \alpha \frac{L_{\text{res}}}{A_c} \quad (2-28)$$

where  $\alpha$  is a constant related to the stress directionality of biaxial residual stress. The biaxial stress state, in which  $\sigma_y = k\sigma_x$ , can be divided into a mean stress term and plastic-deformation-sensitive shear deviator term [22]:

<u>Biaxial stress</u>	<u>Mean stress</u>	<u>Deviator stress</u>
$\begin{pmatrix} \sigma_x^{\text{res}} & 0 & 0 \\ 0 & \sigma_y^{\text{res}} & 0 \\ 0 & 0 & 0 \end{pmatrix}$	$= \begin{pmatrix} \frac{1+k}{3}\sigma_x^{\text{res}} & 0 & 0 \\ 0 & \frac{1+k}{3}\sigma_x^{\text{res}} & 0 \\ 0 & 0 & \frac{1+k}{3}\sigma_x^{\text{res}} \end{pmatrix} + \begin{pmatrix} \frac{2-k}{3}\sigma_x^{\text{res}} & 0 & 0 \\ 0 & \frac{2-k}{3}\sigma_x^{\text{res}} & 0 \\ 0 & 0 & -\frac{1+k}{3}\sigma_x^{\text{res}} \end{pmatrix}$	(2-29)

The stress component parallel to the indentation axis in the deviator stress term directly affects the indenting plastic deformation. A residual-stress-induced normal load  $L_{\text{res}}$  can be defined from the selected deviator stress component as:

$$L_{res} = \frac{1+k}{3} \sigma_{res} A_c \quad (2-30)$$

Therefore,  $\alpha$  in Eq. (2-28) can be taken as approximately 1.5 in the equibiaxial stress state. In the instrumented indentation test, the contact area is determined by unloading curve analysis. By differentiation of the power-law-fitted unloading curve at maximum indentation depth, the contact depth and contact area can be calculated from the contact depth based on the geometry of the Vickers indenter as [2]:

$$A_c = 24.5 h_c^2 \quad (2-31)$$

Thus, residual stress was calculated from the analyzed contact area in Eq. (2-30) and the measured load change  $L_{res}$  by the effect of residual stress in Eq. (2-27).

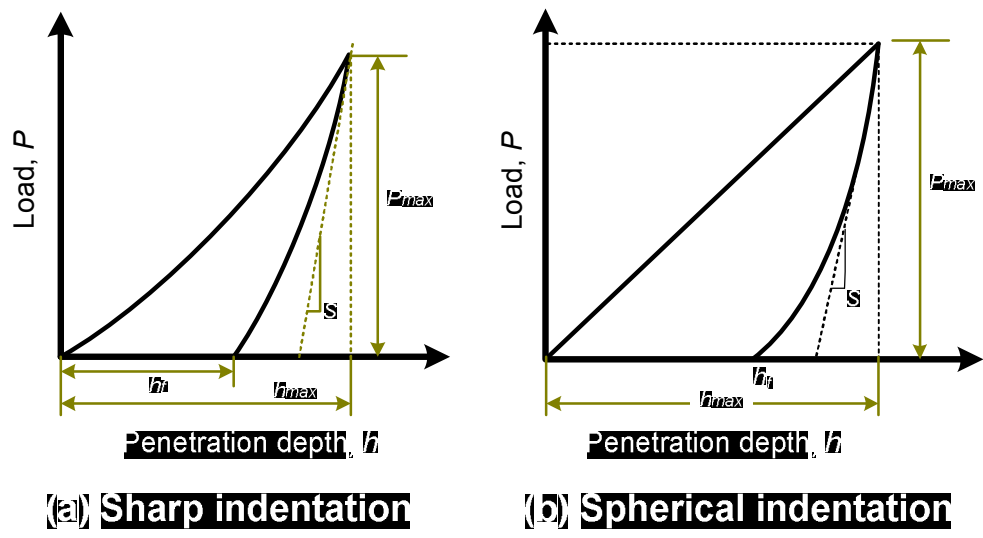


**Figure 2.14** Schematic diagram of typical load-depth curve obtained during instrumented indentations

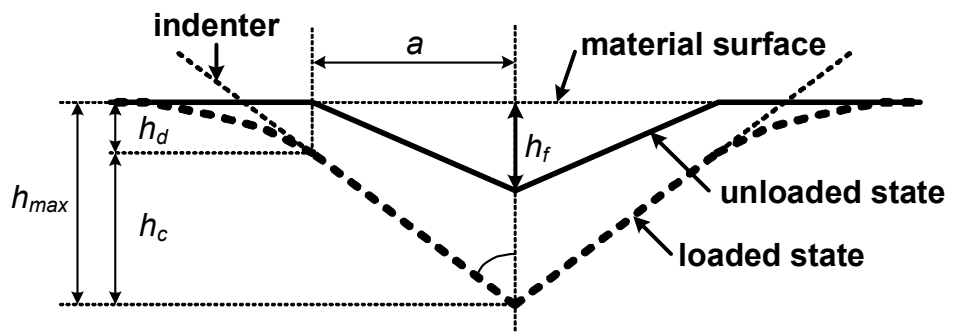


**Figure 2.15** Cross section of contact morphology in the loaded state and residual indent after unloading by a sharp indenter

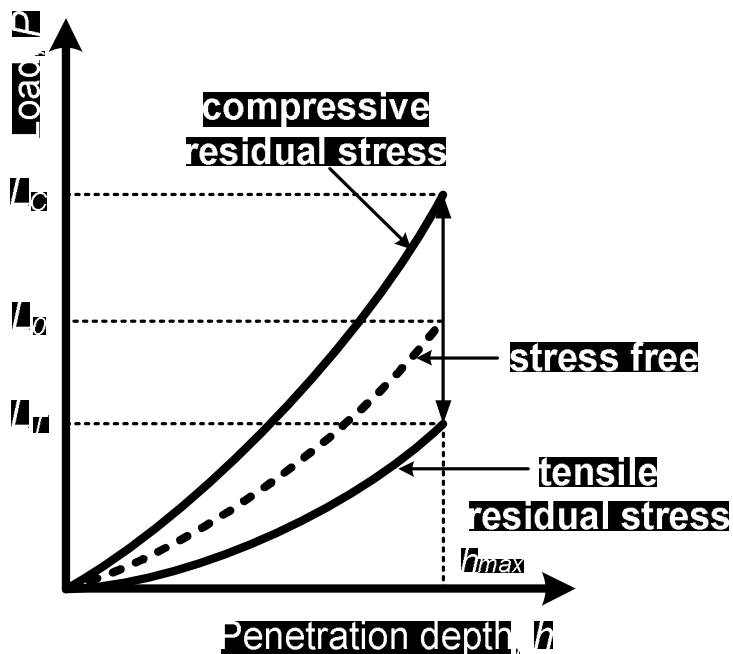


**Figure 2.16** Variation of indentation loading curves with changes in the stress state

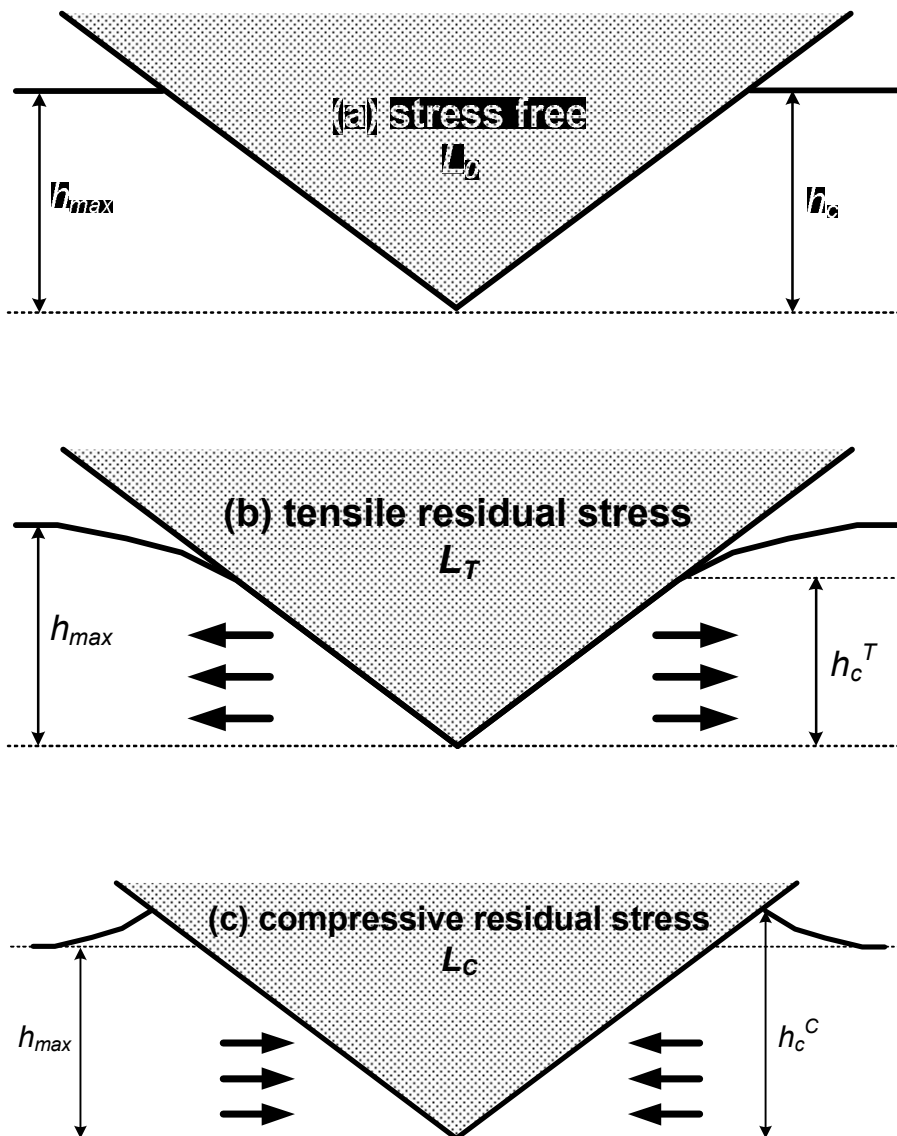


**Figure 2.17** Theoretical surface morphologies around the contact for (a) stress-free, (b) tensile stress, and (c) compressive stress states

### **2.2.3. Indentation fracture toughness**

#### **2.2.3.1. Indentation cracking methods**

Instrumented indentation can be used to evaluate the fracture toughness of materials and interfaces in a similar manner to that conventionally used in larger-scale testing. During loading, tensile stresses are induced in the specimen material as the radius of the plastic zone increases. Upon unloading, additional stresses arise as the elastically strained material outside the plastic zone attempts to resume its original shape but is prevented from doing so by the permanent deformation associated with the plastic zone. There exists a large body of literature on the subject of indentation cracking with Vickers and other sharp indenters.

The various types of crack are illustrated in Figure 2-18 [73]. Radial cracks are vertical half-penny type cracks that occur on the surface of the specimen outside the plastic zone and at the corners of the residual impression at the indentation site. These radial cracks are formed by a hoop stress and extend downward into the specimen but are usually quite shallow.

Lateral cracks are horizontal cracks that occur beneath the surface and are symmetric with the load axis. They are produced by a tensile stress and often extend to the surface, resulting in a surface ring that may lead to chipping of

the specimen surface. Median cracks are vertical circular penny cracks that form beneath the surface along the axis of symmetry and have direction aligned with the corners of the residual impression. Depending on the loading conditions, median cracks may extend upward and join with surface radial cracks, thus forming two half-penny cracks that intersect the surface, as shown in Figure 2-18(d). They arise due to the action of an outward stress. The exact sequence of initiation of these three types of cracks is sensitive to experimental conditions. However, it is generally observed that in soda-lime glass loaded with a Vickers indenter, median cracks initiate first. When the load is removed, the elastically strained material surrounding the median cracks cannot resume its former shape owing to the presence of the permanently deformed plastic material, and this leads to a residual impression in the surface of the specimen.

Residual tensile stresses in the normal direction then produce a horizontal lateral crack that may or may not curve upward and intersect the specimen surface. Upon reloading, the lateral cracks close and the median cracks reopen. For low indenter loads, radial cracks also form during unloading (in other materials, radial cracks may form during loading). For large loads, upon unloading, the median cracks extend outward and upward and may join with the radial cracks to form a system of half-penny cracks, which are then called median/radial cracks. In glass, the observed cracks at the corners of

the residual impression on the specimen surface are usually fully formed median/radial cracks.

It is the radial and lateral cracks that are of particular importance, since their proximity to the surface has a significant influence on the fracture strength of the specimen. Fracture mechanics treatments of these types of cracks seek to provide a measure of fracture toughness based on the length of the radial surface cracks. Attention is usually given to the length of the radial cracks as measured from the corner of the indentation and then radiates outward along the specimen surface, as shown in Figure 2-19.

Palmqvist [23] stated that the crack length was a linear function of the indentation load. Lawn, Evans, and Marshall [27] formulated a different relationship: they treated the fully formed median/radial crack and found the ratio  $P/c^{3/2}$  (where  $c$  is measured from the center of contact to the end of the corner radial crack) is a constant, the value of which depends on the specimen material. Fracture toughness is found from:

$$K_c = \alpha \left( \frac{E}{H} \right)^{1/2} \left( \frac{P_{max}}{c^{3/2}} \right) \quad (2-32)$$

where  $\alpha$  is an empirical calibration constant dependent on the geometry of the indenter. It was found that  $\alpha = 0.016$  gives good correlation between the

toughness values measured from the crack length and those obtained using more conventional methods [100]. An attractive feature of this method is that both  $H$  and  $E$  can be determined directly from analyses of indentation force-depth data. Thus, provided one has a way to measure crack lengths, implementing the method is relatively straightforward.

### **2.2.3.2. Indentation fracture toughness models for ductile materials**

#### **1) Critical strain model**

Ju [31] modified the critical strain model proposed by Hahn and Rosenfield [29] to evaluate ductile fracture toughness using the mechanical properties measured from instrumented indentation tests. The modification of the critical strain model involved: 1) the use of fracture strain from the newly developed model, involving the stress state, i.e. stress triaxiality, and a deformation parameter that can be determined from indentation tests, instead of the critical strain at ahead of crack tip, and 2) the assumption of an empirical calibrated value for the characteristic length,  $l^*$ , as a function of the strain-hardening exponent [29]. To determine the fracture strain, he adopted the void growth rate in a rigid-perfectly plastic material proposed by Rice and Tracey [101]. Integrating, the fracture strain is given by:

$$\varepsilon_f = \ln\left(\frac{R_f}{R_i}\right) / 0.32 \exp\left(1.5 \frac{\sigma_m}{\sigma}\right) \quad (2-33)$$

where  $R_f$  and  $R_i$  are the final and initial void radius and  $\sigma_m$  and  $\sigma$  are the mean normal stress and the equivalent stress, respectively. Ju has shown experimentally that the ratio of void volume can be expressed by the reciprocal of the strain-hardening exponent. Also, the stress ratio is defined as the indentation parameter with regard to deformation. Thus, the critical fracture strain is expressed by:

$$\varepsilon_f = f\left(\frac{1}{n}\right) \exp\left(1 - \frac{6A5^n}{\pi \cdot K}\right) \quad (2-34)$$

where  $A$  is the material yield parameter,  $n$  is the strain-hardening exponent, and  $K$  is the strength coefficient. From the relation between the characteristic length and strain-hardening exponent [29], the modified critical strain model can be defined as:

$$K_{IC} = \text{const.} \sqrt{E \cdot \sigma_{ys} \cdot n^2 \cdot f\left(\frac{1}{n}\right) \exp\left(1 - \frac{6A5^n}{\pi \cdot K}\right)} \quad (2-35)$$

where the constant is determined experimentally.

## 2) Continuum damage model

From Griffith theory [34], the relation of the fracture energy  $w_f$  and plane strain fracture toughness  $K_{IC}$  is expressed as:

$$K_{IC} = \sqrt{2Ew_f} \quad (2-36)$$

where E is the elastic modulus. To estimate  $K_{IC}$  on the basis of Eq. (2-36) by using the indentation technique,  $w_f$  must be determined using only indentation parameters. Triaxiality ahead of the indenter tip is in the range 2~3, and the degree of constraint in the deformed indentation region is similar to that ahead of the crack tip [30, 32, 102]. Hence the indentation energy per unit contact area at the characteristic point can be related to  $w_f$  if there is a characteristic fracture initiation point during the indentation process. This energy, henceforth called the critical indentation energy, is calculated from the indentation load-depth curve:

$$2w_f = \lim_{h \rightarrow h^*} \int_0^h \frac{4P}{\pi d^2} dh \quad (2-37)$$

where  $P$  is the applied load,  $h$  is the indentation depth,  $d$  is the chordal diameter of the impression and  $h^*$  is the critical indentation depth corresponding to the characteristic fracture initiation point.  $2w_f$  indicates the formation of two crack surfaces.

Since there are no distinguishing marks that can be used to identify fractures occurring during indentation,  $h^*$  in Eq. (2-37) cannot be measured by direct methods (optical microscope or SEM observation). Thus to determine  $h^*$ , continuum damage mechanics (CDM) was applied to the indentation process. CDM is used mainly to predict failure in structures loaded statically and dynamically. According to Lemaître's strain equivalence principle [103], a damage variable  $D$  can be represented as:

$$E_{eff} = E(1 - D) \quad (2-38)$$

where  $E_{eff}$  is the effective elastic modulus of the damaged material and  $E$  is the elastic modulus of the initial non-damaged material.  $E_{eff}$  decreases as  $h$  increases due to the increase in damage beneath the indenter [32]. In addition,  $E_{eff}$  is represented by a function comprised only of indentation parameters in Eq. (2-38)

From multiple loading-unloading cycles, the values of  $E_{eff}$  for various indentation depths can be calculated from each unloading and  $E_{eff}$  vs.  $h$  may

be plotted as in Figure 2.20. If a critical value of the elastic modulus is determined,  $h^*$  can be determined from the corresponding value of  $h$ . Since the indentation load is compressive in terms of the loading axis, the deformed region beneath the indenter experiences compressive stress. Hence, voids will be nucleated by localized shear due to compressive stress, and the void volume fraction  $f$  will increase as  $h$  increases [104]. Then  $D$  can be represented in terms of  $f$  as [103]:

$$D = \frac{\pi}{(1.3\pi)^{2/3}} f^{2/3} \quad (2-39)$$

From previous experimental and computational research [105, 106], the void volume fraction,  $f$  of two types is established: the values  $f_C = 0.15$  (void volume fraction at onset of coalescence) and  $f_F = 0.25$  (void volume fraction at initiation of stable crack growth). The concept of critical void volume fraction was adopted to determine the critical value of the elastic modulus. Critical CTOD are classified as  $\delta_C$ ,  $\delta_U$  and  $\delta_m$ , but ductile structural materials generally have  $\delta_U$  and  $\delta_m$  [47]. Since  $\delta_U$ -type materials are brittle and have poor resistance to strain localization between voids compared to  $\delta_m$  materials, they experience abrupt loss of load-carrying capacity soon after void coalescence begins. On the other hand,  $\delta_m$ -type materials retain load-carrying

capacity even after the onset of void coalescence, showing gradual loss of this capacity at the initiation of stable crack growth. With these phenomena in mind,  $f_C$  is used as the fracture criterion for  $\delta_U$ -type materials and  $f_F$  is used for  $\delta_m$ -type materials. The  $f_C$  and  $f_F$  can be converted into corresponding damage variables  $D_C$  and  $D_F$  through Eq. (2-39); then corresponding values of  $E_C$  and  $E_F$  are calculated by Eq. (2-38). Therefore,  $h^*$  is determined as the corresponding  $h$  by using critical value of elastic modulus,  $E^* = E_C$  for  $\delta_m$ -type materials and  $E^* = E_F$  for  $\delta_U$ -type materials.

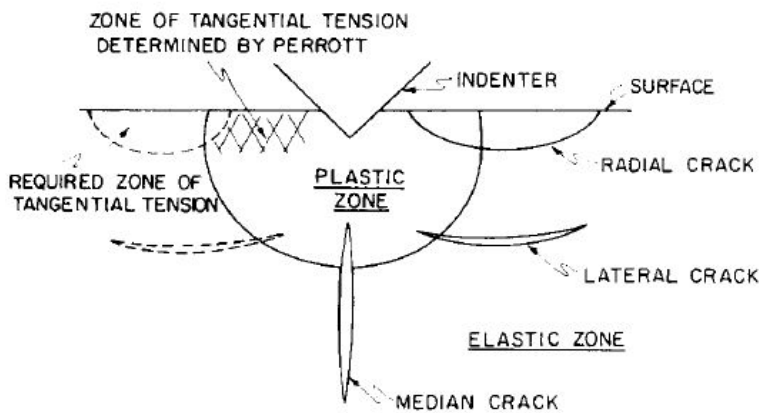


**Figure 2.18** Crack system for Vickers indenter: (a) radial cracks, (b) lateral cracks, (c) median cracks, and (d) half-penny cracks

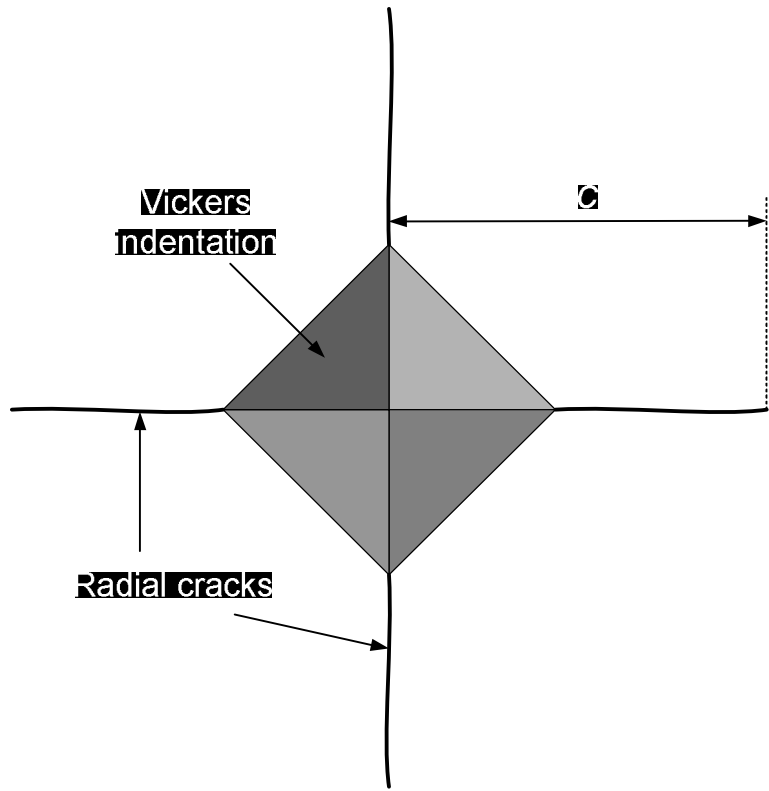


**Figure 2.19** Schematic of radial cracking by Vickers indentation

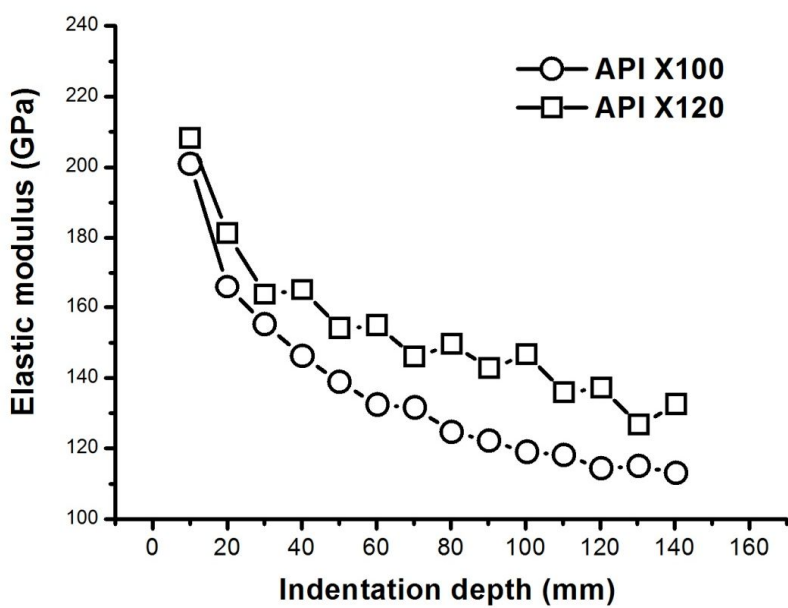


**Figure 2.20** Decreasing elastic modulus with indentation depth (API steels)

## 2.3. Flat Punch Indentation

### 2.3.1. Contact mechanics

#### 2.3.1.1. Elastic models

The problem of the contact of two elastic (spherical) bodies was originally developed by Hertz [70], but the approach to the problem of an elastic half-space subjected to a pressure acting on a closed surface is due to Cerruti [71] and Boussinesq [74], who used the potential theory method, although the solution found cannot be used for problems of a practical interest. Love [75] managed to find a solution for conical and cylindrical indenters. Finally, Sneddon [76] derived the load-displacement relations for an arbitrary shaped axisymmetric punch. The results of the Sneddon solution for the indentation without friction of an elastic half-space by a flat-ended cylindrical punch, can be summarized as follows (see Figure 2.21). The contact area is assumed to be circular and equal to the indenter tip area (radius  $a$ ). The boundary conditions for the formulation ( $z = 0$  for the local system  $r-z$ ) are:

$$\begin{aligned}\sigma_z(r, 0) &= 0, \quad r > a \\ \tau_{rz}(r, 0) &= 0, \quad 0 \leq r \leq a \\ u_z(r, 0) &= h, \quad 0 \leq r \leq a\end{aligned}\tag{2-40}$$

The first condition posits that the free surface outside the contact region has no normal stress ( $\sigma_z$ ) acting on it; the second assures the absence of any friction for the contact region between the indenter and the half space; the third forces the displacement in the  $z$  direction ( $u_z$ ) to be consistent with the flat facet of the punch. Since the punch has a sharp edge,  $\sigma_z \rightarrow \infty$  when  $r = a$ . This condition [77] determines a very localized plasticity on the circular edge that does not invalidate the effectiveness of the elastic relationships found, in particular, the load-displacement and the contact pressure equations. Following a penetration  $h$ , the mean contact pressure  $P_m$  is given by the equation:

$$P_m = \frac{2Eh}{\pi a(1 - \nu^2)}\tag{2-41}$$

which shows that the relationship between  $P_m$  and  $h$  is linear due to the constant contact area.

The distribution of pressure under the punch  $\sigma_z(r \leq a, z = 0)$  is given by the equation:

$$\sigma_z(r, 0) = -\frac{P_m}{2\sqrt{1 - r^2/a^2}} \quad (2-42)$$

and the shape of the deformed boundary  $u_z$  ( $r > a$ ,  $z = 0$ ) by:

$$u\sigma_z(r, 0) = \frac{2h}{\pi} \arcsin \frac{a}{r} \quad (2-43)$$

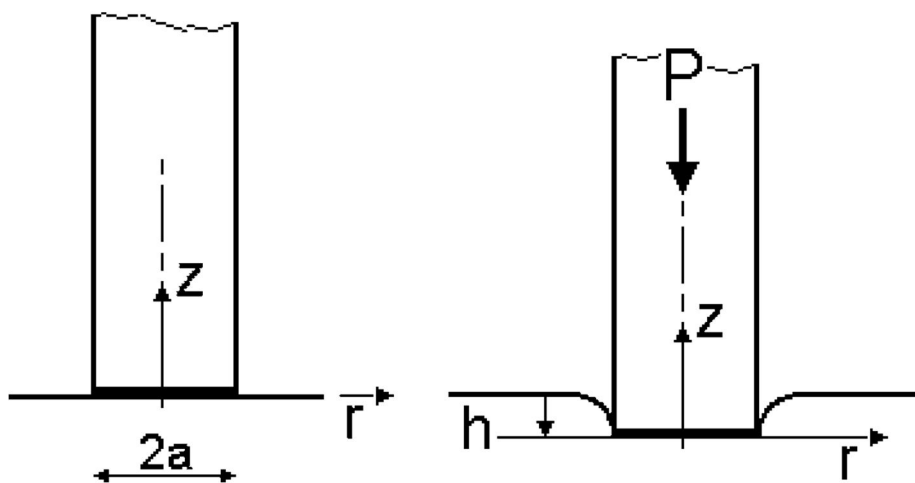


**Figure 2.21** Schematic of flat punch indentation

### **2.3.1.2. Elastic–plastic model**

An indentation model that also includes plasticity is much more complex than a merely elastic model. The complexity is due to the fact that the constitutive equations are not linear and include some material parameters that describe the plastic behavior, such as the yield stress and the work-hardening coefficient.

Two models have been developed to describe the material stress–strain field following an indentation performed by means of punches of different shapes:, the spherical cavity model [78] and the slip-line model [72]. The first was suggested by the consideration that for some indenter shapes, such as the spherical and blunt conical ones, the plastic zone shows spherical symmetry (hemispherical), and thus the problem can be approached on analogy with the elastic–plastic deformation near a cavity subjected to internal pressure. Unfortunately, this model is too rough to be applied to a cylindrical indentation because the plastic region shape varies with penetration depth and becomes roughly spherical only at elevated depth values [79, 80].

The slip-line approach is suitable for modeling material indentation that can be described by means of a rigid plastic model (i.e. no hardening), where the plastic deformation is much higher than the elastic deformation, so that only plastic deformation can be considered. During indentation, and differently

from the spherical cavity model which involves a compressive action, the material is assumed to flow at a constant shear or normal stress under a punch “cutting action” that determines a new surface on the indented specimen. In these conditions, the stress in the flow region can be described by means of slip-line field theory. This approach allows a grid of curvilinear lines to be determined: on this grid, the plastic field can be described by means of a constant simple shear stress and a variable hydrostatic stress. This approach has been successfully applied to solve plane strain indentation (e.g. that produced by a wedge punch) but cannot be used to solve the general axisymmetric problem.

Shield [81] showed that the axisymmetric plastic flow of a rigid-plastic material can be described by a slip-line field if the material follows the Tresca plasticity criterion, assuming the circumferential stress equal to one of the principal stresses in the meridional plane (Haar-von Karman hypothesis). Under these hypotheses, Shield determined the plastic stress field for the indentation of a semi-infinite solid by a smooth flat-ended cylindrical punch. He also extended the plastic stress field outside the punch contact region and estimated the value of the average contact pressure  $P_m = 5.69k$  ( $k$  being the shear strength of the material). In the same conditions, the maximum contact pressure (close to the punch edge) was found to be  $P_{\max} = 7.2k$  and the radial extension of the plastic area is  $1.58a$ .

Afterwards, Eason and Shield [82] studied the indentation of a semi-infinite solid by a rough punch, also evaluating the radial extension and depth of the plastic zone. As already noted, due to the discontinuity of contact pressure under the flat-ended cylindrical punch, the plasticity starts at punch contact edge and then progressively extends with increasing penetration. The result of the Shield–Eason approach is that the plasticity extension reaches the indenter-specimen axis when the mean contact pressure is about six times the shear strength and thus, as a consequence of the Tresca plasticity criterion, when the contact pressure is about three times the tensile yield stress.

### 2.3.1.3. Characteristics of the indentation curve

The typical trend of an experimental indentation curve with the different stages is shown in Figure 2.22. The curves show a trend characterized by an initial linear elastic stage up to a pressure load  $P_L$ . Below  $P_L$  the curve is fully reversible and no permanent deformation occurs on the sample. The linear stage is followed by three plastic stages [107]:

- 1) The first stage is almost linear and ends at a pressure  $P_y$ : the imprint shows permanent sharp edges.
- 2) The second stage occurs for  $P > P_y$  and is characterized by a sudden slope decrease. During this stage the material starts to protrude

around the imprint.

- 3) The third stage shows a trend with an almost constant slope.

For some materials the third stage evidences a saturation pressure load  $P_s$  that is strongly influenced by the penetration rate, while the  $P_y$  load is scarcely affected by this parameter [108]. This result is of great importance in correlating indentation and tensile test results. When the indentation tests are carried out with a penetration rate of 0.1 mm/min or lower, it is possible to compare the indentation results directly with those of tensile tests with a strain rate of  $10^{-3}$  s<sup>-1</sup>; in these conditions it has been observed that the yield stress  $\sigma_y$  is approximately equal to  $P_y/3$ . This result is similar to the result of Yu et al. [109]: that, when plastic flow occurs during a cylindrical indentation, the ratio between indentation pressure and compression (yield) stress is not widely different from the value 3. Moreover, according to the results of Yu et al. [109], the pressure–penetration curves by testing the same material with indenters of different diameters (1.0, 0.8 and 0.7 mm) overlap almost perfectly [110].

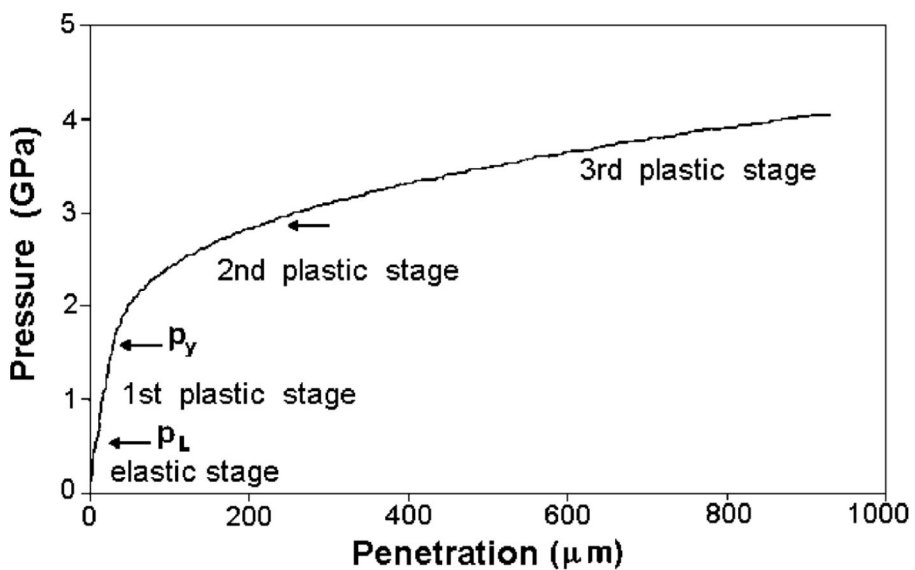


**Figure 2.22** Typical flat punch indentation curve

### **2.3.3. Equivalence with fracture mechanics**

#### **2.3.3.1. Introduction**

The elastic singular fields at the sharp edges of a two-dimensional contact between a rigid flat punch and a planar surface were derived by Sadowski [111]. Subsequently, Nadai [112] analyzed the asymptotic stresses within the elastic substrate in the vicinity of the corners of the punch for both normal and shear loading. Nadai's results confirmed the contact surface stresses predicted by Sadowski for a flat punch, and in addition, the contact stresses derived earlier by Hertz [113] for normal loading of a cylindrical punch. These developments preceded the evolution of the concepts of linear elastic and elastic-plastic fracture mechanics based on the stress intensity factor,  $K$  (e.g. [114]) and the  $J$  integral [115]. Substantial progress has been made in the past five decades in the analysis of crack-tip fields on fracture mechanics principles. Although the singular fields for sharp-edged contacts (e.g. [116-118]) and for cracked bodies (e.g. [119, 120]) suggest similarities (e.g. [121, 122]), it is somewhat surprising that no quantitative connection has been explored in detail, to our knowledge, between the vast literature of contact mechanics and fracture mechanics.

We demonstrate in this chapter a quantitative equivalence as well a broad

connection between the asymptotic stress and strain fields derived by classical analysis for sharp-edged contacts (e.g. [117]) and the crack-tip fields predicted from fracture mechanics methods (e.g. [123]). This equivalence is established by identifying geometries of cracked bodies that facilitate an analogy with contact geometries. In an attempt to validate this “crack analogue”, the following cases are considered:

- 1) A two-dimensional rectangular rigid punch pressed normally against a frictionless flat surface (which is analogous to the compression loading of a double-edge-cracked plate).
- 2) The axisymmetric geometry of a rigid circular cylinder pressed edge-on against a flat surface (which is analogous to a circumferentially cracked cylindrical specimen subjected to normal compressive loading along the cylinder axis).

The conditions governing the validity of the “crack analogue” model to contact mechanics are established by employing the small-scale yielding concepts routinely used in linear elastic fracture mechanics. Because contact between the rigid punch and the substrate implicitly introduces a “fictitious crack length scale”, the problems frequently associated with the identification of an initial crack size can be circumvented. Combinations of elastic properties of the two contacting bodies, which lead to square root singular fields at the contact rim and facilitate the crack analogue approach,

are also identified.

### 2.3.3.2. Theoretical validation

The equivalence between the asymptotic fields for sharp-edged contacts derived from classical contact mechanics analyses and the fields at stationary cracks, as determined from fracture mechanics, is demonstrated in this section for a two-dimensional and a three-dimensional contact geometry. The steps involved in this exercise are as follows for the case of frictionless normal loading.

- 1) Identify the cracked specimen configuration that provides a geometric equivalence for the contact region under a sharp-edged punch that is normally pressed against a planar surface of the same material. A direct geometric correlation is established between the radius of the contact zone (which is a function of the normal load  $P$  and the punch width or diameter  $2a$ ) and the cracked specimen through appropriate coordinate transformation.
- 2) Find the asymptotic solutions to the stress and strain fields at the edges of sharp contacts from classical contact analyses.
- 3) Determine the corresponding stress- and strain-field solutions for the analogous cracked body, from linear elastic fracture mechanics analysis.

Here, invoke the assumption that the cracked body is subjected to a normal compressive load whose magnitude  $P$  is the same as that of the load pressing the punch against the planar surface. The scalar amplitude of the singular fields at the crack tip is the stress intensity factor  $K_I$ .

- 4) Equate the different components of the stress fields determined from steps 2 and 3 and solve for  $K_I$ , which is obtained as a function of  $P$ , the overall geometry of the cracked body, and the characteristic punch dimension.
- 5) Consult any standard text or handbook of fracture mechanics (e.g. [124-126]) and determine the stress intensity factor  $K_I$  as a function of  $P$  and the geometry of the cracked body.
- 6) Show that steps 4 and 5 lead to identical results. This proves the quantitative equivalence between the contact mechanics and fracture mechanics solutions.

An identical result can also be obtained in a slightly different manner. Perform steps 1 and 2 as shown above. Perform the above step 4 next, and from the stress intensity factor so determined, find the mode I crack-tip fields. Show that these fields are identical to those found in step 2.

### 2.3.3.3. Two-dimensional crack analogue

Figure 2.23 schematically shows the two-dimensional contact between a rectangular punch and a flat surfaced substrate. The width of the punch is  $2a$ . Consider the most general loading situation in which the contact interface transmits a compressive normal force  $P$  and a shear force  $Q$  per unit thickness of the contact area (i.e.,  $P$  and  $Q$  have units of force per unit length). Given the symmetry of the contact geometry about the y-z plane, we focus attention at the corner,  $(x, y) = (-a, 0)$  in Figure 2.23, without any loss of generality.

The following assumptions are invoked in the static analysis.

- 1) The substrate, whose depth and width are at least  $6a$  (it is assumed to be semi-infinite), is taken to be linear elastic and isotropic with small-strain deformation at all times.
- 2) Small-scale yield conditions are assumed such that the size of the plastic zone or damage zone,  $r_p$ , at the sharp edges of the contact region is small compared to the width of the contact area, i.e.  $r_p \leq a/20$ .
- 3) Gross sliding does not occur between the punch and the substrate, and any partial slip occurring at the outer edges of the contact area does not significantly alter the asymptotic solutions, which is strictly true for rigid pads on incompressible (i.e. the Poisson ratio,  $\nu = 0.5$ ) or frictionless (i.e. the coefficient of friction,  $\mu = 0$ ) surfaces.

Figure 2.24 illustrates the geometry of a two-dimensional cracked specimen,

which finds an analogy with the punch/substrate contact system shown in Figure 2.23. This cracked plate is infinitely wide and contains double-edge (semi-infinite) cracks whose tips are separated by a distance  $2a$ . The plate is remotely subjected to tensile and shear loads,  $P$  and  $Q$ , respectively, such that they induce mode I and mode II stress intensity factors,  $K_I$  and  $K_{II}$ , respectively, at the crack tips. The  $x^*-y^*$  coordinate axes centered at the contact edge or the crack tip are shown in Figures 2.23 and 2.24.

Note that the stress boundary conditions for the rectangular punch outside the contact area are  $\sigma_{\theta\theta} = \sigma_{r\theta} = 0$ . Within the contact area,  $\varepsilon_{\theta\theta} = 0$ . The former conditions are identical to those of a traction-free crack surface of a mode I flaw in the crack analogue, and the latter condition is identical to that ahead of the crack tip that preserves symmetric mode I deformation. Note also that a constant displacement  $u_z$  occurs throughout the contact area for the rectangular punch; this, however, does not affect the crack-tip stress and strain fields.

The singular stress fields at the sharp edges of the contact between the rectangular rigid punch and the incompressible substrate are known from the asymptotic contact analyses of Sadowski [111] and Nadai [112]. Using the polar coordinates  $(r, \theta)$ , Figure 2.23, the stresses at the left edge  $(-a, 0)$  are found to vary as:

$$\begin{pmatrix} \sigma_{rr} \\ \sigma_{\theta\theta} \\ \sigma_{r\theta} \end{pmatrix} \propto -\frac{3}{4\sqrt{r}} \begin{pmatrix} \sin \frac{3\theta}{2} + 5 \sin \frac{\theta}{2} \\ -\sin \frac{3\theta}{2} + 3 \sin \frac{\theta}{2} \\ \cos \frac{3\theta}{2} - \cos \frac{\theta}{2} \end{pmatrix} \quad (2-44)$$

Using the “crack analogue” transformation (Figure 2.24), we note that

$$\theta \rightarrow \pi - \theta = \varphi; \quad 0 \leq \theta \leq \pi \quad (2-45)$$

Expanding the trigonometric terms in Eq. (2-44), the angular ( $\varphi$  in Figure 2.24) variation of stresses is written as:

$$\begin{pmatrix} \sigma_{rr} \\ \sigma_{\theta\theta} \\ \sigma_{r\theta} \end{pmatrix} \propto \frac{1}{\sqrt{r}} \begin{pmatrix} \cos \frac{\theta}{2} \left(1 + \sin^2 \frac{\theta}{2}\right) \\ \cos^3 \frac{\theta}{2} \\ \sin \frac{\theta}{2} \cos^2 \frac{\theta}{2} \end{pmatrix} \quad (2-46)$$

Note that their stress fields are identical to those derived by Williams [123] for a Mode I crack.

For the calculation of the Mode I stress intensity factor in the crack

analogue, we note that the contact pressure gives the only non-zero component of stress at the contact surface [111]:

$$\sigma_{yy} = -\frac{P}{\pi\sqrt{a^2 - x^2}} \quad (2-47)$$

Taking the asymptote of Eq. (2-47) for the left crack in Figure 2.24,  $x \rightarrow -a$ , we find that

$$\sigma_{yy} \rightarrow -\frac{P}{\pi\sqrt{2ar}}, a + x = r \rightarrow 0 \quad (2-48)$$

The opening stress at the crack tip is related to the stress intensity factor by

$$\sigma_{yy} \rightarrow \frac{K_I}{\sqrt{2\pi r}}, r \rightarrow 0 \quad (2-49)$$

Comparing Eq. (2-48) and (2-49), it is clear that

$$K_I = -\frac{P}{\sqrt{\pi a}} \quad (2-50)$$

This  $K_I$  calibration result agrees with that given in standard fracture mechanics handbooks (e.g. [124-126]) for a double-edge-cracked infinite plate (containing two semi-infinite cracks whose tips separated by a distance of  $2a$ ) loaded remotely with a concentrated symmetric normal load  $P$ .

#### 2.3.3.4. Three-dimensional crack analogue

Sneddon [122] found the elastic solution for a normally loaded axisymmetric rigid punch of circular contact radius  $a$ , shown in Figure 2.25. It is shown in this section that the stress fields of the contact problem are the same as those of the semi-infinite circumferential crack in a right circular, cylindrical rod, Figure 2.26.

Using the cylindrical coordinates  $r, z, \varphi$  in Figure 2.25, the non-zero stresses are

$$\begin{pmatrix} \sigma_{zz} \\ \sigma_{rz} \\ \sigma_{rr} \\ \sigma_{\varphi\varphi} \end{pmatrix} \rightarrow -\frac{P}{2\pi a^2 \sqrt{2s}} \cos \frac{\varphi}{2} \begin{pmatrix} 1 + \sin \frac{\varphi}{2} \sin \frac{3\varphi}{2} \\ \sin \frac{\varphi}{2} \cos \frac{3\varphi}{2} \\ 1 - \sin \frac{\varphi}{2} \sin \frac{3\varphi}{2} \\ 2\nu \end{pmatrix} \quad (2-51)$$

Therefore, all stresses are square root singular with respect to  $s$ , the local

radial coordinate of the “crack analogue”, Figure 2.26.

For the calculation of the Mode I stress intensity factor, we note that the contact pressure gives the only non-zero stress at the surface, e.g. [117],

$$\sigma_{zz} = -\frac{P}{2\pi a \sqrt{a^2 - r^2}} \quad (2-52)$$

The first of Eq. (2-51) is the correct asymptote of Eq. (2-52) as  $r \rightarrow a-$ . From

$$\sigma_{zz} = -\frac{K_I}{\sqrt{2\pi(a-r)}} \quad (2-53)$$

we readily conclude

$$K_I = -\frac{P}{2a\sqrt{\pi a}} \quad (2-54)$$

This result is the same as that in [124-126] for a circular semi-infinite crack located along the circumference of a cylindrical rod (with an uncracked ligament of radius  $a$ ) loaded remotely with a concentrated normal load  $P$ , Figure 2.26. Eq. (2-51) also provide stress distributions that are identical to those for the fields ahead of a circumferentially located crack in a cylindrical rod (where the crack depth  $\gg$  uncracked ligament radius).

### 2.3.3.5. Limits of the linear elastic crack analogue

The elastic solutions predict that stress singularities develop at the contact perimeter and that such stresses will inevitably lead to plasticity or damage at this location. It should be emphasized that the asymptotic forms presented in the preceding section are valid only in the region around the contact edges.

In order to assess quantitatively the difference between the contact mechanics and the asymptotically matched fracture mechanics fields, consider the tensile opening stresses given by Eq. (2-47) and (2-48), respectively. Dividing  $\sigma_{yy}$ , as given by Eq. (2-48), by that from Eq. (2-47) yields:

$$\frac{P/(\pi\sqrt{2ar})}{P/(\pi\sqrt{a^2 - x^2})} = \frac{P/(\pi\sqrt{2a}\sqrt{a-x})}{P/(\pi\sqrt{a+x}\sqrt{a-x})} = \frac{\sqrt{a+x}}{\sqrt{2a}} = \epsilon \quad (2-55)$$

This ratio equals 1 when the contact mechanics and the asymptotic fracture mechanics solutions match exactly. The distance over which they asymptotically match for various levels of accuracy,  $x_{\text{asym}}$ , can be quantitatively assessed by letting the ratio in Eq. (2-55) equal the parameter  $\epsilon$ . From Eq. (2-55),

$$x_{asym} = |2\epsilon^2 - 1|a \quad (2-56)$$

In other words, when the contact mechanics and the asymptotically matched fracture mechanics solutions are at least 95% of each other, i.e. when  $\epsilon = 0.95$ , Eq. (2-56) shows that  $x_{asym}=0.8a$ . This implies that the two solutions match to an accuracy of better than 95% over 20% of the contact radius measured from the rim of the contact.

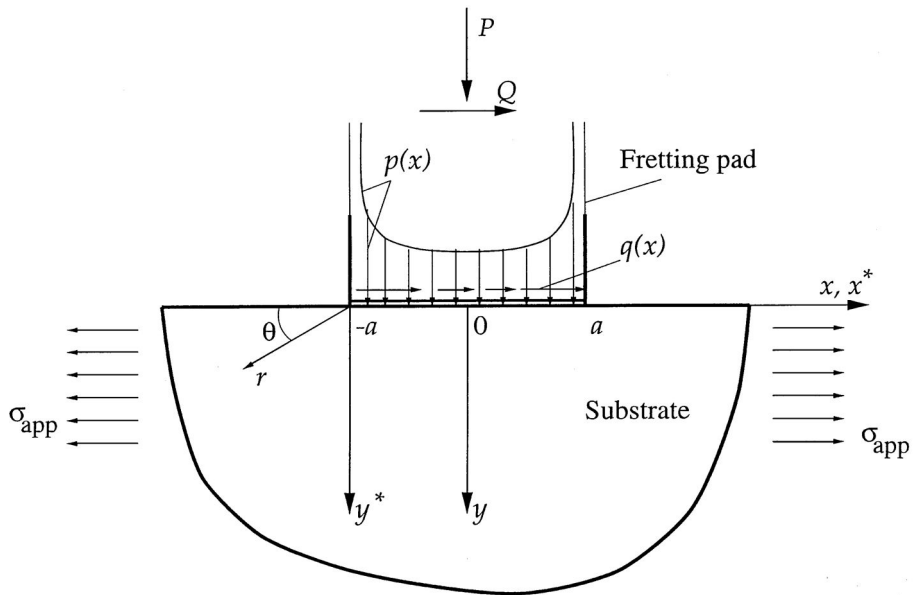


**Figure. 2.23** A schematic representation of the contact between a two-dimensional rectangular punch and a substrate

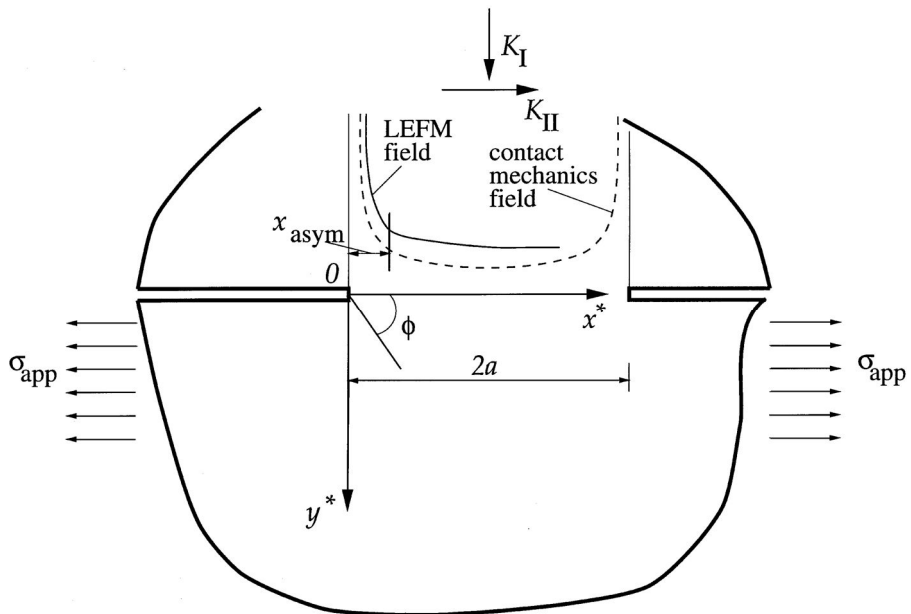


**Figure 2.24** Crack analogue of Figure 2.23 showing the double-edge cracked plate specimen that is subjected to mode I and mode II stress intensity factors,

$K_I$  and  $K_{II}$ .

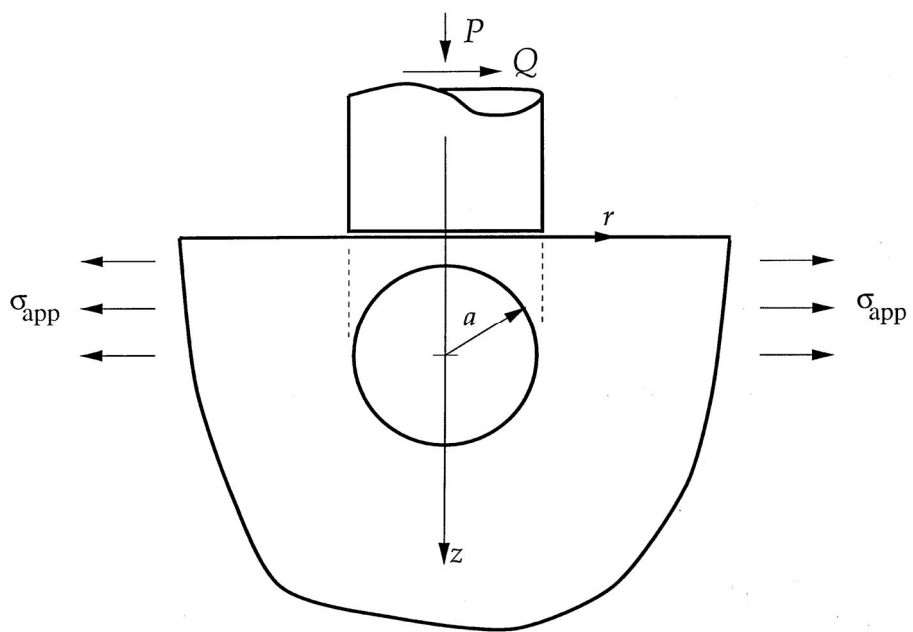


**Figure 2.25** A schematic representation of the contact between the end of a right-circular cylindrical punch and a substrate.

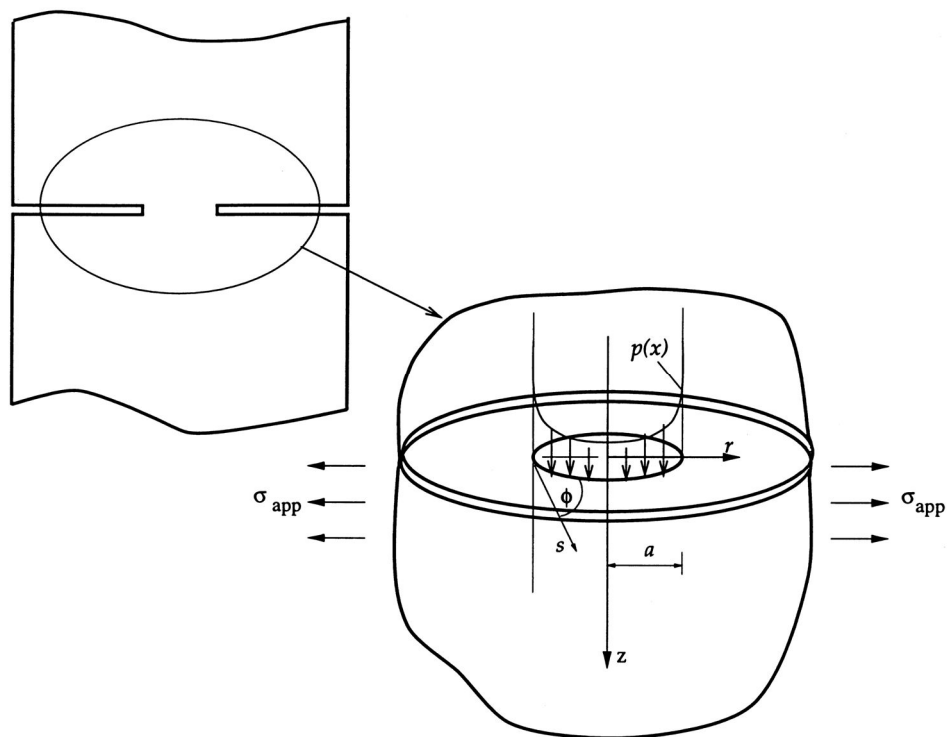


**Figure 2.26** Crack analogue of Figure 2.25 showing the circumferentially cracked cylindrical rod specimen, and the associated nomenclature

# **Chapter 3**

---

---

## **THEORETICAL MODELING**

### **Contents**

3.1. Introduction .....	100
3.1.1. Origin of modeling	
3.1.2. Key issues	
3.2. Ductile Fracture Model .....	113
3.2.1. Crack initiation determination	
3.2.2. Indenter size adjustment	
3.3. Brittle Fracture Model .....	122
3.3.1. Crack initiation determination	
3.3.2. Indenter size adjustment	

## **3.1. Introduction**

### **3.1.1. Origin of modeling**

Previous indentation fracture toughness models are based on the primary assumption that ahead of a crack tip and beneath a spherical indenter, the stress state has similar constraint effect to that shown in Figure 3.1, that is, a plastic deformed region is constrained by a surrounding elastic deformed region. This assumption, however, is a somewhat qualitative approach if we consider actual geometries of fracture toughness specimen and the spherical indenter in Figure 3.2. In the 2D explanation in Figure 3.1, the assumption seems to be right. But the actual crack geometry in common fracture toughness specimens such as C(T) and SEN(B) specimen has planar symmetry. On the other hand, the actual geometry in common indenter such as Vickers, Berkovich, flat punch, and also spherical indenter is axisymmetric. Therefore, the actual stress state at the crack tip and beneath the spherical indenter also has a planar symmetrical stress state and an axisymmetrical stress state, respectively.

In addition, as shown in Figure 3.3, there is a singularity point in the elastic stress field at the crack tip: infinite stress occurs at the crack tip point [120]. But there is no singularity point in the elastic stress field beneath the

spherical indenter [117]. As shown in Figure 3.4, although the maximum stress occurs at the center of contact area between the indenter and the material, it is not infinite and the decreasing trend of stress distribution with distance from the indenter center to its edge is different. On the other hand, for a flat punch indenter, the elastic stress field beneath the indenter has singularity points at the edge of the indenter and the decreasing trend of stress distribution with distance from edge to center of the indenter is similar.

Therefore, as mentioned in Chapter 2, the stress intensity factor,  $K$ , produced by the elastic stress field of a flat punch indenter is identical to that of circumferentially cracked round bar specimen if the mechanical behavior is isotropic, that is, the tensile and compressive behaviors of the material are identical [127]. From this, it is possible to model crack tip stress fields using indentation stress fields. The infinite stress at the crack tip or at the edge of flat punch indenter exists only in the linear elastic situation; in reality, the infinite stress induces local yielding and plastic deformation occurs immediately. The process and behavior (the plastic deformation) are also similar in two situations because of the similarity of the elastic stress fields. Therefore, extending the approach by applying a stress intensity factor concept of LEFM to the indentation situation, we see that the J-integral concept of EPFM also can be applied to flat punch indentation. Finally, we can simulate a virtual J test from flat punch indentation and determine the

fracture toughness parameter like  $J_{IC}$ .

In summary, since the contact mechanics of flat punch indentation and fracture mechanics of circumferentially cracked round bar specimen are almost identical, we can treat flat punch indentation as a virtual fracture toughness test with CRB geometry and then, from the indentation load-depth curve, we can calculate virtual fracture toughness parameters such as  $K$  or  $J$  and estimate virtual fracture toughness by considering crack initiation determination and indentation size adjustment, as described in the next section.

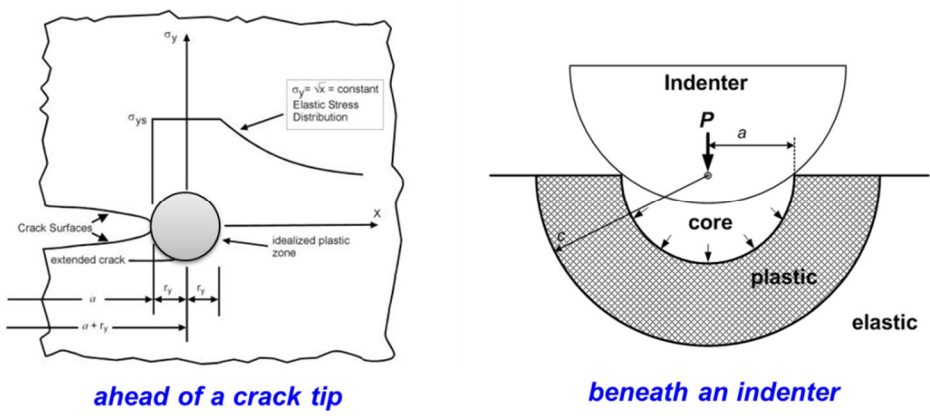


**Figure 3.1** Similar stress state ahead of a crack tip and beneath an indenter

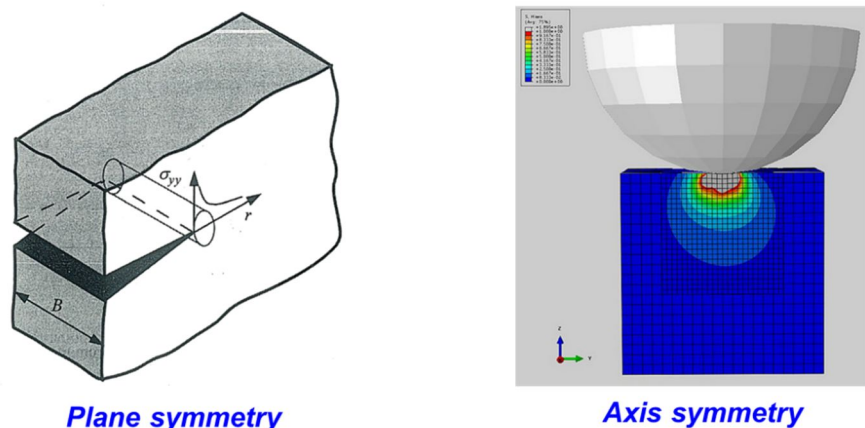


**Figure 3.2** Dissimilar symmetry of stress state ahead of a crack tip and beneath an indenter

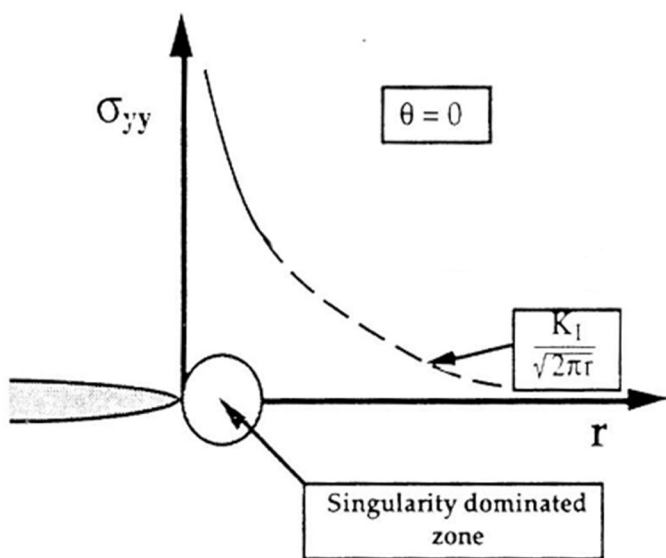


**Figure 3.3** Elastic stress field ahead of a crack tip

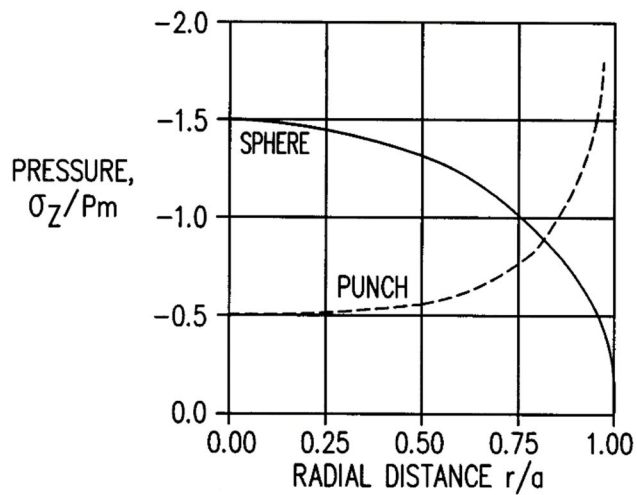


**Figure 3.4** Elastic stress fields beneath spherical indenter and flat punch indenter

### **3.1.2. Key issues**

Two key issues arise in estimating fracture toughness of metallic materials using flat punch indentation. The first and more fundamental issue is how to determine a virtual crack initiation point in indentation load-depth curve since there is no crack initiation in indentation on metallic materials. The other issue is how to apply the specimen size effect of fracture toughness testing to the indentation situation so that indentation fracture toughness can be correlated with standard conditions. Before looking at the first fundamental issue, we resolve the second using an indenter size adjustment.

$K_{JC}$ , one of the fracture toughness parameters used in the transition region to evaluate the ductile-brittle transition temperature, varies with specimen thickness, even when the same materials are tested, because of the statistical nature of the brittle fracture mechanism [53]. This point was not considered in previous indentation fracture toughness models. So indentation fracture toughness results from spherical indentation were always the same for materials that show brittle fracture behavior in fracture toughness testing. To resolve this issue, in flat punch indentation, indenter size can be considered as key. When the geometry of flat punch indenter is matched with a circumferentially cracked round bar specimen, the indenter radius corresponds to the remaining ligament radius of a circumferentially cracked

round bar specimen. Since the ligament size is a representative crack length parameter in deeply cracked fracture toughness specimen, it is related to the specimen size requirement in standard conditions; hence, using an indenter size adjustment, we can consider the specimen size effect of fracture toughness in brittle fracture mode.

As the radius of flat punch indenter increases, the load at the same indentation depth increases also. So different load-depth curves are measured for different flat punch indenter sizes, as shown in Figure 3.5. However, when load and indentation depth are divided by contact area and indenter radius, respectively, normalized curves are obtained that are identical for different indenter sizes, as shown in Figure 3.6. This is derived from the geometrical self-similarity of flat punch indentation: the normalized curve can be treated as a master curve for the material, which means response to indentation. This stress-like mean pressure and strain-like  $h/a$  curve are used in crack initiation determination and evaluation of tensile properties.

Meanwhile, this master curve can also be used in the above-mentioned indenter size adjustment and efficient testing procedure, since the curve can be converted to a load-depth curve of any size of flat punch indenter by calculating a new load and new depth from the master curve and multiplying by any indenter size, as shown in Figure 3.7. Thus, without manufacturing the specific size of flat punch indenter required by indentation fracture

toughness models but by using a flat punch indenter of an appropriate size, the load-depth curve of required flat punch indenter can be converted and, from this, the specimen size requirement under standard conditions can be considered.

Now the remaining key issue is crack initiation determination. In fracture toughness testing, crack initiation behaviors determined by fracture mechanisms of materials affect whether the testing finishes in ductile fracture mode or brittle fracture mode,. Crack initiation mechanisms and traces in the load-displacement curve at crack initiation also differ. Above all, in flat punch indentation of metallic materials, whether the fracture mode is ductile fracture or brittle fracture, since there is no cracking, appropriate determination of virtual crack initiation point is ultimately required. To resolve this issue, we benchmarked previous research on fracture behaviors of circumferentially cracked round bar specimens and tried to set appropriate criteria for crack initiation determination. We also established two indentation fracture toughness models, a ductile fracture model and a brittle fracture model, because of the contrasting nature of their fracture behaviors.

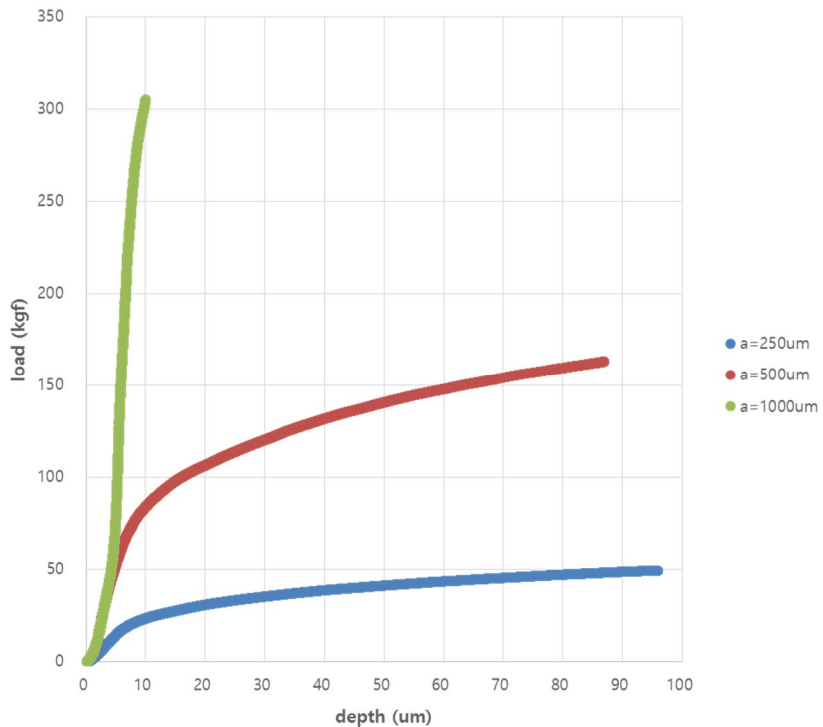


**Figure 3.5** Indentation load-depth curves using flat punch indenters of various indenter radii

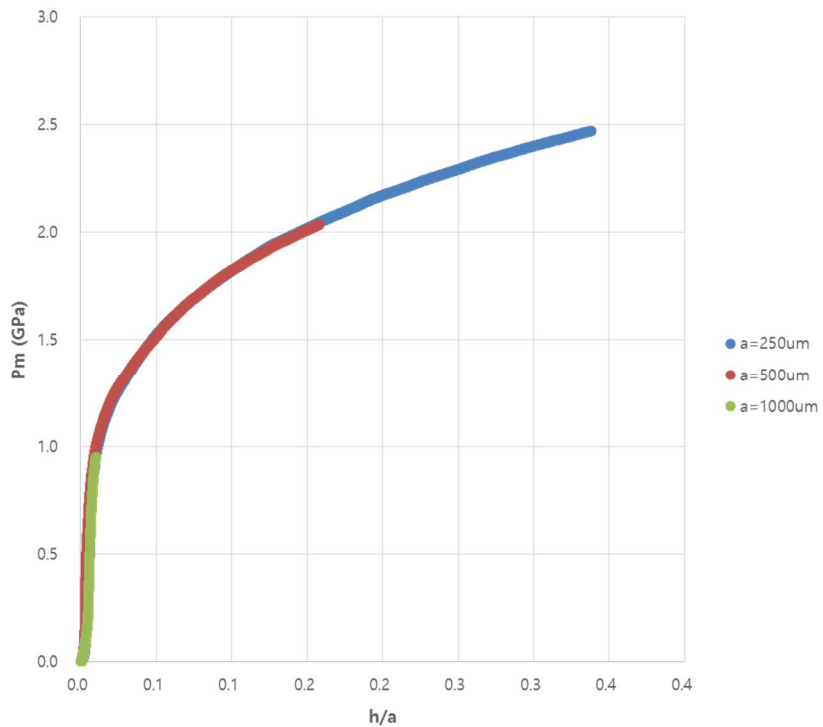


**Figure 3.6** Normalization of indentation load-depth curves using flat punch  
indenters of various indenter radii

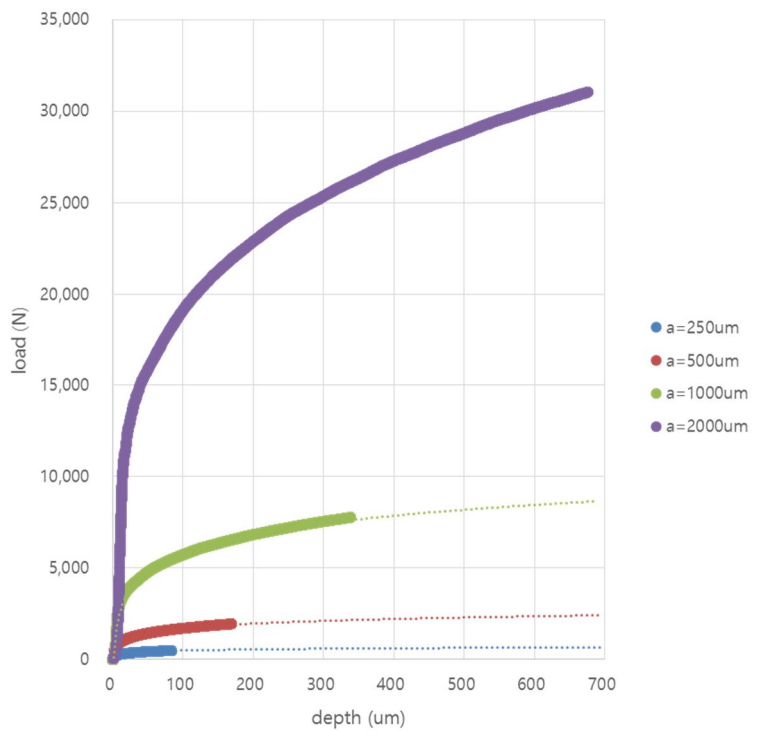


**Figure 3.7** Indentation load-depth curves converted from normalized curve

## **3.2. Ductile Fracture Model**

### **3.2.1. Crack initiation determination**

Previous research on fracture toughness testing with circumferentially cracked round bar specimens reports that crack initiation occurs at maximum load in the load-displacement curve as shown in Figure 3.8 [128, 129]. Since the load is a function of the reduction of the ligament size due to crack blunting, necking or crack growth, and since the increase of the average axial stress is due to higher constraint or strain hardening, the load drop can occur similarly to the necking point in tensile testing and the maximum load can be taken as the crack initiation point if we assume the load drop is due only to crack growth. Scibetta et al. [128] suggest that the maximum load be evaluated by the plastic limit load. In fact, as mentioned in Chapter 2, the limit load is defined as the load-bearing capacity in perfectly plastic behavior of materials and is a function of yield strength of materials and geometrical constant. However, in real materials, strain hardening occurs so that the load calculated from the theoretical limit load equation is not the end load point but a specific point, as shown in Figure 3.9. This point matches well with the crack initiation point in Scibetta's study.

The limit load equation of circumferentially cracked round bar geometry is

reported as [130]:

$$P_L = 2.845 \cdot \sigma_Y \cdot \pi a^2 \quad (3-1)$$

for the deeply cracked condition, where  $\sigma_Y$  is the yield strength or flow strength and  $a$  is ligament radius. The constant 2.845 is derived from the Tresca yield criterion, so 3.285 can be also used by applying Von Mises yield criterion. In flat punch indentation, because the indenter radius is very small compared to the specimen size, virtual crack length per specimen size is almost 1. Thus, under very deep cracked conditions, this equation can be applied.

In summary, for a ductile fracture model targeting materials having ductile fracture mode, the crack initiation point can be determined by a mechanical parameter, the limit load, which matches the maximum load in the load-displacement curve in fracture toughness testing with circumferentially crack round bar specimen.

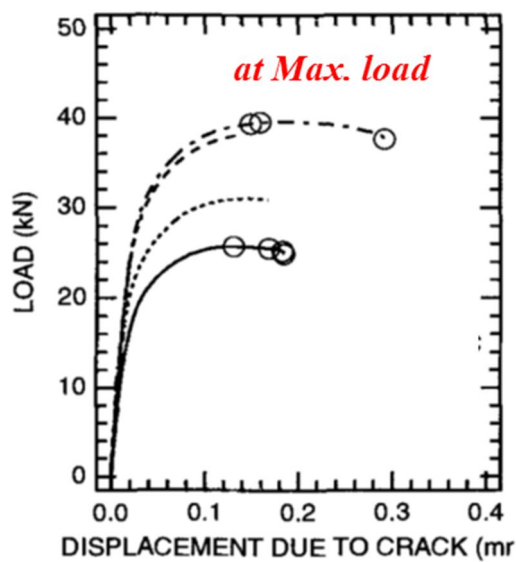


**Figure 3.8** Load displacement curves of circumferentially cracked round bar specimen with ductile fracture [129]

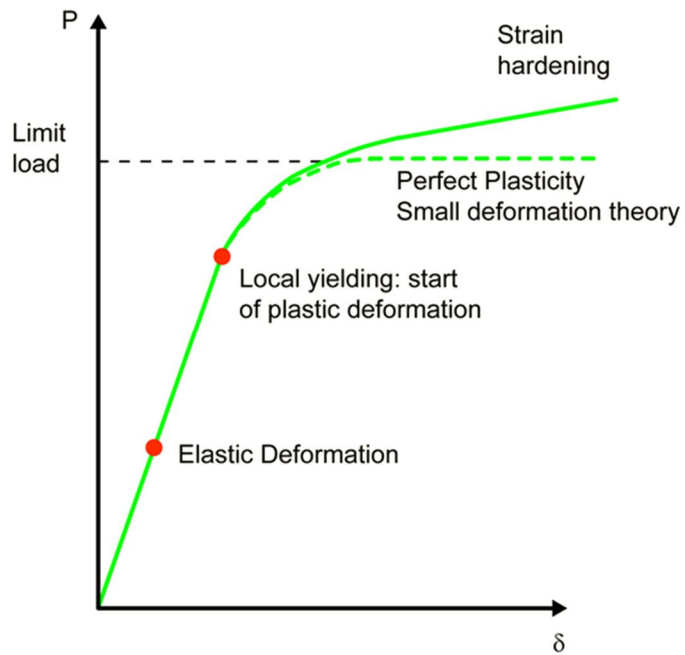


**Figure 3.9** Schematic description of limit load concept

### **3.2.2. Indenter size adjustment**

Although the crack initiation point is determined, virtual fracture toughness calculated from this crack initiation point varies with indenter radius. In order to adjust to an appropriate indenter size and also standard conditions, we use an idea from the fracture toughness testing standard. In fracture toughness testing standards such as ASTM [52] and ESIS [131], the fracture toughness parameter for ductile fracture is  $J_{IC}$  and the J-R curve method is generally used to evaluate  $J_{IC}$  because crack initiation is not clear in the load-displacement curve for a standard specimen geometry. In the J-R curve method,  $J_{IC}$  is determined by the intersection between blunting line and power-law-type  $J$  versus the crack extension curve, as shown in Figure 3.10. At this moment, the blunting line is shifted by 0.2 mm and this 0.2 mm offset means that a crack extension of 0.2 mm, including crack blunting, is empirically negligible for stable crack extension. In this sense, the standard also suggests another fracture toughness determination method similar to  $J_{0.2}$ , that is, an estimate of  $J_{IC}$  determined by the  $J$ -integral at 0.2 mm crack extension, as shown in Figure 3.11. Based on this, we attempted to replace 0.2 mm crack extension with an indentation parameter.

As shown in Figure 3.12, using the geometrical similarity between a circumferentially cracked round bar and flat punch indentation, the

indentation depth corresponds to half of the crack tip opening displacement (CTOD), and half of the CTOD corresponds to crack blunting. Thus the indentation depth corresponds to degree of crack blunting, that is, (roughly) to the crack extension. From this, the 0.2 mm crack extension including crack blunting is matched with the 0.2 mm indentation depth.

If only 0.2 mm indentation depth is used for fracture toughness determination, the indenter size effect also occurs. Therefore, 0.2 mm indentation depth is applied for indenter size adjustment with the crack initiation point determined by the limit load. If we convert indenter size to the appropriate indenter size for which the crack initiation point is determined by the limit load and make an indenter size adjustment by 0.2 mm indentation depth at the same load depth point, this is the best condition for estimating fracture toughness in the ductile fracture model. This condition means that when virtual crack is extended 0.2 mm, that is, indentation depth is 0.2 mm, the load reaches limit load point, that is, a virtual crack initiates.

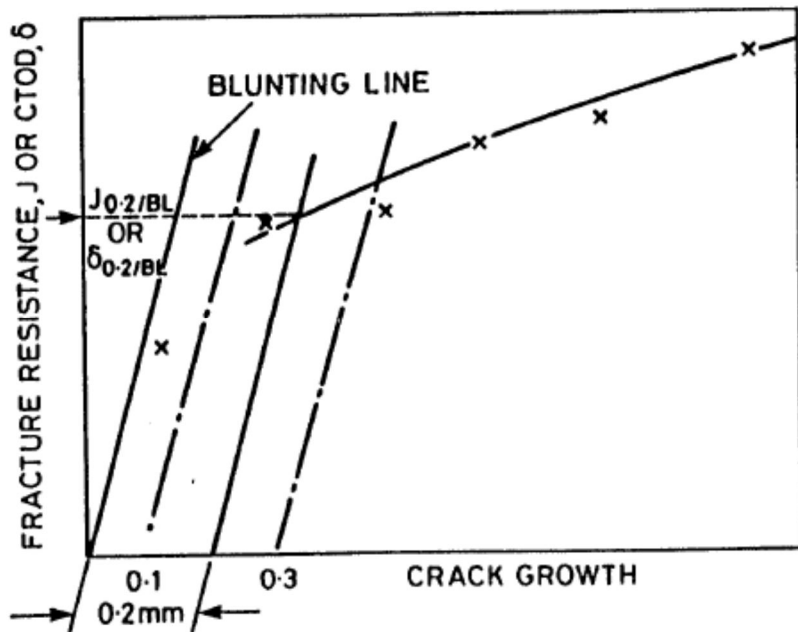


**Figure 3.10** General  $J_{\text{IC}}$  determination method in  $J$ - $R$  curve [131]

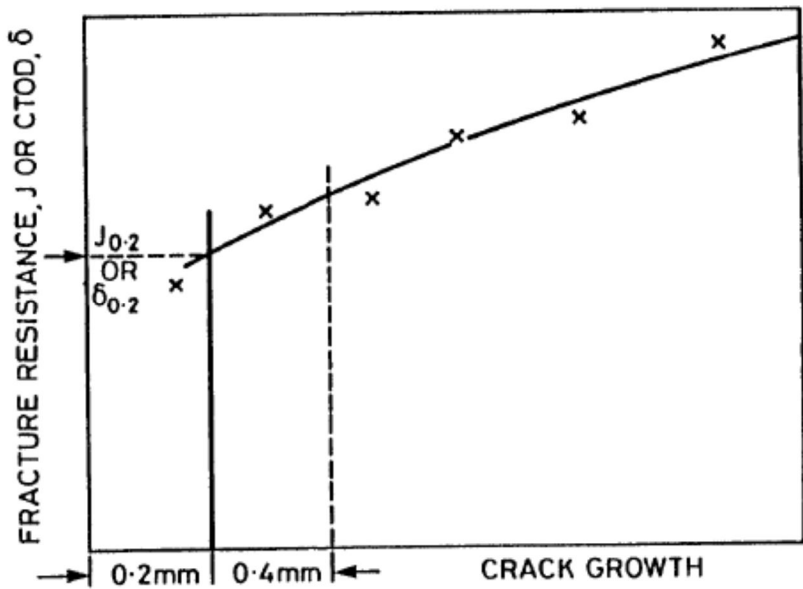


**Figure 3.11**  $J_{0.2}$  determination method in  $J$ - $R$  curve [131]

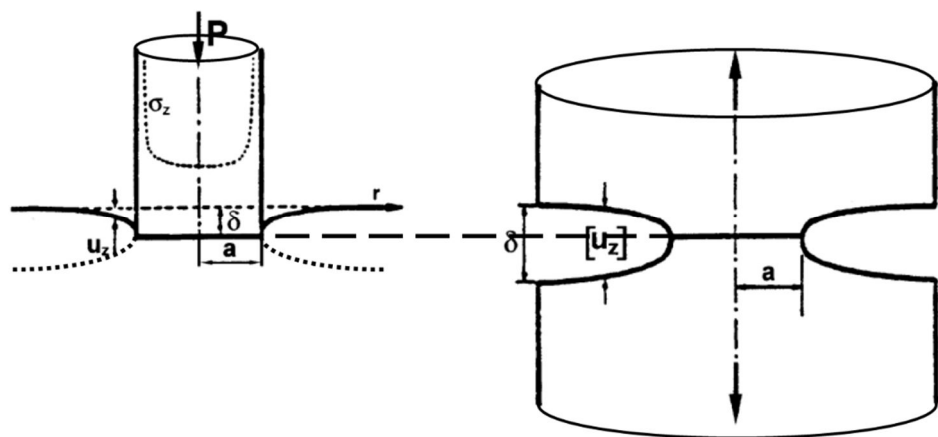


**Figure 3.12** Geometrical similarity between flat punch indenter and circumferentially cracked round bar specimen

### **3.3. Brittle Fracture Model**

#### **3.3.1. Crack initiation determination**

In contrast with ductile fracture mode, which shows stable crack extension, in brittle fracture mode crack initiation and fracture occur at the same time. Thus, the crack initiation point is clear in the load-displacement curve in fracture toughness testing and crack initiation is not a concern in brittle fracture mode. So we tried to determine the crack initiation point in the brittle fracture model intuitively, paying attention to the phenomenon that cracks generally initiate at the onset of nonlinear behavior in the load-displacement curve in fracture toughness testing, as shown in Figure 3.13. We finally chose 0.2% offset method, widely used in engineering to determine the onset of nonlinear behavior in the load-displacement curve or stress-strain curve [98]. Another method for crack initiation determination can be found in linear elastic fracture toughness standard [46]. In Figure 3.14, a 95% secant line method is also applicable for determining crack initiation point in the brittle fracture model. However, this method is originally for linear elastic behavior and its application is limited for flat punch indentation in general situations such as room-temperature testing of steel specimens, that is, when plastic deformation in flat punch indentation is considerable.

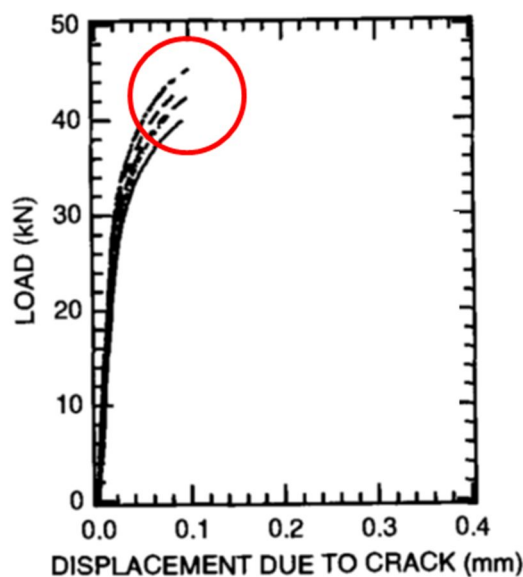


**Figure 3.13** Load displacement curves of circumferentially cracked round bar specimen with brittle fracture [129]

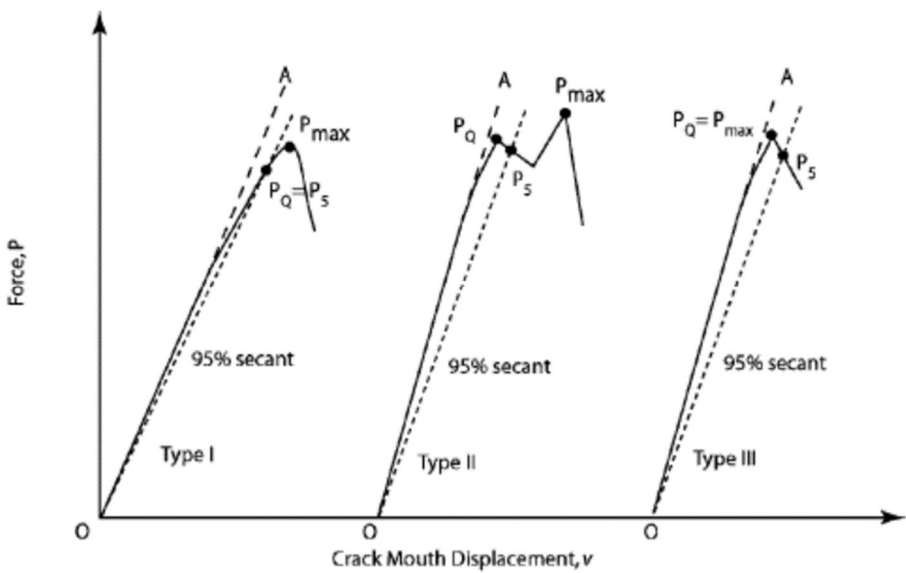


**Figure 3.14** 95% secant line method for  $K_{IC}$  determination [46]

### **3.3.2. Indenter size adjustment**

In brittle fracture mode, fracture toughness varies with specimen thickness and ASTM E1921 [53] recommends, instead of using the specimen size requirement for plane strain conditions, either using 1-inch-thick specimens or converting the fracture toughness value to that for 1-inch-thick fracture toughness specimen, as shown in Figure 3.15. From this point, we simply adjust indenter size corresponding to 1 inch thickness for a standard fracture toughness specimen. Since the thickness of a general fracture toughness specimen is the crack front length, in case of circumferentially cracked round bar specimen, the crack front length is the circumference of ligament, as shown in Figure 3.16, and the indenter size corresponding to 1 inch thickness is about 4 mm radius of flat punch indenter. Therefore, in the brittle fracture model, flat punch indentation is performed with any size of indenter and then the load-depth curve is converted to that for about 4 mm indenter radius. Finally, the crack initiation point is determined as the onset of nonlinear behavior.

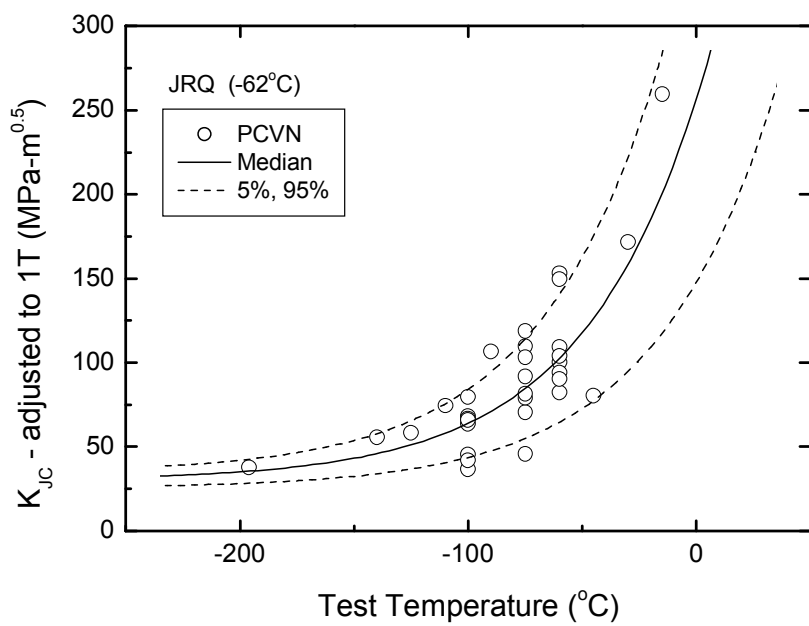


**Figure 3.15** Typical  $K_{\text{JC}}$  data adjusted to 1T (inch) thickness with temperature

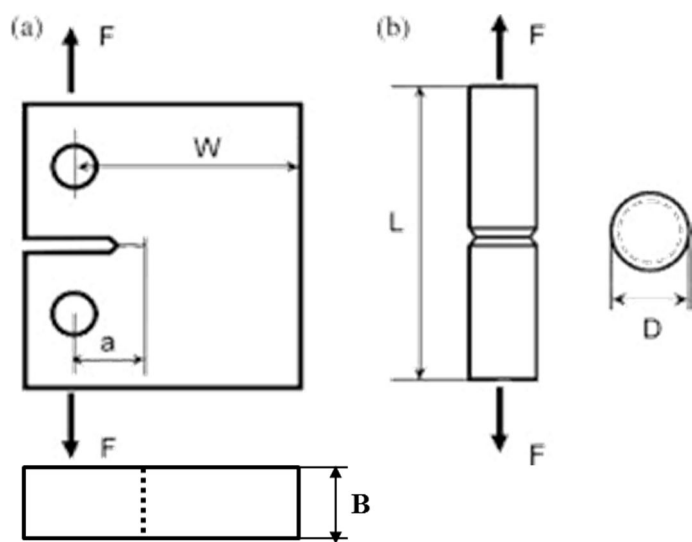


**Figure 3.16** Geometrical relationship between crack front length and specimen geometry

# **Chapter 4**

---

---

## **EXPERIMENTAL VERIFICATION**

### **Contents**

4.1. Materials and methods .....	129
4.2. Results and discussion .....	143
4.2.1. Tensile properties	
4.2.2. Fracture toughness	

## **4.1. Materials and methods**

To verify the proposed indentation fracture toughness models, various kinds of metallic materials for which fracture toughness is often required in industry are selected for flat punch indentation testing and conventional mechanical testing. The list and mechanical properties of selected materials are shown in Table 4.1.

Uniaxial tensile tests were carried out according to ASTM E8:09 [132] at room temperature. Test specimens used the 6 mm diameter smooth round test specimens shown in Figure 4.1, which is the small-size specimen proportional to the full-size one; gage length was 25 mm. The tensile tests were performed on an INSTRON 5582 material testing machine and cross-head speed was 1 mm/min. To get reliable average values for the tensile properties, at least five tensile tests have been carried out.

Flat punch indentation tests were performed with the AIS 2100 portable indentation system in Figure 4.2 (Frontics Inc., South Korea). This indentation equipment measured the real-time indentation load and depth through a 300 kgf load cell and a linear variable displacement transducer with resolution 0.002 kgf and 0.1  $\mu\text{m}$ , respectively. The indenter was a tungsten carbide cylindrical punch of 0.25  $\mu\text{m}$  radius. Under displacement-controlled conditions at 0.3 mm/min indentation speed, the maximum

indentation depth was 100 mm. At least three sets of indentation data were obtained from indentation tests for each material, and the average value was used in analyzing the fracture toughness. Indentation specimens were  $20 \times 20 \times 20$  mm and surfaces were polished with 1  $\mu\text{m}$   $\text{Al}_2\text{O}_3$  powder.

The fracture toughness tests were performed using two different methods according to ASTM E1820 [52]: the basic procedure and the resistance curve procedure. The basic method was used for material not showing significant stable crack growth prior to fracture instability. That is, the value of fracture toughness of brittle materials,  $J_C$ , was measured from the basic method. The resistance curve method was used to measure the fracture toughness,  $J_{IC}$ , near the onset of ductile crack extension, i.e. stable crack growth. A  $J$ - $R$  curve was obtained from the single specimen unloading compliance method, as illustrated in Figure 4.4. The crack length is computed at regular intervals during the test by partially unloading the specimen and measuring the compliance.

The configuration of the SENB (single-edge-notched bending) specimens is shown in Figure 4.5. All test specimens have orientation corresponding to loading in the longitudinal direction and crack propagation in the transverse direction from rolled plate. Also, an specimen orientation extracted from disk and hollow is L-R, i.e. loading in the longitudinal direction and crack propagation in the radial direction (Figure 4.6).

Straight fatigue pre-cracks were made on the specimens in front of the side-notch to make the ratio of total crack length to the specimen width ( $a/W$ ) valued between 0.5 and 0.7, since the unloading compliance technique is less sensitive for  $a/W < 0.5$ . The maximum load for the fatigue pre-cracking was calculated from:

$$P_m = \frac{0.5Bb_0^2\sigma_R}{S} \quad (4-1)$$

where  $\sigma_R$  is the flow stress and is typically the average of the yield strength and ultimate tensile strength. After pre-cracking, grooves are machined into the sides of each specimen to maintain a straight crack front during a  $J-R$  curve test; the total thickness reduction is 0.2B.

An INSTRON 8503 was used as for fracture toughness testing, as shown in Figure 4.7. The values of fracture toughness for each material were measured from at least three tests and the average values were used as the representative fracture toughness. Tested materials were heated to measure the length of the original crack, i.e. the length of the fatigue pre-crack, and final physical crack length, i.e. the extended length after testing at about 300°C for 30 min. The measuring instrument was a stereographic microscope and each crack length was measured at nine equally spaced points centered

about the specimen centerline, as shown in Figure 4.8. The provisional  $J_{IC}$  values are determined from the  $J$ - $R$  curves in Figure 4.9 and validity checks were also performed according to the requirement in ASTM E1820 [52].

**Table 4.1** Mechanical properties of tested materials

		Tensile properties				Fracture toughness					
		<b>E</b>	<b>YS</b>	<b>UTS</b>	n	<b>e<sub>f</sub></b>	<b>ε<sub>u</sub></b>	Thickness	J <sub>C</sub> / J <sub>IC</sub>	K <sub>JC</sub> (avg.)	Stdev.
		<i>GPa</i>	<i>MPa</i>	<i>MPa</i>				<i>mm</i>	<i>kJ/m<sup>2</sup></i>	<i>MPa<math>\sqrt{m}</math></i>	
Carbon Steels & Alloy Steels	S45C	207000	338.5	727.8	0.27	0.27	0.15	15	144.61	181.32	5.1
	SCM21	207000	288.8	579.3	0.22	0.30	0.14	15	339.98	281.37	12.0
	SS400	207000	259.4	497.0	0.24	0.38	0.18	20	423.05	310.21	0.1
	API X65	207000	466.9	650.9	0.17	0.35	0.15	14	372.91	291.18	8.0
	API X100	207000	598.6	918.1	0.14	0.25	0.09	19	548.24	352.80	19.1
	API X120	207000	745.9	1023.0	0.13	0.20	0.05	16	687.95	395.52	9.3
Tool Steels	SK3	207000	315.1	706.5	0.26	0.36	0.18	8	34.76	88.86	10.8
	SKS3	207000	434.9	755.5	0.22	0.31	0.16	8	60.60	118.17	5.8
	SKH51	207000	294.9	784.4	0.26	0.17	0.12	8	14.57	59.75	4.4
	SKD11	207000	342.8	807.7	0.26	0.12	0.10	8	40.52	98.37	6.8
	SUJ2	207000	404.3	821.7	0.24	0.33	0.16	8	54.38	113.87	13.0
	SKD61	207000	377.4	765.8	0.24	0.31	0.14	20	571.61	360.58	3.0
Stainless steels	SUS304	207000	285.7	1138.4	0.36	0.77	0.49	20	537.13	349.27	17.1
	SUS304L	207000	258.8	1164.7	0.40	0.65	0.43	20	666.29	389.21	11.0
	SUS347	207000	244.9	999.5	0.37	0.64	0.42	23	591.39	366.74	6.4
	SUS321	207000	252.4	1040.0	0.37	0.72	0.47	22	499.02	336.91	2.7

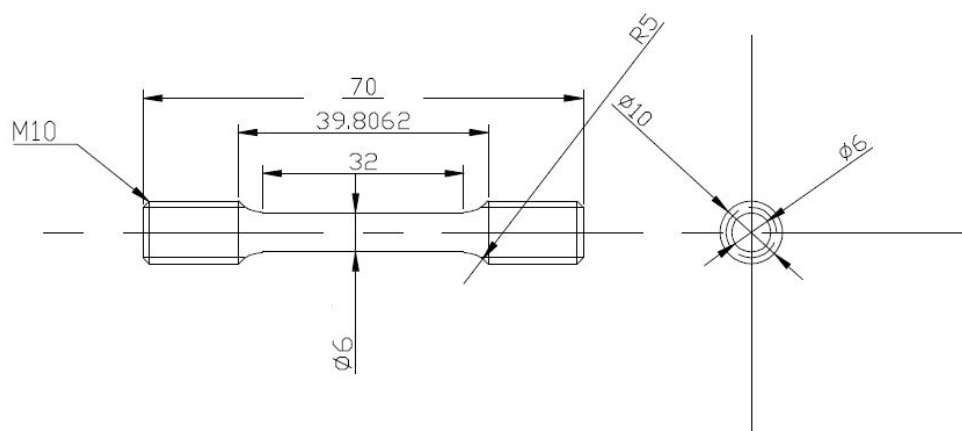


**Figure 4.1** Tensile specimen configuration according to specifications

ASTM E8:09



**Figure 4.2.** AIS 2100 system for indentation

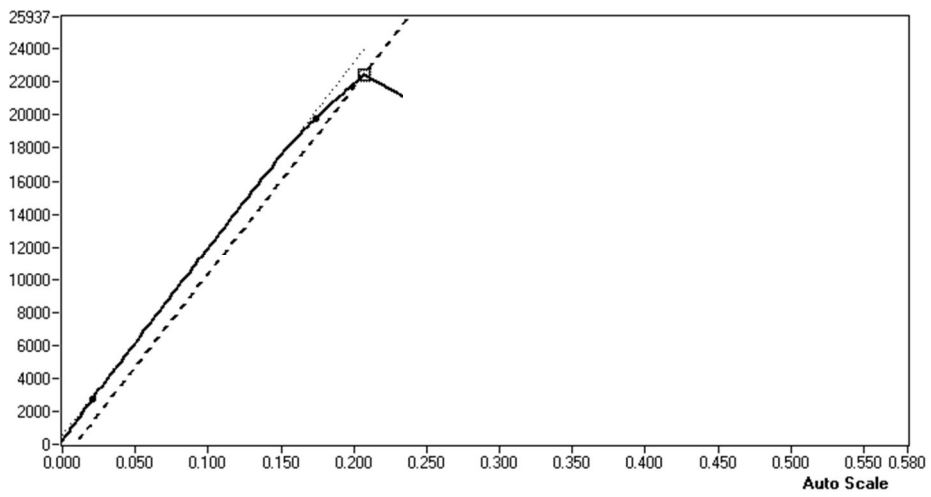


**Figure 4.3** Load and displacement curve measured from the basic method

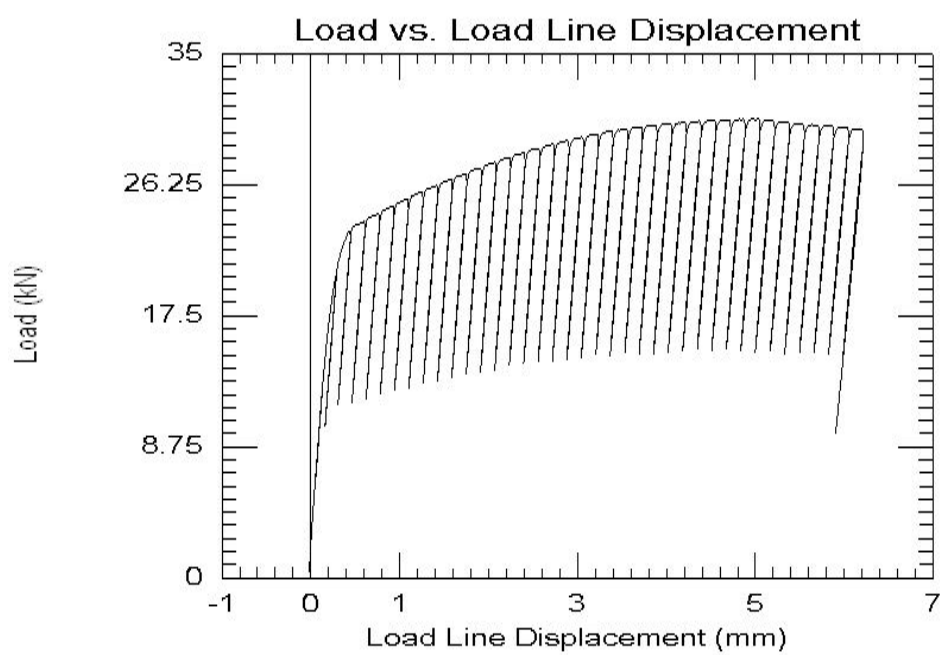


**Figure 4.4** An example of the unloading compliance method

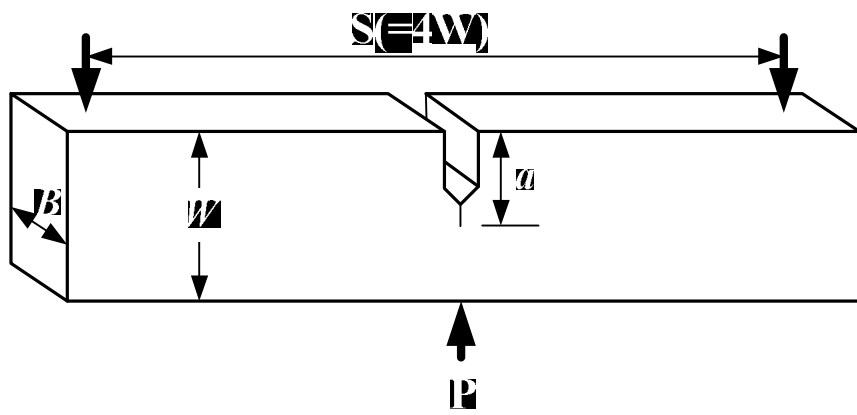
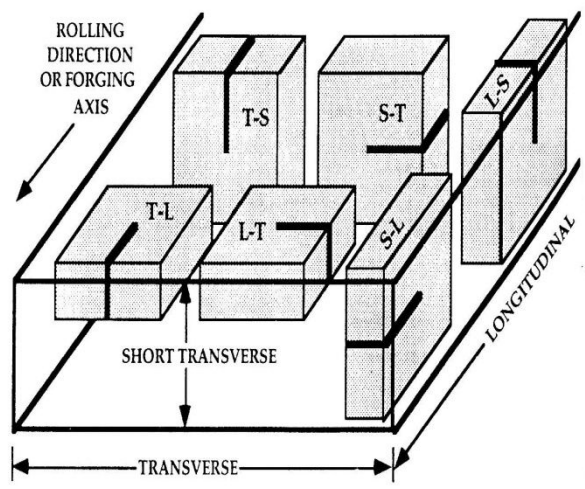
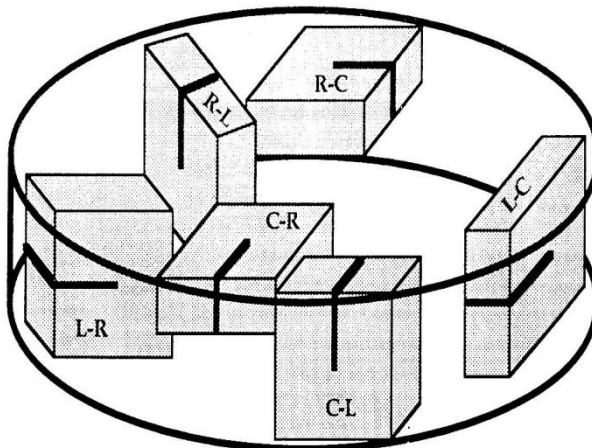


**Figure 4.5** Geometry of the SENB specimen used in fracture test according to specifications ASTM E1820:09



(a)

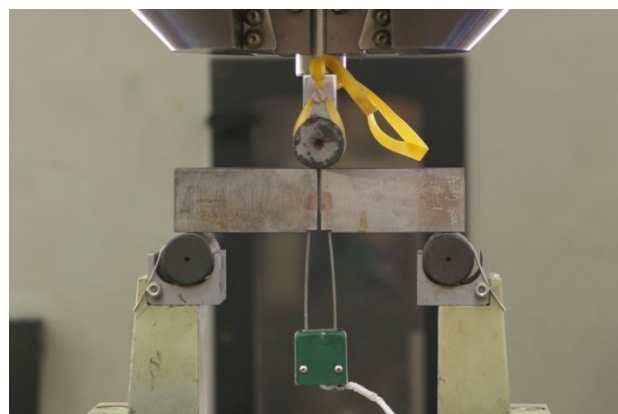


(b)

**Figure 4.6** ASTM notation for fracture specimens from (a) rolled plate and forgings and (b) disk and hollow cylinders



(a)



(b)

**Figure 4.7** The equipment and specimen for  $J$ -integral tests

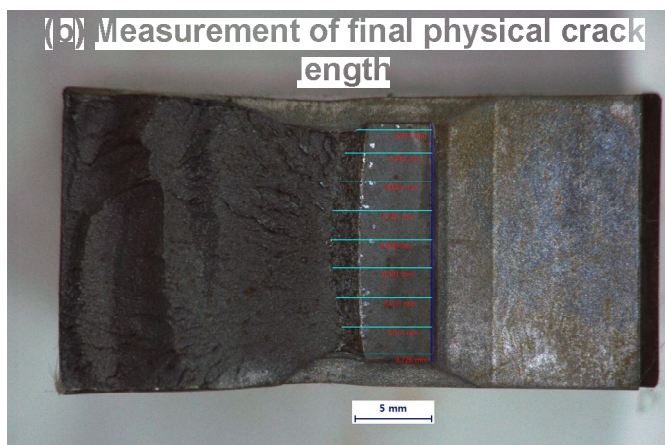
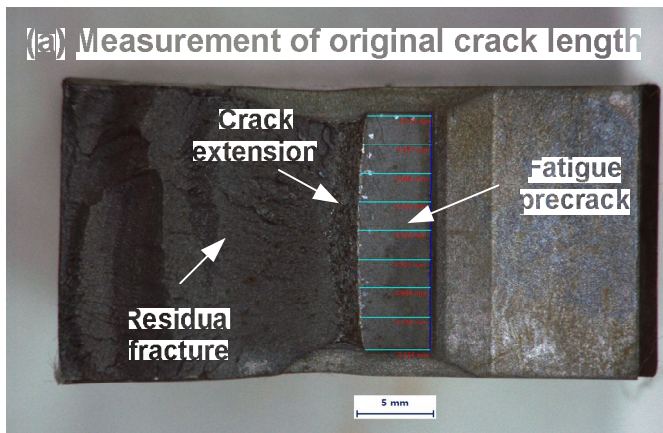


**Figure 4.8** Optical crack size measurement for SCM 21 and API X100: (a) original crack length and (b) final physical crack length

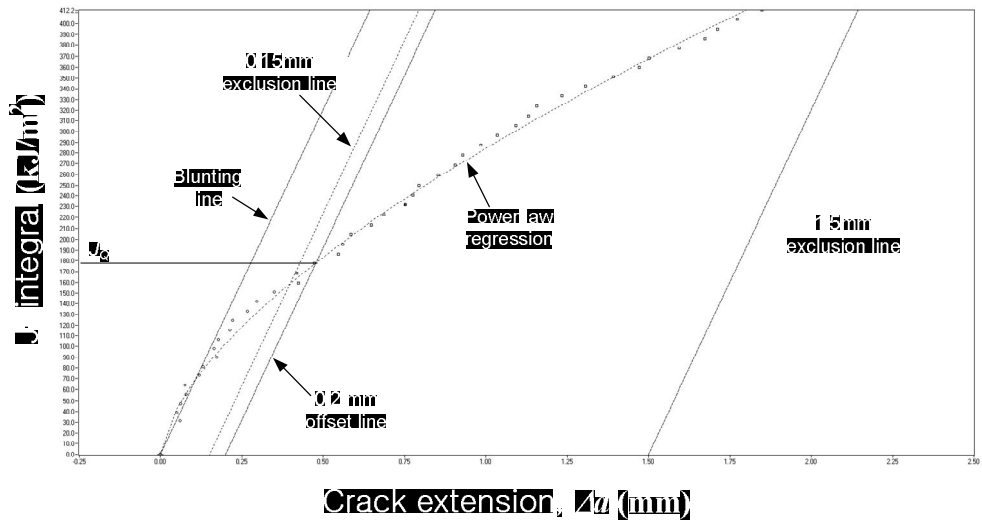


**Figure. 4.9**  $J$ - $R$  curve results

## **4.2. Results and Discussion**

### **4.2.1. Tensile properties**

Flat punch indentation was originally used for evaluating tensile properties of materials. Since the normalized curve of flat punch indentation is similar to the stress-strain curve in tensile or compressive testing, many researchers have investigated the relationship between these curves using the concept of representation [107-110]. A plastic constraint factor is used for the relationship between the mean pressure of flat punch indentation and the stress in tensile or compressive testing and is about 3 in many cases. Indentation depth per indenter radius is related to the strain in tensile or compressive testing and is the same as strain in many cases.

This study uses a simple approach to evaluate yield strength and strain-hardening exponent using flat punch indentation. The procedure is as follows:

- (1) The load-depth curve of flat punch indentation is normalized to a  $P_m - h/a$  curve.
- (2) The mean pressure is divided by plastic constraint factor of 3 for stress representation.
- (3)  $h/a$  is used as it is for strain representation.

- (4) Yield strength is determined by the 0.2% offset method in the representative stress and strain curve of flat punch indentation, which is an identical method of tensile testing as shown in Figure 4.10.
- (5) The strain-hardening exponent is determined by power law fitting in the fully plastic region of the indentation curve, again just as in tensile testing as shown in Figure 4.10.

The results are compared with uniaxial tensile test results in Figure 4.11. Yield strength and strain-hardening exponent evaluated from flat punch indentation match well (within 20% error range) with those evaluated from uniaxial tensile testing. The flat punch indentation results are also comparable to the spherical indentation results shown in Figure 4.12, so that flat punch indentation could be an attractive alternative to strength algorithms using spherical indentation because of its simple methodology. Moreover, evaluated yield strength values can be used for calculating limit loads for crack initiation determination in the ductile fracture model.

We conclude that flat punch indentation also can be used for evaluating tensile properties of materials. Future work will aim to improve the accuracy of the measured values.

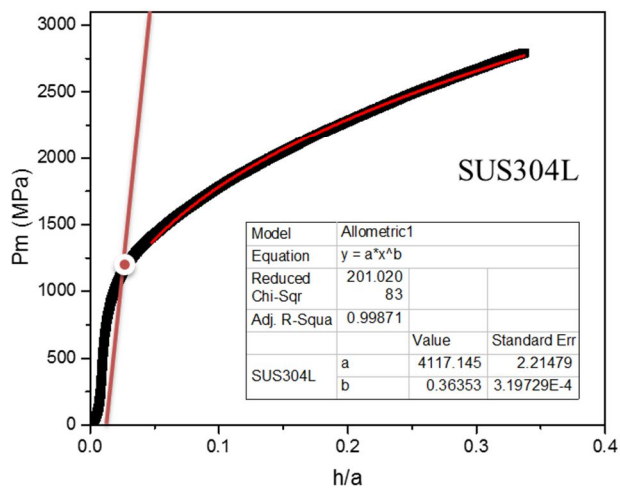
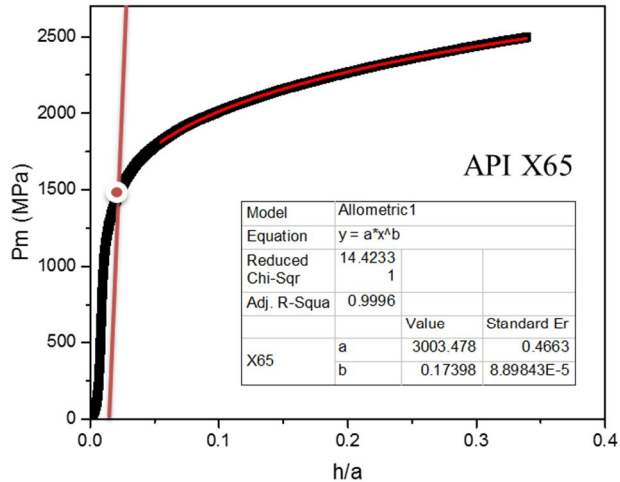


**Figure 4.10** Examples of data analysis for evaluating tensile properties using flat punch indentation

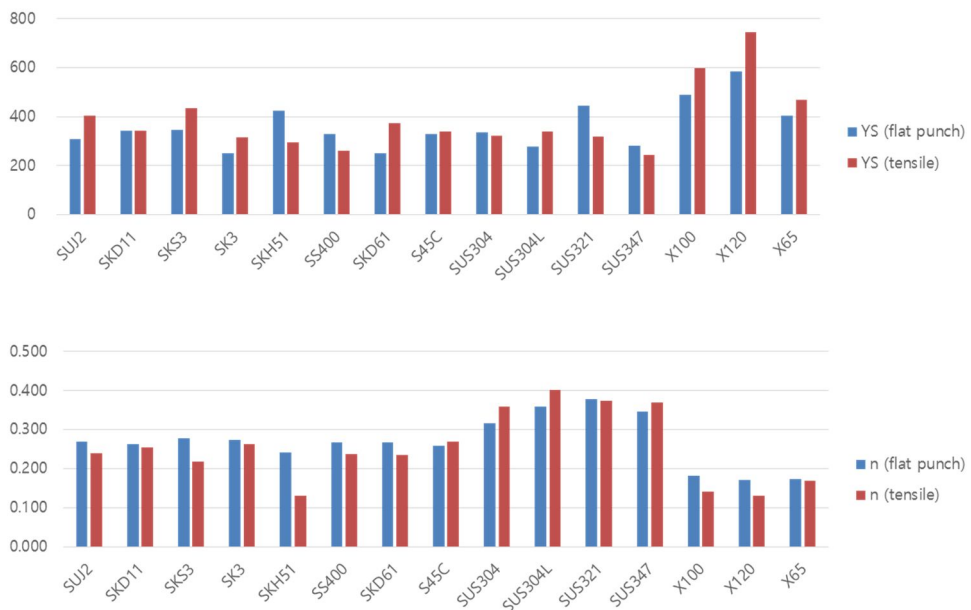


**Figure 4.11** Comparison between indentation tensile properties results and uniaxial tensile test results: (a) yield strength (b) strain-hardening exponent

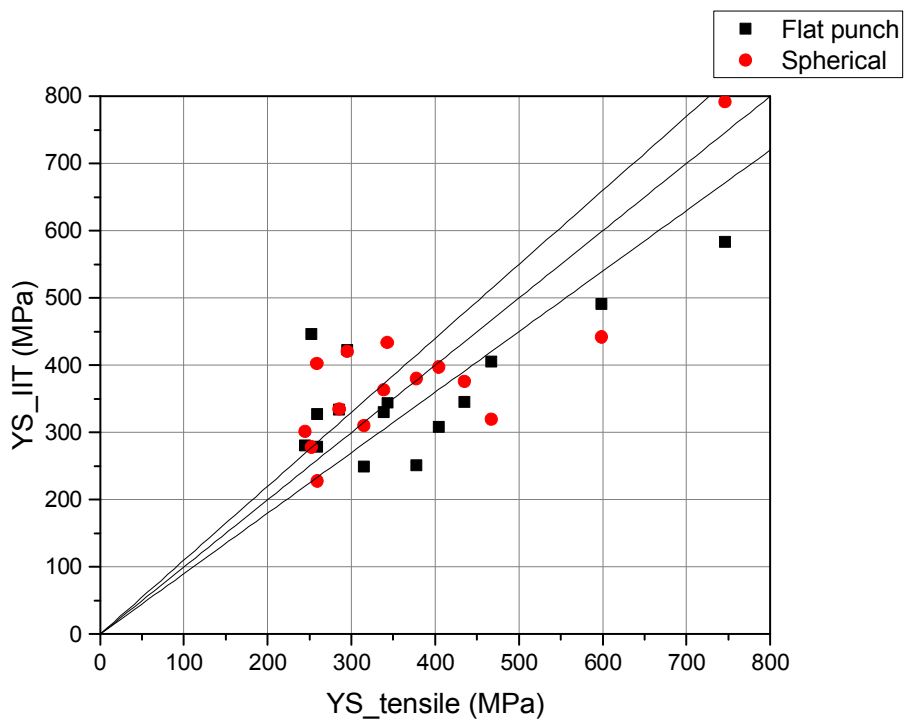


**Figure 4.12** Comparison of yield strength between flat punch indentation results and spherical indentation results

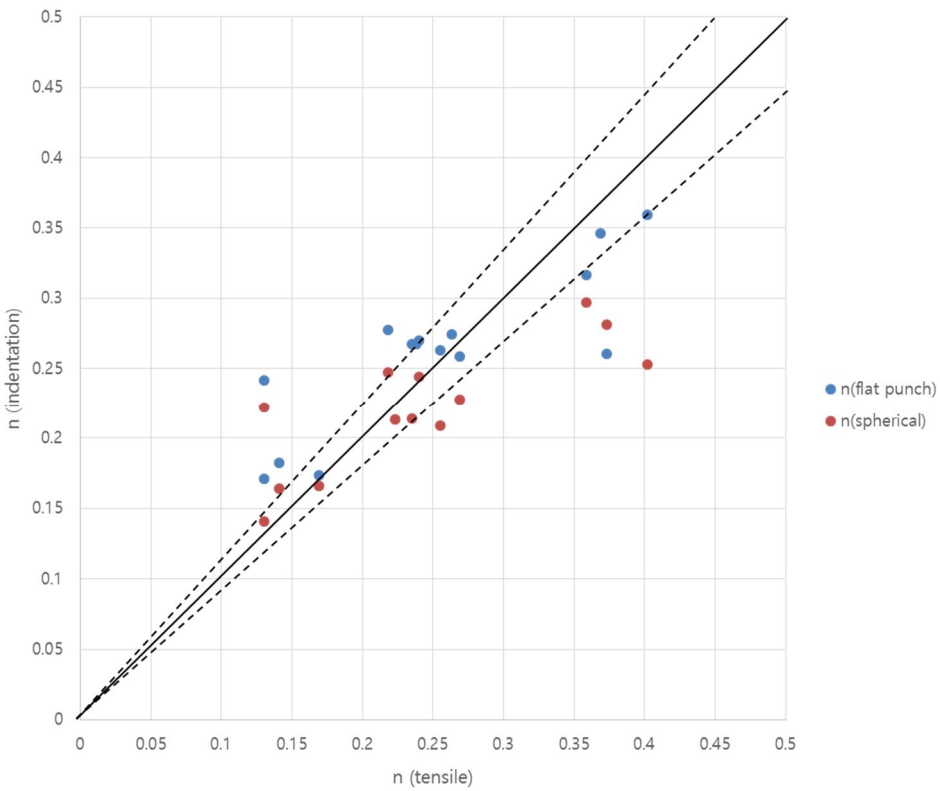


**Figure 4.13** Comparison of strain-hardening exponent between flat punch indentation results and spherical indentation results

#### 4.2.2. Fracture toughness

Determination of fracture toughness using the proposed indentation fracture toughness models is identical with standard fracture toughness testing, applying standard fracture mechanics, because we modeled flat punch indentation as virtual fracture toughness testing with a circumferentially cracked round bar specimen.  $J$  is calculated as follows [52]:

$$J_{IC} = J_e + J_p = \frac{(1 - \nu^2)K_I^2}{E} + \eta_{pl} \frac{A_{pl}}{\pi a^2} \quad (4-1)$$

where  $K_I$  is a stress intensity factor and is calculated using Eq. (2-54),  $E$  is elastic modulus,  $\nu$  is Poisson's ratio,  $A_{pl}$  is the area under the load-depth curve until the determined crack initiation point,  $a$  is indenter radius, and  $\eta_{pl}$  is a factor for specimen geometry and crack size equal to 0.775 for a circumferentially cracked round bar geometry.  $J_{IC}$  is converted to  $K_{JC}$  by

$$K_{JC} = \sqrt{\frac{J_{IC} \cdot E}{(1 - \nu^2)}} \quad (4-2)$$

The values of fracture toughness obtained from Eq. (4-2) are illustrated in

Figure 4.14 and compared with those from  $J$ -tests.

The values of fracture toughness for the ductile fracture model show about 20% deviation between the results in Figure 4.14(a). It turns out that with most materials the values of fracture toughness obtained from indentation are underestimated compared to those from fracture tests. If we take into account the universal deviation of fracture toughness in the upper shelf region, Figure 4.14(a) shows mostly good agreement. In the case of SS400 and SKD61, although the indentation result is largely underestimated, it is acceptable from a conservative point of view. And, as shown in Figure 4.15, the normalized curve and stress-strain curve from tensile test does not match well in these cases, perhaps because the indentation fracture toughness model has limitations and needs further study.

The results from the brittle fracture model in Figure 4.16(b) also show an approximately 20% deviation between the indentation and fracture tests overall, except for SKH51, which shows slightly larger error than others. This is expected because the fracture toughness value of SKH51 from  $J$  testing is somewhat low, contrary to expectations. Fracture toughness in the brittle region has large scatter by its statistical nature and differences in microstructure. The present study did not consider materials' microstructural aspects and manufacturing direction, which also affected fracture toughness results and probably produced the large error in the final results.

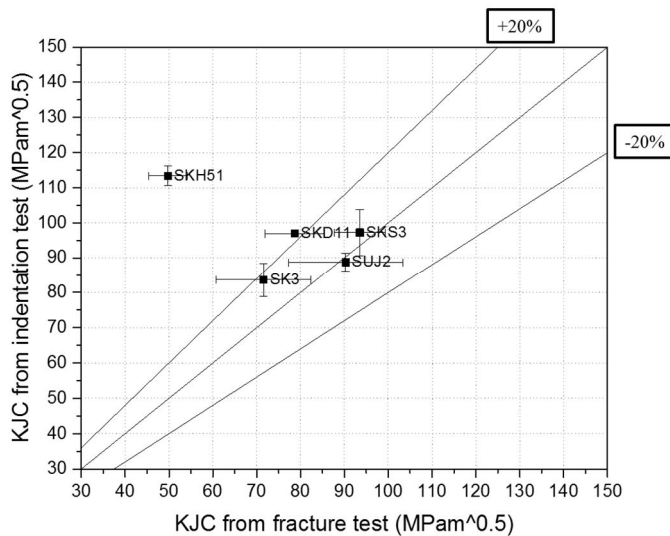
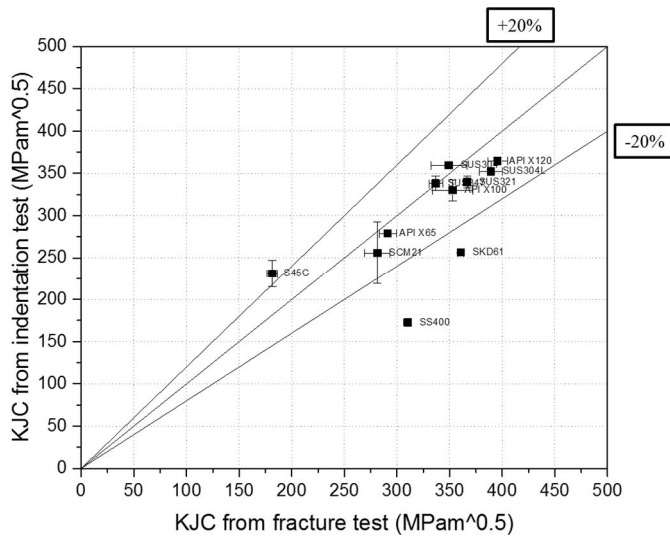


**Figure 4.14** Comparison of fracture toughness results between flat punch indentation tests and  $J$  tests: (a) ductile fracture model (b) brittle fracture model

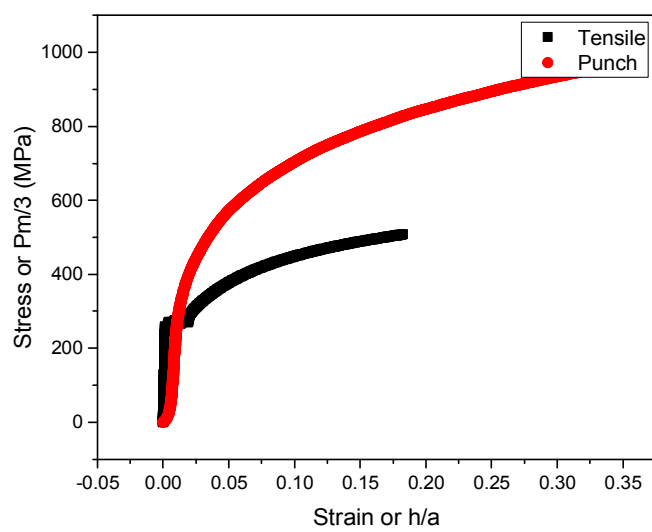


**Figure 4.15** Comparison between normalized flat punch indentation curve and stress-strain curve from uniaxial tensile test of SS400

## **Chapter 5**

---

---

---

## **CONCLUSIONS**

In this study, we developed models to estimate fracture toughness of metallic materials using flat punch indentation as a new approach for indentation fracture toughness models. Based on the analogy between contact mechanics of the flat punch indentation and fracture mechanics of the circumferentially cracked round bar geometry, we treated the flat punch indentation as a virtual fracture toughness testing and indentation behavior as a virtual crack tip behavior. Key issues are determination of the crack initiation point for non-cracking indentation behavior and adjustment of indenter size corresponding to the specimen size requirement of fracture toughness testing standard. We established two distinct indentation fracture toughness models according to fracture mechanisms,, a ductile fracture model and a brittle fracture model, and solved the issues for, both. In the ductile fracture model, the crack initiation point is determined by the limit load and indenter size is adjusted to a geometrical relationship between acceptable crack extension and corresponding indentation depth. In the brittle fracture model, the crack initiation point is determined by the onset of nonlinear behavior in the indentation curve and the indenter size is adjusted to the standard thickness of a fracture toughness specimen. We then calculated fracture toughness according to the standard fracture toughness calculation method.

To verify these models, experimental results were compared with standard  $J$

test results, confirming that these results match well (within 20% error range) for both models. In addition to fracture toughness, we evaluated tensile properties using flat punch indentation and yield strength, and the strain-hardening exponent can be evaluated by a simpler approach than the strength algorithm of spherical indentation. Further studies should improve indentation fracture toughness models and their application to evaluation of the ductile-brittle transition temperature and in-field testing.

## References

- [1] M.F. Doerner and W.D. Nix, *J. Mater. Res.* **1**, (1986).
- [2] W.C. Oliver and G.M. Pharr, *J. Mater. Res.* **7**, (1992).
- [3] W.C. Oliver, G.M. Pharr, *J. Mater. Res.* **19** (2004).
- [4] D. Tabor, *The Hardness of Metals*, Clarendon Press (1951).
- [5] D.M. Marsh, *Proc. of Res. Soc. of London, Ser. A* **279** (1964)
- [6] C.H. Mok, *Exp. Mech.*, **87** (1966).
- [7] R.A. George, S. Dinda, A.S. Kasper, *Metals Progress*, **30** (1976)
- [8] D. Kramer, H. Huang, M. Kriese, J. Robach, J. Nelson, A. Wright, D. Bahr, W.W. Gerberich, *Acta. Mater.*, **47** (1999).
- [9] J.H. Underwood, G.P. O'Hara, J.J. Zalinka, *Exp. Mech.*, **379** (1986).
- [10] H.A. Francis, *Trans. of ASME*, **9** 272 (1976).
- [11] F.M. Haggag and G.E. Lucas, *Mater. Tran. A* **14A**, 1607 (1983)
- [12] J.S. Field, M.V. Swain, *J. Mater. Res.*, **10**, 101 (1995).
- [13] A.C. Fischer-Cripps, B.R. Lawn, *Acta Mater.*, **44**, 519 (1996).
- [14] J. Alcala, A. Giannakopoulos, S. Suresh, *J. Mater. Res.*, **13**, 1390 (1998).
- [15] B. Taljat, T. Zacharia, F. Kosel, *Int. J. Solids Struct.*, **35**, 4411 (1998).
- [16] J.H. Ahn, D. Kwon, *J. Mater. Res.*, **16**, 3170 (2001).
- [17] J.Y. Kim, K.W. Lee, J.S. Lee, D. Kwon, *Surf. Coat. Technol.* **201** (2006).

- [18] T.Y. Tsui, W.C. Oliver, G.M. Pharr. *J. Mater. Res.* **11**, 752 (1996).
- [19] S. Suresh, A.E. Giannakopoulos. *Acta Mater.* **46**, 5775 (1998).
- [20] A. Bolshakov, G.M. Pharr. *J. Mater. Res.* **13**, 1049 (1998)
- [21] Y.H. Lee, D. Kwon. *J. Mater. Res.* **17**, 901 (2002).
- [22] Y.H. Lee, D. Kwon. *Acta Mater.* **52**, 1555 (2004).
- [23] S. Palmquist, *Jernkontorets Ann.* **141**, 300 (1957).
- [24] B.R. Lawn, J. Wilshaw, *J. Mater. Sci.* **10**, 1049 (1975).
- [25] B.R. Lawn, M.V. Swain, *J. Mater. Sci.* **10**, 113 (1975).
- [26] B.R. Lawn, E.R. Fuller, *J. Mater. Sci.* **10**, 2016 (1975).
- [27] B.R. Lawn, A.G. Evans, D.B. Marshall, *J. Am. Ceram. Soc.* **63** 574 (1980).
- [28] F.M. Haggag and R. K. Nanstad, ASTM PVP **170**, 41 (1989).
- [29] G.T. Hahn and A.R. Rosenfield, ASTM STP432, American Society for Testing and Materials, **5** (1968): Philadelphia.
- [30] T.S. Byun, J.W. Kim, J.H. Hong, J. Nucl. Mater. **252**, 187 (1998).
- [31] J.B. Ju, Ph. D. thesis at Seoul National University, (2003).
- [32] J.S. Lee, J.-i. Jang, B.W. Lee, Y. Choi, S.G. Lee, and D. Kwon, *Acta Mater.* **54**, 1101 (2006).
- [33] M. Janssen, J. Zuidema, and R.J.H. Wanhill, *Fracture Mechanics*, 2nd Edition (Spon Press, London and New York, 2004).
- [34] A.A. Griffith, *Phil. Trans. A* **221**, 163 (1920).

- [35] G.R. Irwin, *Sagamore Research Conference Proceedings* **2**, 289 (1956).
- [36] A.A. Wells and D. Post, *Proc. Soc. Exp.* **16**, 69 (1958).
- [37] J.R. Rice and G.F. Rosengren, *J. Mech. Phys. Solids* **16**, 1(1968).
- [38] H.M. Westergad, *J. App. Mech.* **6**, 49 (1939).
- [39] G.R. Irwin, *J. App. Mech.* **24**, 361 (1957).
- [40] J.M. Barsom and S.T. Rolfe, *Fracture and fatigue control in structures: application of fracture mechanics*, 3rd edition (ASTM, 1999).
- [41] W.S. Pellini, *Proc. Joint United States-Japan Symposium on Application of Pressure Component Codes*, Tokyo, Japan, March 13-15 (1973).
- [42] A.A. Wells, *Proc. Crack Prop. Sym.* **1**, 84 (1961).
- [43] T.L. Anderson, *Fracture Mechanics*, 3rd edition (CRC Press, 2005).
- [44] G.W. Wellman and S.T. Rolfe, *Fracture Mechanics: Sixteenth Sym.*, ASTM STP 868, 214 (1985).
- [45] A.D. Wilson, K. Donald, *Nonlinear Fracture Mechanics: Volume II: Elastic-Plastic Fracture*, ASTM STP 995, 144 (1989).
- [46] ASTM Test Method E-399: *Standard Test Method for Linear-Elastic Plane-Strain Fracture Toughness  $K_{IC}$  of Metallic Materials* (2009).
- [47] ASTM Test Method E-1290: *Standard Test Method for Crack-Tip Opening Displacement (CTOD) Fracture Toughness Measurement* (2008).
- [48] BS 5762, *Methods for Crack Opening Displacement (COD) Testing*,

The British Standards Institution (1979).

- [49] BS7448, *Fracture Mechanics Toughness Test*, The British Standards Institution (1979).
- [50] ASTM Test Method E-1737: *Standard Test Method for J-integral Characterization of Fracture Toughness* (discontinued 1998).
- [51] ASTM Test Method E-813: *Standard Test Method for  $J_{IC}$ , A Measure of Fracture Toughness* (1989).
- [52] ASTM Test Method E-1820: *Standard Test Method for Measurement of Fracture Toughness* (2009).
- [53] ASTM Test Method E-1921: *Standard Test Method for the Determination of Reference Temperature  $T_o$ , for Ferritic Steels in the Transition Range* (2009).
- [54] T.L. Anderson, D. Steinstra, R.H. Dodds, *Fracture Mechanics*, 24th Volume, ASTM STP 1207, 185 (1985).
- [55] M. I. Baskes, *Eng. Fract. Mech.*, **6**, 11 (1974).
- [56] K.H. Schwalbe, *Eng. Fract. Mech.*, **9**, 795 (1977).
- [57] C.Q. Chen and J.F. Knott, *Met. Sci.*, **15**, 357 (1981).
- [58] Z. Cvijovic, M. Vratnica, and K. Geric, *J. Microsc.*, **232**, 589 (2008).
- [59] J.M. Barsom and J.V. Pellegrino, *Eng. Fract. Mech.*, **5**, 209 (1973).
- [60] V.V. Teleshov, V.G. Kudryashov, *Strength of Materials*, **9**, 967 (1977).
- [61] N.V. Oleinik and Ngo Van Kuet, *Probl. Prochn.*, **1**, 72 (1976).

- [62] G. Said and S. Tasgetiren, *Eng. Fract. Mech.*, **67**, 345 (2000).
- [63] A.A. Baron, *Strength of Materials*, **25**, 556 (1993).
- [64] R. Roberts and C. Newton, *WRC Bull.* **299**, 1 (1984).
- [65] C.B. Ponton and R.D. Rawlings, *Br. Ceramic Trans. J.*, **88**, 83 (1989).
- [66] K.K. Sharma, P.N. Kotru, B.M. Wanklyn, *App. Surf. Sci.*, **81**, 2 (1994).
- [67] M.T. Laugier, *J. Mat. Sci. Letters*, **6**, 779 (1987).
- [68] V. Milekhine, M.I. Onsoien, J.K. Solberg, and T. Skaland, *Intermetallics*, **10**, 743 (2002).
- [69] N. Perez, *Fracture Mechanics* (Kluwer Academic, 2004).
- [70] H. Hertz., *J.Reine Angew. Math.*, **92**, 156 (1881).
- [71] V. Cerruti, *Memorie di Fisica Matematica*, (Accademia dei Lincei, Roma, 1882).
- [72] K.L. Johnson, *Contact Mechanics* (Cambridge University Press, Cambridge, 1985).
- [73] A.C. Fisher-Cripps, *Introduction to Contact Mechanics*, 2nd edition (Springer, 2007).
- [74] J. Boussinesq, *Application des Potentiels à l'Etude de l'Equilibre et du Mouvement de Solides* (Elastiques-Gautier-Villar, Paris, 1885).
- [75] A.E.H. Love, *A Treatise on the Mathematical Theory of Elasticity*, fourth ed. (Dover Publications, New York, 1944).
- [76] I. N. Sneddon, *Int. J. Eng. Sci.* **3** (1965).

- [77] S. Timoshenko, J.N. Godier, *Theory of Elasticity*, third ed., (McGraw Hill, New York, 1951).
- [78] R.F. Bishop, R. Hill, N.F. Mott, *Proc. Phys. Soc. London* **57** (1945).
- [79] K. Lange, *Handbook of Metal Forming* (McGraw Hill, New York, 1980).
- [80] W. Yu, J.P. Blanchard, *J. Mater. Res.* **11** (1996).
- [81] R.T. Shield, *Proc. R. Soc. A* **233** (1955).
- [82] G. Eason, R.T. Shield, *Zeitschrift für Angewandte Mathematik und Physik* **11** (1960).
- [83] ISO 14577-1: *Metallic Materials – Instrumented Indentation Test for Hardness and Materials Parameters – Part 1: Test Method* (2002).
- [84] ISO 14577-4: *Metallic Materials – Instrumented Indentation Test for Hardness and Materials Parameters – Part 4: Test Method for Metallic and Non-metallic Coatings* (2007).
- [85] ISO/TR 29381: *Measurement of Mechanical Properties by an Instrumented Indentation Test – Indentation Tensile Properties* (2008).
- [86] G.M. Pharr and A.J. Bolshakov, *J. Mater. Res.* **17**, 2660 (2002).
- [87] I.N. Sneddon, *Int. J. Engng. Sci.* **3**, 47 (1965).
- [88] A.E.H. Love., *Quart. J. Math.* **10**, 161 (1939).
- [89] A.E.H. Love., *Phil. Trans. A* **228**, 377 (1929).
- [90] J.W. Harding, I.N. Sneddon, *Proc. Camb. Phil. Soc.* **41**, 16 (1945).
- [91] I.N. Sneddon, *Fourier Transforms* (McGraw-Hill, New York, 1951).

- [92] Y. Liu, A.H.W. Ngan, *Scripta Mater.* **44**, 237 (2001).
- [93] J.Y. Kim, J.J. Lee, Y.H. Lee, J.I. Jang, D. Kwon, *J. Mater. Res.* **21** (2006).
- [94] G.M. Pharr, W.C. Oliver, F.R. Brotzen, *J. Mater. Res.* **7**, 613 (1992).
- [95] C.M. Cheng, Y.T. Cheng, *Appl. Phys. Lett.* **71**, 2623 (1997).
- [96] H. Gao, T.W. Wu, *J. Mater. Res.* **8**, 3229 (1993).
- [97] E.C. Jeon, M.K. Baik, S.H. Kim, B.W. Lee, D. Kwon, *Key Eng. Mater.* **2152**, 297 (2005).
- [98] G.E. Dieter, *Mechanical Metallurgy* (McGraw-Hill, New York, 1986).
- [99] K.W. Lee, K.H. Kim, J.-Y. Kim, and D. Kwon, *J. Phys. D: Appl. Phys.*, **D 41**, 074014 (2008).
- [100] G.R. Antis, P. Chantikul, B.R. Lawn, D.B. Marshall, *J. Am. Ceram. Soc.* **64**, 533 (1981).
- [101] J.R. Rice and D.M. Tracey, *J. Mech. Phys. Solids*, **17**, 201 (1969).
- [102] H.A. Francis, *J. Eng. Mater. Tech.*, **98**, 272(1976).
- [103] J. Lemaitre, *J. Eng. Mater. Tech.*, **107**, 83(1985).
- [104] G.E. Fougere, L. Riester, M. Ferber, J.R. Weertman, and R.W. Siegel, *Mater. Sci. Eng. A* **204**, 1 (1995).
- [105] L.M. Brown and J.D. Embury, *Proc. 3rd Int. Conf. Strength of Metals and Alloys* **1**, 164(1973).
- [106] S.H. Goods and L.M. Brown, *Acta Metall.*, **27**, 1 (1979).

- [107] B. Riccardi, R. Montanari, *Mater. Sci. Eng. A*, **381** (2004).
- [108] P. Gondi, R. Montanari, A. Sili, S. Foglietta, A. Donato, G. Filacchioni, *Fusion Technol.* (1996)
- [109] H.Y. Yu, M.A. Imam, B.B. Rath, *J. Mater. Sci.* **20** (1985)
- [110] B. Riccardi, R. Montanari, L.F. Moreschi, A. Sili, S. Storai, *Fusion Eng. Des.* **58–59** (2001).
- [111] M. Z. Sadowski, *Angew. Math. Mech.*, **8**, (1928).
- [112] A. I. Nadai, *Theory of Flow and Fracture of Solids, Vol. II*, (McGraw-Hill, NY, 1963).
- [113] H. Z. Hertz, *Reine Angew. Math.*, **92** (1882).
- [114] G. R. Irwin, *J. Appl. Mech.*, **24** (1957)
- [115] J. R. Rice, *J. Appl. Mech.*, **35** (1968).
- [116] G. M. L. Gladwell, *Contact Problems in the Classical Theory of Elasticity*, (Sijthoff and Noordhoff, Alphen aan den Rijn, 1980).
- [117] K. L. Johnson, *Contact Mechanics*, (Cambridge University Press, Cambridge, 1985).
- [118] D.A. Hills, D. Nowell, and A. Sackfield, *Mechanics of Elastic Contacts*, (Butterworth Heinemann, Oxford, 1993).
- [119] M.F. Kanninen, and C.H. Popelar, *Advanced Fracture Mechanics*, (Oxford Engineering Science Series, Oxford University Press, 1985).
- [120] T.L. Anderson, *Fracture Mechanics: Fundamentals and Applications*,

*2nd Ed.*, (CRC Press, Boca Raton, FL, 1995).

- [121] H.M. Westergaard, *J. Appl. Mech.*, **6** (1939).
- [122] I.N. Sneddon, *Proc. Cambridge Philos. Soc.*, **42** (1946).
- [123] M.L. Williams, *J. Appl. Mech.*, **24** (1957).
- [124] H. Tada, P.C. Paris, and G.R. Irwin, *Stress Analysis of Cracks Handbook*, (Del Research Corporation, Hellertown, 1973).
- [125] D.P.H. Rooke and D.J. Cartwright, *Compendium of Stress Intensity Factors*, (Her Majesty's Stationery Office, London, 1976).
- [126] Y. Murakami, *Stress Intensity Factors Handbook*, (Pergamon Press, New York, 1987).
- [127] A.E. Giannakopoulos, T.C. Lindley and S. Suresh, *Acta Metallurgica*, **66** (1998)
- [128] M. Scibetta, R. Chaouadi, and E. Van Walle, *International Journal of Fracture*, **104** (2000)
- [129] J.Giovanola, T.Kobayashi, *Engineering Fracture Mechanics*, **59** (1998).
- [130] A. Miller, *International Journal of Pressure Vessels and Piping*, **32** (1988).
- [131] ESIS P2-92: *ESIS Procedure for Determining the Fracture Behavior of Materials* (1992)
- [132] ASTM Test Method E8: *Standard Test Method for Tension Testing of Metallic Materials* (2009).

## 초 록

대형구조물의 예기치 못한 파손은 심각한 손실을 가져오기 때문에 파손을 방지하기 위해 다양한 기법의 구조건전성 평가가 이루어지고 있다. 사용 중인 구조물의 건전성을 평가하기 위해서는 구조물에 가해진 응력 정보, 구조물 내부에 존재하는 결함 정보, 그리고 구조물 소재의 물성 정보를 정확히 아는 것이 중요하다. 특히, 많은 경우에 있어서 구조물의 파손 원인은 열화나 취화와 같은 소재물성의 변화에서 유발되기 때문에 설계 당시의 소재물성보다는 실제 사용 중인 상태에서의 기계적 물성을 측정하여 이를 반영하는 것이 요구된다. 하지만 기존의 기계적 시험법들은 규격화된 시편을 제작하여 이를 파괴시킴으로써 소재의 기계적 물성을 측정하는 파괴적 시험법이기 때문에, 사용 중인 구조물의 기계적 물성을 실시간으로 평가하는 데에 적용할 수 없다는 단점이 있다.

이에 대한 대안으로 제안되고 있는 연속압입시험법은 뾰족한 압입자를 이용하여 평가대상물의 표면에 하중을 가하면서 실시간으로 하중과 압입깊이를 측정하고, 측정된 하중변위곡선의 해석을 통하여 소재의 다양한 기계적 특성을 평가하는 기법이다. 이 기법은 소재 표면에 작은 압흔 만을 남기기 때문에 비파괴적인 기계적 시험법으로서 기존의 시험법들과 달리 현장에서 직접 물성 측정이 가능한 장점이 있고, 국부적인 영역의 시험을 통한 국부물성 평가도 가능하기 때문에 박막이나 전자부품 등 마이크로/나노스케일의 기계적 시험법으로도 널리 사용되고 있다. 최근에는 역학적 모델링을 바탕으로 압입시험의 기본물성인 경도와 탄성계수뿐만 아니라,

인장물성, 잔류응력, 파괴인성을 평가하는 기술이 개발되고 있다.

그 중에서도 파괴인성은 구조건전성의 파괴역학적 해석을 위해 요구되는 고급물성이지만, 일반적인 구조해석에 쓰이는 강도와 달리 균열길이, 시편형상 등 다양한 변수의 영향을 받아 그 해석이 어렵기도 하거니와, 표준화된 파괴인성 시험법 역시 복잡한 절차와 파괴적 시험이라는 본질 때문에 적용이 어려운 단점이 있어, 압입시험을 이용해 파괴인성을 평가 또는 예측하고자 하는 많은 연구들이 진행되어왔다.

본 연구에서는 보다 이론적이고 실제적인 접근을 통하여 압입시험을 이용한 금속소재의 파괴인성 예측모델을 개발하고자 하였다. 압입자 하부의 응력상태와 균열첨단 앞에서의 응력상태를 매칭하고자 기존에 널리 사용되는 구형 압입자 대신 플랫펀치 형상의 압입자를 사용하고, 이를 통해 압입거동과 균열거동을 직접적으로 연계시킴으로써 단순한 에너지적 연관성을 넘어 가상의 파괴인성을 유도하는 방식으로 모델링을 수행하였다. 압입시험에서는 균열이 발생하지 않기 때문에, 파괴시험에서의 균열개시시점을 압입상황에서 결정하기 위해 이론적/공학적 관점에서 기준을 설정하였다. 그리고 기존의 연구들에서 고려되지 않았던 파괴인성의 시편크기조건을 압입상황에 적용하여 표준시험 조건에 부합될 수 있도록 고려하고자 하였다.

우선 소재의 일반적인 파괴거동에 따라 모델을 연성파괴모델과 취성파괴모델로 구분하였다. 연성파괴모델의 경우, 실제 파괴시험에서의 균열개시시점을 역학파라미터 중 하나인 한계하중(limit load)으로 예측하는 기존 연구 결과를 토대로, 압입시험에서의 한

계하중을 계산함으로써 균열개시시점을 예측하였다. 또한 플랫펀치 압입자와 원주형태의 균열시편의 기하학적 유사성으로부터 압입깊이를 가상의 균열진전량으로 보고 표준에서 제시하는 공학적 기준인 0.2mm 균열진전량에 대응되는 압입깊이를 설정함으로써 파괴인성의 시편크기조건과 대응되는 압입자 크기를 결정하였다. 취성파괴모델의 경우, 보다 공학적 접근을 토대로 하중변위곡선에서 초기 선형성이 끝나는 지점을 균열개시시점으로 보고 표준에서 제시된 95% 할선 기법을 이용해 균열개시시점을 결정하였다. 시편크기 조건에 대해서는, 연성파괴와 달리 취성파괴에서는 시편의 크기에 따라 파괴인성이 달라지고 이에 대한 확률론적 접근법에 의해 1T의 두께시편으로 환산하여 파괴인성을 평가하는 기준의 관례를 따라 1T의 두께에 해당하는 압입자 크기를 선정하여 실제 파괴인성 결과에 대응되도록 하였다.

각각의 모델을 통해 결정된 하중변위곡선으로부터 파괴역학의 어법을 그대로 적용하여 파괴인성 파라미터인 J를 계산하였다. 이를 K로 환산한 KJC 결과를 실제 표준시험법으로 구한 파괴인성 결과와 비교하였다. 모델의 검증을 위해 파괴인성평가가 주로 요구되는 구조용 강, 스테인리스 강, 파이프용 강 등을 선정하여 비교한 결과, 20% 오차범위 내에서 그 결과가 잘 일치함을 확인할 수 있었다.

또한 플랫펀치 압입시험은 압입거동이 완전소성영역로 넘어갈 경우, 인장/압축시험의 거동과 유사성을 보이기 때문에, 이를 기반으로 인장물성인 항복강도와 가공경화지수를 평가할 수 있다. 대표 응력-대표변형률 기법을 활용하여 하중변위곡선을 응력-변형률

곡선으로 변환하고 표준의 인장물성 측정법을 그대로 적용하여 항복강도와 가공경화지수를 평가한 결과, 이 역시 20% 오차범위 내에서 그 결과가 잘 일치함을 확인할 수 있었다.

본 연구에서는 플랫편치 압입시험을 이용하여 금속소재의 파괴특성인 파괴인성과 변형특성인 항복강도, 가공경화지수를 평가하는 모델을 개발하였다. 비파괴시험인 압입시험과 파괴시험인 파괴인성 시험의 차이를 극복하고 파괴인성을 예측하기 위해, 압입응력장과 균열응력장의 이론적 유사성과 더불어 균열개시시점의 공학적 접근법을 적용하여 파괴인성을 예측하고자 하였으며, 마찬가지로 소재의 항복강도와 가공경화지수를 기준의 압입시험연구와 비교하여 보다 직관적인 방법론으로써 평가하였다. 개발된 모델은 후속연구를 통해 온도 변화에 따른 파괴인성 변화 및 DBTT 평가 연구나 서두에 제안한 구조건전성 평가를 위한 현장물성 평가에 활용될 수 있을 것으로 기대된다.

**주요어:** 연속압입시험, 파괴인성, 인장물성, 플랫편치, 연성파괴, 취성파괴, 구조건전성

**학번:** 2008-20634

# LIST OF PUBLICATIONS

## I. International Journals

1. **Junyeong Kim**, Kug-Hwan Kim, Dongil Kwon: Evaluation of High-Temperature Tensile Properties of Ti-6Al-4V Using Instrumented Indentation Testing, *Metals and Materials International* 22 (2016) (in press)
2. Seung-Won Jeon, Kyung-Woo Lee, **Junyeong Kim**, Dongil Kwon: Estimation of Fracture Toughness of Metallic Materials Using Instrumented Indentation Testing, *Experimental Mechanics* (2016) (submitted)

## II. International Conference (\* indicates speaker)

1. **Junyeong Kim\***, Kyung-Woo Lee, Seung-Won Jeon, Dongil Kwon: Estimation of Fracture Toughness Using Instrumented Indentation Testing: Ductile/Brittle Fracture Models, IIW4, July 3-8, Seoul, Korea (2011)
2. Dongil Kwon\*, **Junyeong Kim**, Won-Seok Song, Young-Cheon Kim, Seung-Kyun Kang: Multiscale Mapping of Mechanical Characteristics Using Instrumented Indentation Testing, THERMEC 2011, August 1-5, Quebec City, Canada (2011)
3. Young-Cheon Kim, Won-Seok Song, **Junyeong Kim\***, Ji-Won Chung, Dongil Kwon: Nondestructive Evaluation of Mechanical Properties for

Reliability Assessment pf Weldments Using Instrumented Indentation,  
IWJC-Korea 2012, May 8-11, Jeju Island, Korea (2012)

4. Jongheon Kim\*, **Junyeong Kim**, Jinwoo Lee, Dongil Kwon: Evaluation of Thin-film Interfacial Properties Using Indentation Test, PRICM 8, August 4-9, Hawaii, US (2013)
5. **Junyeong Kim**, Woojoo Kim\*, Seung-Hun Choi, Dongil Kwon: Estimation of Fracture Toughness of Metallic Materials Using Instrumented Indentation Test, ICM12, September 10-14, Karlsruhe, Germany (2015)

### **III. Domestic Conference (\* indicates speaker)**

1. 김준영\*, 최민재, 강승균, 권동일: 계장화 압입시험법을 이용한 엔지니어링 플라스틱의 잔류응력 측정, 2009년도 대한금속·재료학회 춘계 학술대회, 4월 23일-24일, 창원컨벤션센터(CECO) (2009)
2. 김준영, 김영천\*, 송원석, 권동일: 역학물성 기반의 신뢰성 평가를 위한 계장화 압입시험법의 응용, 2010년 한국신뢰성학회 춘계 학술대회, 6월 18일, 아주대학교 윤곡관, 법학관, 팔달관 (2010)
3. 김준영, 이경우, 전승원, 권동일: 연속압입시험을 이용한 금속소재의 파괴인성 예측, 2011년도 대한금속·재료학회 추계 학술대회, 10월 27일-28일, 대전컨벤션센터(DCC) (2011)

4. 전승원\*, 김준영, 이진우, 권동일: 구조용강의 파괴인성 천이거동 해석을 위한 연속압입시험의 응용, 2011년도 대한금속·재료학회 추계 학술대회, 10월 27일-28일, 대전컨벤션센터(DCC) (2011)
5. 김준영, 최민재, 강승균, 박찬평\*, 권동일: 계장화 압입시험법의 표준화 동향: ASME, ISO, 제25회 첨단구조재료 심포지엄, 11월 17일-18일, 한국원자력안전기술원 (2011)
6. 권동일\*, 송원석, 강승균, 김준영: 연속압입시험의 표준화 동향 및 법공학적 활용, 2012년도 대한금속·재료학회 춘계 학술대회, 4월 26일-27일, 현대성우리조트 (2012)
7. 전승원\*, 김준영, 권동일: 피로특성 예측을 위한 연속압입시험법의 활용, 2012년도 대한금속·재료학회 춘계 학술대회, 4월 26일-27일, 현대성우리조트 (2012)
8. 이진우\*, 김준영, 조원제, 전승원, 권동일: 연속압입시험법을 이용한 금속재료의 샤프피 충격에너지 예측, 2012년도 대한금속·재료학회 춘계 학술대회, 4월 26일-27일, 현대성우리조트 (2012)
9. 김지연\*, 강승균, 김준영, 권동일: 나노압입시험에서의 소성쌓임이 반영된 접촉면적 예측을 통한 재료물성평가, 2012년도 대한금속·재료학회 추계 학술대회, 10월 25일-26일, 창원컨벤션센터 (2012)
10. 전승원\*, 김준영, 권동일: 연속압입시험법을 이용한 AI합금의 피

로특성 예측, 제26회 첨단구조재료 심포지엄, 11월 15일-16일, 부산센텀호텔 (2012)

11. 전승원\*, 김준영, 김지연, 권동일: 계장화 압입시험법을 이용한 API강재의 피로특성 예측, 2013년도 대한금속·재료학회 춘계 학술대회, 4월 25일-26일, 제주국제컨벤션센터 (2013)
12. 김준영\*, 전승원, 이경우, 권동일; 연속압입시험을 이용한 금속소재의 파괴인성 평가, 2014년도 대한기계학회 재료 및 파괴부문 춘계학술대회, 4월 3일-4일, 서귀포 KAL호텔 (2014)
13. 전승원\*, 김준영, 권오민, 권동일: 연속압입시험법을 이용한 API 강재의 피로특성 예측, 2014 Materials Fair, 9월 25일, 서울대학교 (2014)
14. 안희준\*, 김종형, 김준영, 전승원, 이경우, 권동일; 계장화 압입시험을 활용한 금속소재 물성 평가 연구, 2015년도 대한기계학회 춘계학술대회 재료 및 파괴 부문, 4월 2일-3일, 서귀포 KAL호텔 (2015)